Durham University

Durham E-Theses

An aeroacoustic study of industrial gas turbine intake and exhaust systems.

Blake, Simon

How to cite:

Blake, Simon (2008) *An aeroacoustic study of industrial gas turbine intake and exhaust systems.*, Durham theses, Durham University. Available at Durham E-Theses Online: http://etheses.dur.ac.uk/2404/

Use policy

The full-text may be used and/or reproduced, and given to third parties in any format or medium, without prior permission or charge, for personal research or study, educational, or not-for-profit purposes provided that:

- a full bibliographic reference is made to the original source
- a link is made to the metadata record in Durham E-Theses
- the full-text is not changed in any way

The full-text must not be sold in any format or medium without the formal permission of the copyright holders.

Please consult the full Durham E-Theses policy for further details.

Academic Support Office, The Palatine Centre, Durham University, Stockton Road, Durham, DH1 3LE
e-mail: e-theses.admin@durham.ac.uk Tel: +44 0191 334 6107
http://etheses.dur.ac.uk

AN AEROACOUSTIC STUDY OF INDUSTRIAL GAS TURBINE INTAKE AND EXHAUST SYSTEMS.

Simon Blake BEng

Submitted for the degree of
Master of Science

School of Engineering
University of Durham

2008

The copyright of this thesis rests with the author or the university to which it was submitted. No quotation from it, or information derived from it may be published without the prior written consent of the author or university, and any information derived from it should be acknowledged.

1 8 MAR 2009

Table Of Contents

Nomenclature

x	Axial distance along x axis	(metres)
y	Axial distance along y axis	(metres)
Δx	Axial grid size in x direction	(metres)
Δy	Axial grid size in y direction	(metres)
L	Length	(metres)
A	Cell face area	(metre^2)
V	Cell volume	(metre^3)
m	Unit measurement	(metre)
t	Time	(seconds)
$Tstep$	Timestep	(seconds)
i	Grid index in x direction	
j	Grid index in y direction	
$imax$	Maximum number of cells along x axis in a domain	
$jmax$	Maximum number of cells along y axis in a domain	
K	Unit of temperature measurement	(Kelvin)
Pa	Unit of pressure measurement	(Pascal)
Kg	Unit of mass measurement	(Kilogramme)
Q	Heat flux	(Watts/metre^2)
k	Thermal conductivity	(Watts/m.K)
$\dot{m}$	Mass flow rate	(Kg/second)
u	Flow velocity in x direction	(metre/second)
v	Flow velocity in y direction	(metre/second)
VEL	Velocity magnitude	(metre/second)
p	Pressure	(Pascal)
ρ	Density	(Kg/metre^3)
C	Wave speed	(metre/second)
M	Mach number	
$P0$	Stagnation pressure	(Pascal)
$PExit$	Static pressure at domain outlet	(Pascal)
T	Temperature	(Kelvin)
$T0$	Stagnation temperature	(Kelvin)
E	Total energy	
R	Universal gas constant (taken to be 287 KJ/Kg.K for air)	
γ	Ratio of specific heats (taken to be 1.4 for air)	
Cp	Specific heat capacity at constant pressure	(Joules/Kg.K)
Cv	Specific heat capacity at constant volume	(Joules/Kg.K)
e	Specific energy = RT/γ-1	
a	Thermal diffusivity $\alpha = k/(\rho.Cp)$	
a	Also taken to be wedge half angle in the oblique shock relations.	

ρu	*X* momentum
ρv	*Y* momentum
H	Total enthalpy
RO	Conservative variable ρ
ROU	Conservative variable ρu
ROV	Conservative variable ρv
ROE	Conservative variable ρE
CMASS	Mass flux in the axial x direction
CMASSX	*X* component of mass flux CMASS
CMASSY	*Y* component of mass flux CMASS
XFLUX	Momentum flux in x direction
XFLUXX	X component of x momentum flux
XFLUXY	Y component of x momentum flux
YFLUX	Momentum flux in y direction
YFLUXX	X component of y momentum flux
YFLUXY	Y component of y momentum flux
EFLUX	Energy flux in x direction
EFLUXX	X component of energy flux
EFLUXY	Y component of energy flux
P_SIDE	Axial pressure force
θ	Oblique shock angle
δC_1 , δC_2 , δC_4 , δC_5	Characteristic variables used in the NRBC's
sin	Trigometric function sin
cos	Trigometric function cosine
tan	Trigometric function tangent
cot	Trigometric function cotangent
f	Frequency Hz
ω	Angular frequency (radian per second)
β	Angle of outlet boundary relative to datum (degrees)
λ	Wavelength (metres)
ε	Non dimensional error value
FTBS	Forward Time Backward Space
FTCS	Forward Time Centred Space
CFL	Courant Friedrichs Lewy criterion (Courant number)
HOT	Higher Order Terms
NRBC	Non reflecting boundary condition
FFT	Fast Fourier transform
RK	Runge Kutta coefficient
SF	Dimensionless artificial viscosity smoothing coefficient

Acknowledgements

I would like to thank Professor Li He, Chair of Thermofluids at the University of Durham for his invaluable help and guidance during my studies and without whose support and insight this work would not have been possible.

Simon Blake

Summary

The purpose of this study was to seek a means of numerically simulating and analyzing the aerodynamic and acoustic behaviour of industrial gas turbine intake or exhaust systems. The method was developed in an effort to advance the current state of the art employed for the prediction of intake and exhaust noise. Current methods rely upon the summation of experimentally gathered insertion loss data for individual system components. This approach requires that physical testing of chosen components be undertaken which can be both costly and time consuming.

The proposed numerical method is based upon a two stage finite volume solution of the two dimensional non linear Euler equations whereby an aerodynamic solution for the mean flow is first obtained followed by a solution for the acoustic field. The method has been found to be both accurate and easy to implement, furthermore being numerically based it eliminates the need for the costly and time consuming procurement and testing of physical prototypes. In this respect it is considered to advance the present state of the art.

The two step Euler solver developed herein employs a multiblock finite volume formulation wherein the hyperbolic Euler equations are solved using a cell centred finite volume technique employing a second order central differencing method for spatial discretisation on a multiblock grid and with temporal integration being undertaken using an explicit time marching two stage second order Runge Kutta scheme. In the first step the mean flow is solved using the finite volume method to obtain a transient or pseudo steady state solution. This provides both the general aerodynamic characteristics of the system and a baseline steady state solution for the acoustic analysis. In the second step a perturbation representing an acoustic disturbance is introduced to the mean flow and the non linear Euler equations are again solved using the finite volume scheme. Spurious non physical numerical reflections at the domain boundaries are prevented by the application of the characteristic based non reflecting boundary conditions. The resulting unsteady pressure field is then postprocessed to generate the unsteady pressure disturbance due to the applied acoustic perturbation. The interaction of the acoustic disturbance can then be evaluated by examination of the pressure amplitudes and frequency spectra at any location within the domain.

The scheme was applied to the study of the aerodynamic and acoustic characteristics of an industrial gas turbine emergency shutdown compressor bleed system. It was found to accurately predict the acoustic attenuation characteristics of the system, furthermore it was shown that it could also be usefully applied as a design tool and as an example of this a change of attenuation performance of the bleed system is demonstrated by a simple relocation of the baffle silencer within the system ducting. It is concluded that the method developed herein demonstrates that a numerical solution to predict the acoustic attenuation characteristics of an industrial gas turbine silencing system is possible and as such offers an improved means for undertaking the acoustic design of products for noise control in industrial gas turbine applications. In this respect it is considered to advance the present state of the art.

Thesis Overview

This aim of this thesis was twofold. Firstly the author sought to gain an in depth understanding of the principal and implementation issues of computational fluid dynamics by developing a CFD code. Secondly the author sought to investigate the feasibility of improving the current method adopted for the acoustic design of industrial gas turbine intake and exhaust systems. In this regard it is composed of the following.

Chapter 1 serves as an introduction to the study. The motivation and need for the study are addressed and the technical and engineering challenges are discussed.

Chapter 2 presents a literature review where the numerical methods adopted for the solution of the mean flow and acoustic field are addressed. In this respect it provides an overview of the aeroacoustic design of industrial gas turbine intake systems and also of numerical methods such as the Jameson scheme [12] employed in this study.

Chapter 3 addresses the basic formulation of the numerical methods employed in this study. Solutions for the one dimensional heat conduction equation and the one dimensional wave equation are presented to demonstrate the advantages and disadvantages of the various numerical schemes and from these the choice of scheme adopted in this study becomes self evident. The formulation of the two stage finite volume method for the acoustic solution is also discussed and prescription of the non reflecting boundary conditions presented.

Chapter 4 presents a number of basic validation cases for one dimensional and two dimensional flows. These serve to prove the accuracy and convergence capabilities of the chosen numerical scheme as well as verify its accurate representation in the author's computer codes. Having proven the scheme's stability, accuracy and convergence capabilities and having determined the magnitude of artificial viscosity required for algorithm stability the numerical method was deemed acceptable for use in the forthcoming acoustic studies.

Chapter 5 presents a number of case studies wherein the aerodynamic and acoustic characteristics of a combustion intake system and an emergency compressor shutdown bleed silencing system were examined. Case studies 1 and 2 examine the aerodynamic characteristics for each system and from these it becomes possible to identify undesirable flow characteristics that could adversely affect system performance. Case study 3 presents an acoustic study of the compressor bleed system and case study 4 presents a brief design study for the compressor bleed system wherein a change of system attenuation is found by a simple relocation of the baffle silencer.

In Chapter 6 conclusions are drawn and recommendations made for future work. Recommendations for possible improvements relating to the computational efficiency of the numerical solution include the use of multigrid, adapted or unstructured grids, the use of higher order methods and the adoption of 64 bit processor architecture and parallel processing.

1.0 Introduction

1.1.1 Overview

The use of computational fluid dynamics (CFD) for the prediction of aerodynamic behaviour has gained acceptance in a wide range of engineering applications ranging from automotive and aerospace to power generation. This is largely due to two factors, namely the development of robust and accurate numerical methods and the emergence of modern high speed computing facilities which permit the simulation of complex flows on a typical modern desktop pc. These factors, together with the development of intuitive graphical user interfaces have led to the availability of commercial CFD codes such as Fluent, Star CD and Ansys CFX and hence their application on an everyday basis for the computation of aerodynamic flows in a wide range of industrial applications.

In the past decade there has emerged much interest in the use of CFD methods for the computation of acoustic behaviour, resulting in the emergence of computational aeroacoustics (CAA) as a specialist field of study. However in comparison to CFD methods, CAA is relatively new and as a result many new opportunities for the application of CAA remain. This is particularly so in the industrial power generation industry where the growing use of gas turbines for power generation, coinciding with the emergence of strict environmental and health & safety legislation has led to a need to minimize the acoustic impact of gas turbines upon the environment. This presents a formidable engineering challenge.

Whilst the application of CAA methods to gas turbines is not new, much of the work undertaken to date has been in the aero engine industry where the focus has been upon the reduction of noise associated with compressor blading, the turbine core and jet noise arising from the discharge of the exhaust to atmosphere. To this authors knowledge few, if any efforts have been made to apply either CAA or CFD methods to the study of gas turbine acoustic emissions in an industrial power generation application.

1.1.2 Engineering relevance, state of the art and motivation for the work.

Recent and rapid industrialization of countries in the Far East and Asia have led to increased demand for energy commodities such as oil and coal resulting in significant rises in energy costs globally. However existing power generating capacity has proved insufficient to satisfy increasing energy consumption and this, together with the extended timescales required for new build power stations to be built and brought online has led to a global shortage of power generating capability in the immediate and foreseeable future. Gas turbine driven generating plant however can be very quickly constructed and brought online, in addition their ability to cope with short term peak demand have made gas turbine fired power stations extremely attractive. In addition, natural gas is viewed favourably by the environmental lobby as being comparatively clean burning and hence less polluting than coal or oil fired power plant. These factors, together with the ease at which natural gas may be transported in large quantities by pipeline or by LNG tanker have

made gas turbine fired power plant an attractive means of generating power globally.

However, as the use of industrial gas turbines for power generation is becoming more popular, some disadvantages to their use are being noted. Due to their compact size and low cost many new build gas turbine fired power stations are now being situated in urban or residential areas where it is vital to minimize their environmental impact, particularly with regard to noise. As a result a number of companies now design and manufacture acoustic and emissions control equipment specifically for the industrial gas turbine market. One of the most successful and longest established of these is American Air Filters Limited.

It was during the author's time as a senior research engineer at AAF Ltd that it became apparent to him that many of the methods used for estimating the acoustic attenuation characteristics of intake and exhaust systems were largely empirically based, relying either upon proprietary test data or on data published in sources such as Beranek [4]. Whilst useful, the successful application of such data relies entirely upon the experience of the acoustic engineer and the ability to correctly select individual components based upon their individual insertion loss characteristics and compile them into a compatible system. Since a typical gas turbine intake system can be geometrically complex this can pose a considerable challenge and makes a computational solution attractive, should it prove possible.

In addition the flow characteristics of intake systems themselves are complex. An intake system is typically required to fulfill a number of roles, these primarily being the provision of the required mass flow of clean, filtered combustion air, attenuation of the acoustic emissions emanating from the gas turbine bellmouth (primarily compressor blade pass frequencies) and minimisation of differential pressure losses (since differential pressure losses constitute a significant loss of power generating capacity). In addition very strict specifications for the static pressure profiles at the bellmouth are often imposed by the gas turbine manufacturers as it is known that asymmetric static pressure profiles at the inlet to the gas turbine can induce loss of performance and in extreme cases compressor blade vibration induced fatigue failure as a result of unequal aerodynamic loading. To complicate matters further the geometry of the intake systems themselves are often dictated by the demands of the available space envelope and low capital cost and as a result many installations feature undesirable geometric features such as sudden contractions or enlargements, truncated diffusers and 90 degree elbow bends which can be the cause of high pressure drop, flow separation and vortex shedding. Indeed it is the author's experience that vortex induced vibration as a result of poor intake geometry has been responsible for a number of fatigue failures of intake system components and consequential turbine damage.

In addition the imposition of more stringent environmental legislation governing noise levels permitted from industrial gas turbines dictate that external noise emissions from the gas turbine must be attenuated by the provision of an acoustically insulated enclosure and silencing system. In the past the high levels (upto 130 dBA) of tonal and broadband noise arising from the many mechanical and aerodynamic

sources within the gas turbine have been successfully attenuated by the use of passive intake silencers and the adoption of heavy gauge steel plate (often 6 mm thickness) and fibrous insulating material (typically rockwool) in the construction of the gas turbine enclosure and intake system. However the adoption of heavy gauge materials and acoustic cladding are both costly and increase system weight and can prove to be commercially undesirable, especially in offshore applications where minimisation of system weight is a priority. Clearly therefore any means that may permit a reduction in noise emissions without significantly increasing build cost or weight would be particularly attractive and merit investigation.

Whilst many efforts have and continue to be made within the global CFD community to understand internal noise emissions within the gas turbine itself, few efforts if any are being made to develop improved methods for managing external noise emissions from the gas turbine. As a result industry is still largely reliant upon the continued use of empirically based methods some of which date from the 1940's. To the authors knowledge Euler based methods have not yet been applied specifically to the study of external noise emissions from industrial gas turbines. However it is also this authors belief that the increasing use of gas turbines for industrial power generation together with the apparent trend to locate these within urban or residential areas and the emergence of stricter environmental controls will inevitably result in an urgent need to more effectively manage external noise emissions from the gas turbine by better acoustic design of the intake system. It was the author's intention therefore to investigate the feasibility of advancing the present state of the art (i.e. empirically based methods) by developing a numerically based method whereby the acoustic performance of an intake system as a whole could be evaluated with an emphasis on developing a relatively simple tool that could be easily applied to the solution of practical engineering problems.

There have been relatively few advancements made in the field of industrial gas turbine noise control beyond the use of proprietary test data or public domain empirically based sources such as Beranek. Proprietary test data typically takes the form of insertion loss measurements acquired in an acoustic test rig which typically comprises of a series of ducts containing a white noise generator in lieu of a working gas turbine as a broadband noise source at the required power level and a number of working sections into which various components of interest such as silencers may be placed. Measurements of the acoustic sound power are made upstream and downstream of the item under test and from these an estimate of the insertion loss for the component may be made. If insertion loss values are known for the components comprising an intake system then an estimate of the acoustic attenuation characteristics of the intake system as a whole may be constructed.

The advantages of such a method are its simplicity and low cost., and given a skilled and experienced designer an accurate assessment of the acoustic attenuation capabilities of a candidate intake system design may be quickly made. However the method does suffer from a number of disadvantages. A number of these are described below.

Firstly, it's success relies upon the availability of insertion loss data for the candidate system components, if these are not available then they must obtained by testing of a physical prototype with consequent associated procurement and development costs and time delay.

Secondly, since no flow effects are taken into account the generation of noise as a result of aerodynamic effects is entirely ignored. Whilst the maximum flow velocities in most industrial gas turbine intake systems manufactured to date has never exceeded 40 metres/second and it has therefore been successfully argued that as a result flow noise is generally not a concern, the trend toward smaller, lower cost systems and hence higher flow velocities mean that this argument may not be sustainable.

Thirdly, the correct summation of insertion loss data to create an intake system design having the desired acoustic characteristics is still heavily reliant upon the skill and experience of the designer. From the authors experience suitably experienced and knowledgeable acoustic engineers are a rarity.

Finally, the use of a method based solely upon summation of static insertion loss measurements for individual system components in the authors opinion completely ignores the effect of system configuration upon the overall acoustic system response. This could potentially result in the non prediction of significant and unanticipated noise sources such as those arising from shear layers formed as a result of flow separation, vortex shedding from blunt bodies immersed in the flow such as anti ice pipe work or from jet noise arising from high spatial velocity within the silencer flow passages.

It was therefore considered by this author that whilst the current method based upon summation of insertion loss measurements has served the industry well for a number of decades, given the advances in computational capabilities and numerical methods that may be applied to acoustic problems there now exists some scope for advancing the present state of the art. The object of this thesis therefore was defined as to ascertain the feasibility of developing a simple yet useful method for the study of acoustic characteristics of industrial gas turbine intake systems with an emphasis on developing a tool that could easily be used to investigate the effect of system configuration upon acoustic performance.

1.1.3 Technical Challenges

Aeroacoustic problems can be considered to fall into two categories - the computation of the sound generated as a result of aerodynamic effects such as turbulence or fluid-structure interaction and the study of the propagation of a known source into the surrounding medium which may be the atmosphere. The former utilise methods such as Direct Numerical Simulation (DNS) and Reynolds Averaged Navier Stokes (RANS) methods to directly compute sound as a fluctuating pressure variable. The latter employ techniques such as the use of boundary element methods, Lighthill's acoustic analogy {1,2] , Ffowcs-Williams [3] or linearised Euler methods.

Whilst direct solution of the aerodynamic flow field would be desirable, the requisite solution of the full compressible Navier Stokes equations would be computationally expensive within the large bounded domains typically found in an industrial gas turbine intake or exhaust system. Fortunately however, in the application considered here direct numerical solution of the aerodynamic flow field is not required at the acoustic scale since both the amplitude and frequency content of the source at the inlet boundary are known from the noise spectrum recorded at the gas turbine inlet. Therefore the less computationally demanding methods such as boundary element methods, Lighthills method, Ffocws Williams or linearised Euler methods may be effectively employed to compute the acoustic characteristics of the system under study.

However, it was considered by the author that a solution of the mean flow was also of particular interest, for it would yield useful information regarding the general aerodynamic characteristics of the system in addition to its acoustic characteristics. For this reason a two stage CFD approach was proposed wherein in the first step the 2D non linear Euler equations were solved using a finite volume time marching method to obtain a transient or pseudo steady state solution thereby providing information regarding the general aerodynamic characteristics of the system under study such as differential pressure drop estimates, static pressure and velocity profiles and identification of unsteady flow phenomena. Having obtained a pseudo steady state solution the acoustic field could be solved for by introducing a sinusoidal pressure perturbation representing a selected amplitude and frequency content of the gas turbine power spectrum into the mean flow at the inlet boundary and preventing non physical numerical reflections at the inlet and outlet boundaries by applying characteristic based non reflecting boundary conditions. The unsteady pressure field due to the applied acoustic perturbation could then be solved for in the time domain by subtraction of the known pseudo steady state solution from the transient solution arising from the introduction of the perturbation to give the unsteady pressure field due to the applied acoustic perturbation. In this way it would be possible to observe the interaction and propagation of the original acoustic source within the domain.

Having chosen a method for the numerical solution of both the aerodynamic and acoustic fields, other difficulties specific to the numerical solution arise. Among those that pose the greatest difficulties are the scale effect, the choice of numerical solution method, the need to carefully control the numerical damping in order to prevent attenuation of the pressure as the fluctuating variable in the acoustic solution, creation of the computational grid and computational requirements. Each of these are discussed below.

Scale effects.

From a practical perspective the scale effect presents the greatest challenge. These relate to both the relative magnitudes of the acoustic pressures and the mean flow and the small acoustic wavelength relative to the computational domain. In the first instance since the acoustic pressures are much smaller than the mean value they are extremely sensitive to numerical errors such as dissipation and dispersion or the

magnitude of artificial viscosity damping that may be applied to stabilise the numerical scheme. In the second instance since most of the acoustic energy emitted by the gas turbine that is perceived to be objectionable by the human ear lies within the 3 KHz to 8 KHz frequency bandwidth the acoustic wavelength is correspondingly small, typically in the range of 0.1 to 0.04 metres. In addition the acoustic wavespeed may be very high relative to the mean flow, perhaps an order of magnitude greater. Furthermore it can be shown that in order to minimize numerical damping of the acoustic field a grid resolution of some 30 to 50 computational cells per wavelength is typically required. Together these factors conspire to necessitate a very small grid size with an edge length of less than 1.0 millimeter not being uncommon. Given that a typical gas turbine intake system may feature internal dimensions exceeding some 2.5 metres width by 9 metres in length it become immediately apparent that as a result of these scaling effects the computational domain may easily consist of many millions of cells meaning that solution becomes computationally prohibitive. The high cell count can be considerably reduced by the use of higher order schemes (e.g. Wells & Renault [22]) report adequate resolution of the acoustic field using a grid resolution of only 6 to 8 cells per wavelength by the use of 6^{th} order central differencing) although these have not been investigated in this study. For the case of an exhaust system the scaling effect becomes even more pronounced than that for the case of an intake system. This is due to the higher static temperature within the exhaust system resulting in an increase of the local speed of sound and hence shorter wavelength of the acoustic disturbance necessitating both a more highly refined grid and a smaller value of the timestep to maintain solution accuracy and stability. For this reason a fully three dimensional solution was not considered practical, the author instead opting for a less computationally demanding two dimensional solution. This was still considered valid however as in the author's experience many of the intake and exhaust silencing systems designed for the industrial gas turbine market tend to exhibit symmetry about one, and often two planes making a simple two dimensional planar solution still worthy of study and capable of yielding useful information to the designer.

Choice of numerical solution method.

The Jameson scheme [12] was chosen for its simplicity and ease of application to the solution of unsteady flow behaviour using a time marching method. Being a density based method however the use of this scheme did present some difficulties with regard to achieving a fully converged solution for low speed flows. This was particularly so for those intake systems featuring large filter plenums where the flow local Mach Number could become less than 0.10. As a result it was found that the method could be most successfully applied to systems where significant changes in density arising from higher flow velocities could be expected, such as in the compressor emergency bleed system considered in this study.

Control of numerical damping.

Numerical damping can arise from numerous sources such as natural damping inherent in the numerical scheme itself, numerical round off errors, the use of an excessively coarse grid or the application of excessive amounts of artificial viscosity

(see the above discussion relating to scale effects). Whilst the use of artificial viscosity is useful to control numerical oscillations and ultimately divergence of the second order scheme when applied to the solution of the mean flow, an undesirable effect is that it would tend to dampen the pressure fluctuations that we seek in the acoustic solution.

Fortunately however by adopting the two stage CFD based approach considered here it is possible to solve firstly for the mean flow using a modest value of the artificial viscosity of say two percent and once having achieved a pseudo steady state converged solution the acoustic field could then be solved for using a much lower value of artificial viscosity, say 0.1 percent. In this way attenuation of the fluctuating pressure variable in the acoustic solution could be minimized.

Computational grid generation

The geometry of industrial gas turbine intake and exhaust systems are quite complex featuring multiple interconnected ducts, variable area transitions and diffusers, elbow bends and bodies immersed in the flow such as passive baffle type silencers, anti ice systems and air treatment devices such as intake filtration. Representation of such complex geometry calls for a multiblock approach. In the multiblock method the computational domain is decomposed into a number of smaller sub domains which are then linked to one another in the solver using interface blocks. In the study of the compressor emergency bleed system studies in this work the computational domain consisted of twenty three discrete quadrilateral sub domains each of which were created using transfinite interpolation, in this way a mapped grid could be constructed for each sub domain. Information exchange at the sub domain boundaries was accomplished in the solver by means of explicitly defined interface block subroutines.

The advantage of the multiblock approach was that complex domains could be easily represented, in addition the mapped quadrilateral grid was found to be of high quality thereby promoting rapid solution convergence. However the overall grid creation process was found to be time consuming due to the need to segregate the domain into grid blocks, manually create the computational grid for each block and then explicitly define the interface block subroutines in the solver. It is considered by the author that grid creation remains one area where the current code could be improved, perhaps by the use of Cartesian cut cell methods or unstructured grids.

Computational requirements.

To conduct the numerical studies a number of Fortran programs were written by the author. For the acoustic studies of the bleed system three codes were written, a grid program to produce the multiblock computational grids, a steady state solver to compute the mean flow, and an acoustic solver featuring non reflecting boundary conditions to compute the acoustic flow. At the time of the study the Intel Fortran compiler used was available only as 32 bit architecture which restricted the available machine RAM to 2GB. Therefore the computational domain had to be devised so as to permit solution within the 2GB limit, and due to the large physical size of the

bleed system under consideration this limited the upper frequency limit for the acoustic study to approximately 800 Hz.

The numerical studies were undertaken on a 3 GHz Pentium IV pc with 2GB of physical RAM. Even so, solution times were extensive, for the case of the 800 Hz acoustic studies conducted on the bleed system the total solution time was approximately 240 hours. Whilst such prolonged solution times may be acceptable for research purposes, it is considered that such extended solution times would not be acceptable within industry. It is suggested that for future studies the solver codes could be recompiled using the new 64 bit release of the Intel Fortran compiler. This would permit the utilisation of further machine RAM and offer increased processor bandwidth, thereby reducing solution times. It is also suggested that perhaps a parallel version of the code could be developed as this would permit solution of the domain on multiple processors.

2.0 Literature Review.

Aeroacoustic or flow noise is generated as a result of small scale fluctuations that may arise within a viscous flow from mechanisms such as shear flow, fluid-structure interaction or vorticity. Solution of an aeroacoustic problem can be segregated into two distinct areas of study - the application of CFD methods to solve for the near field acoustic disturbances arising from aerodynamic flow and the subsequent solution of the propagation of these disturbances into the far field using methods such as Lighthills analogy [1,2] and the Ffocws Williams Hawkings method [3].

Solution of the pressure field arising from the mean flow is generally solved for using a time domain solution of the Navier Stokes equations in the near field using either Reynolds Averaged Navier Stokes (RANS) methods or Large Eddy Simulation (LES). However a solution of the complete Navier Stokes equations is computationally expensive and therefore prohibitive for the practical computation of acoustic behaviour within a large bounded domain such as those presented by the gas turbine intake and exhaust systems considered in this study. Furthermore since noise propagation is not strongly affected by viscosity the propagation of acoustic disturbances in the near and mid field can be described using a form of the Navier Stokes equations wherein viscosity is neglected, i.e. the Euler equations. Furthermore, since the pressure fluctuations arising from acoustic disturbances are typically two or three orders of magnitude less than those of the mean flow a linearised form of the Euler equations may be employed for the simulation of acoustic propagation. This has resulted in the formulation of the linearised Euler method (LEE) which has found many applications in industry.

2.1 Design methods in noise control

Design methods employed for noise control of industrial gas turbines tend to be largely based upon proprietary test data and the works of Beranek [4]. This is largely due to the scale effect and the difficulties associated with the computation of unsteady aerodynamic flow and acoustic propagation within the large bounded domains typical of industrial gas turbine intake and exhaust systems. Nevertheless some efforts have been made to undertake numerical studies of gas turbine intake systems although these have largely focused upon the study of passive baffle type silencer often employed for the control of tonal noise emanating from the gas turbine compressor blading. Tam and Fahy [5] present numerical results and analytical solutions for the noise intensity within a vertical splitter type silencer. Soderman [6] presents a method for predicting silencer attenuation based upon insertion loss measurements and Ver [7] considers the conceptual design of silencers considering factors such as silencer type, lining material and self noise whilst Munjal [8] considers the design of cylindrical pod silencers.

Whilst these works are illuminating, it is apparent that, to this author's knowledge at least, no efforts have yet been made to apply CFD methods to the study of the aerodynamic and acoustic behaviour of a complete industrial gas turbine intake system. It is proposed therefore in this study to advance the current state of the art by devising a method that can be used for the simulation of both the unsteady mean

flow and the acoustic propagation, thereby providing a useful design tool that may be effectively used on a day to day basis for the practical computation of intake system flow and acoustic behaviour.

The methodology adopted in this study is essentially a two step method, wherein the first step the mean flow is solved for by CFD methods using a time marching finite volume scheme for the non linear Euler equations followed by a second step wherein the propagation of a simulated acoustic disturbance to the mean flow is again solved for using a finite volume time marching solution of the Euler equations (note that noise generation itself is not solved for using the Euler scheme). These are discussed further below.

2.2 Solution of the mean flow.

Many numerical schemes exist for the solution of the Euler equations. These are typically classified by the form of the time stepping scheme used and may be either of implicit formulation (such as the Crank Nicholson method) or explicit formulation (such as the MacCormack and Lax Wendroff methods). A description of these and other methods are given by Anderson [9], Laney [10] and by Tannehill, Anderson & Pletcher [11]. However, since noise is inherently a time dependent phenomena a time dependent solution of the governing equations is required, dictating therefore that an explicit or time marching method be used. Whilst a number of explicit or time marching schemes exist that may be successfully applied to the solution of the unsteady Euler equations such as the MacCormack predictor-corrector method or the variations of the Lax-Wendroff Scheme, the method adopted in this study is the well known finite volume formulation developed by Jameson, Schmidt and Turkel [12]. This is a multistage Runge Kutta scheme similar to the well known Lax Wendroff method but having the added advantage in that the user has control over the damping applied to the scheme. It is second order accurate in space and time integration may be undertaken by either second or fourth order Runge Kutta . For the work undertaken in this study the Jameson scheme was chosen for its finite volume formulation, its simplicity and the ease at which the numerical scheme may be implemented in a computer code.

2.3 Solution of the acoustic pressure field.

It is common practice to use RANS or LES methods to compute the nearfield sound followed by other methods such as Lighthills analogy, Ffowcs Williams Hawkings, boundary element methods or Kirchoff integrals to compute the propagation of the near field sound to the far field. However methods such as Lighthills analogy or Ffocws Williams assume that the sound propagates in a medium where velocity gradients are not significant which may not be the case in a typical gas turbine intake or exhaust system where significant velocity gradients can exist at the duct walls or elsewhere throughout the domain. Furthermore acoustic propagation can be considered to be almost unaffected by viscosity and the acoustic amplitudes are often negligible when compared to the mean flow. In addition the acoustic power spectrum at the gas turbine bellmouth is usually known from manufacturer data hence a direct computation of the noise source is not required. Therefore, with the

pressure perturbation due to the acoustic disturbance at the inlet boundary to the domain known, and considering that viscosity effects can be neglected then both the aerodynamic and acoustic fields can be solved for via a solution of the Euler equations in the time domain. In this study the Jameson finite volume scheme with user controlled artificial viscosity is therefore adopted for the solution of both the mean flow and the acoustic field.

However, one of the most significant obstacles to obtaining an acoustic solution using the time domain CFD method is the relative magnitude of the acoustic wave amplitudes to the mean flow. Due to the small acoustic wave amplitudes some provision must be made to allow acoustic waves to exit the domain without undergoing numerical reflection at the inlet and outlet boundaries as failure to do so would result in spurious non physical waves reflecting from the downstream boundary into the interior, contaminating the solution and causing divergence. Therefore some form of non reflecting boundary condition must be devised. Fortunately a considerable amount of literature regarding the formulation of non reflecting boundary conditions for the Euler equations exists with the methods proving most popular being the Local One Dimensional Inviscid (LODI) formulations of Giles [13] and Thompson [14,15] (and developed further by Poinsot and Lele [16]) and the Perfectly Matched Layer (PML) introduced by Berenger [17] and implemented in a form for the Euler equations by Hu [18,19].

The local one dimensional inviscid methods popularized by Giles and Thompson essentially set the velocity of the incoming characteristic at the boundary to zero, thereby in effect canceling any spurious reflections at the boundary. They are robust and easy to implement but being one dimensional are by design limited to the study of plane waves where the angle of the outgoing wave to the outlet boundary can be considered to be small. However in many duct acoustic problems the boundaries are often dictated by the configuration of the duct and in such cases the one dimensional assumption may not be valid. In such instances the perfectly matched layer method may be adopted instead. This involves the extension of the computational grid to include the construction of an additional buffer zone wherein the outgoing wave amplitudes are damped to some constant value. Three methods of implementing the PML technique are presented by Richards et al [20] and these are reported to offer favourable non reflecting properties in turbomachinery problems. The use of PML methods however do incur additional computational expense and with the exception of the work by Richards et al, it appears that little work has been undertaken to prove their validity in practical applications. Given the ease with which the LODI formulation of the non reflecting boundary conditions may be formulated and applied, these have been adopted in this study for prescription of the inlet and outlet boundary conditions when undertaking the solution of the acoustic field.

3.0 Numerical Methods

Introduction

The formulation of the finite volume scheme employed in this study require that the fundamental aspects of creating a numerical scheme to model a set of partial differential equations (pde's) be addressed. Whilst the object of the overall study was to develop a scheme for the two dimensional Euler equations, it was considered useful to first develop a scheme for a more simple family of pde's to allow fundamental aspects such as differencing methods, stability and convergence issues and the formulation of the finite volume method to be investigated.

3.1 Finite Difference Methods

It was elected to initially study the one dimensional heat conduction problem as the governing PDE was both simple and easily applied to a numerical solution and an exact analytical solution was known that could be used for validation of the simulation results .

The governing equation for 1D unsteady heat conduction is given as $\frac{\partial T}{\partial t} = \alpha . \frac{\partial^2 T}{\partial x^2}$

To compute a numerical solution it was necessary to replace the differential derivative terms $\partial T/\partial t$ and $\partial^2 T/\partial x^2$ with differencing formulae. A computational stencil was derived where the evolution of temperature with time was considered to occur on a grid where the x axis represented the spatial distance along the 1D domain and the y axis represented time. The cell temperature T_i varied with distance x and time t as shown in Figure 3.1.1.

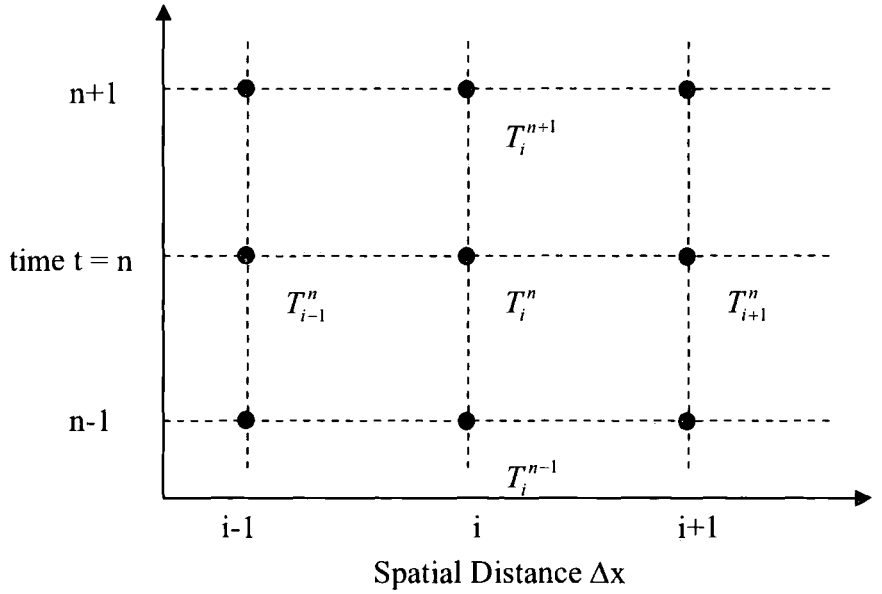

Figure 3.1.1 Representation of Computational Grid

Notation

Subscript $_i$ referred to a position on the spatial grid within the current timestep.
Superscript ^{n} referred to position within the temporal, or time grid.
Δx represented the grid spatial step size.

There exist a number of differencing schemes which may be applied, these being first order forward difference, first order backward difference, first order central difference and second order central difference. Each of these were considered in turn

First order, forward difference.

Considering a Taylor series expansion about the point x_i at temperature T_i

$$T(x+\Delta x) = T_{x=i} + \Delta x.\left(\frac{\partial T}{\partial x}\right)_{x=i} + \frac{\Delta x^2}{2}.\left(\frac{\partial^2 T}{\partial x^2}\right)_{x=i} + \frac{\Delta x^3}{3!}.\left(\frac{\partial^3 T}{\partial x^3}\right)_{x=1} + ...$$

$$\text{Then } \left(\frac{\partial T}{\partial x}\right)_{x=i} = \frac{T(x+\Delta x) - T_{x=i}}{\Delta x} - \frac{\Delta x}{2}.\left(\frac{\partial^2 T}{\partial x^2}\right)_{x=i} - \frac{\Delta x^2}{3!}.\left(\frac{\partial^3 T}{\partial x^3}\right)_{x=1} + ...$$

$$\text{i.e. } T_{i+1} = T_i + \left(\frac{\partial T}{\partial x}\right)_i .\Delta x + \frac{\Delta x^2}{2}.\left(\frac{\partial^2 T}{\partial x^2}\right)_{x=i} + \frac{\Delta x^3}{3!}.\left(\frac{\partial^3 T}{\partial x^3}\right)_{x=i} + ...$$

First order backward difference.

Again considering a Taylor series expansion about the point x_i at temperature T_i

$$T(x-\Delta x) = T_{x=i} - \Delta x.\left(\frac{\partial T}{\partial x}\right)_{x=i} + \frac{\Delta x^2}{2}.\left(\frac{\partial^2 T}{\partial x^2}\right)_{x=i} - \frac{\Delta x^3}{3!}.\left(\frac{\partial^3 T}{\partial x^3}\right)_{x=1} + ...$$

Then

$$-\left(\frac{\partial T}{\partial x}\right)_{x=i} = \frac{T(x-\Delta x) - T_{x=i}}{\Delta x} + \frac{\Delta x}{2}.\left(\frac{\partial^2 T}{\partial x^2}\right)_{x=i} - \frac{\Delta x^2}{3!}.\left(\frac{\partial^3 T}{\partial x^3}\right)_{x=1} + ...$$

Rearranging we obtain

$$\left(\frac{\partial T}{\partial x}\right)_i = \frac{T_i - T_{i-1}}{\Delta x} + \frac{\Delta x}{2}.\left(\frac{\partial^2 T}{\partial x^2}\right)_{x=i} - \frac{\Delta x^2}{3!}.\left(\frac{\partial^3 T}{\partial x^3}\right)_{x=1} + ...$$

$$\text{Or } T_{i-1} = T_i - \left(\frac{\partial T}{\partial x}\right)_i .\Delta x + \frac{\Delta x^2}{2}.\left(\frac{\partial^2 T}{\partial x^2}\right)_{x=i} - \frac{\Delta x^3}{3!}.\left(\frac{\partial^3 T}{\partial x^3}\right)_{x=i} + ...$$

Central difference of first order derivatives

Taking the expressions for the forward and backward differencing respectively

$$T_{i+1} = T_i + \left(\frac{\partial T}{\partial x}\right)_i .\Delta x + \frac{\Delta x^2}{2}.\left(\frac{\partial^2 T}{\partial x^2}\right)_{x=i} + \frac{\Delta x^3}{3!}.\left(\frac{\partial^3 T}{\partial x^3}\right)_{x=i} + \ldots\ldots \quad \mathbf{1}$$

$$T_{i-1} = T_i - \left(\frac{\partial T}{\partial x}\right)_i .\Delta x + \frac{\Delta x^2}{2}.\left(\frac{\partial^2 T}{\partial x^2}\right)_{x=i} - \frac{\Delta x^3}{3!}.\left(\frac{\partial^3 T}{\partial x^3}\right)_{x=i} + \ldots\ldots \quad \mathbf{2}$$

And subtracting 2 from 1 we get

$$T_{i+1} - T_{i-1} = \left(\frac{\partial T}{\partial x}\right)_i .\Delta x - \left(-\left(\frac{\partial T}{\partial x}\right)_i .\Delta x\right) + \frac{\Delta x^3}{3!}.\left(\frac{\partial^3 T}{\partial x^3}\right)_{x=i} - \left(-\frac{\Delta x^3}{3!}.\left(\frac{\partial^3 T}{\partial x^3}\right)_{x=i}\right) + \ldots\ldots$$

Which simplifies to

$$\left(\frac{\partial T}{\partial x}\right)_i = \frac{T_{i+1} - T_{i-1}}{2.\Delta x} - \frac{\Delta x^3}{3!}.\left(\frac{\partial^3 T}{\partial x^3}\right)_{x=i} + \ldots\ldots$$

Central difference of second order derivatives

Taking the expressions for the forward and backward differencing respectively

$$T_{i+1} = T_i + \left(\frac{\partial T}{\partial x}\right)_i .\Delta x + \frac{\Delta x^2}{2}.\left(\frac{\partial^2 T}{\partial x^2}\right)_{x=i} + \frac{\Delta x^3}{3!}.\left(\frac{\partial^3 T}{\partial x^3}\right)_{x=i} + \ldots\ldots$$

$$T_{i-1} = T_i - \left(\frac{\partial T}{\partial x}\right)_i .\Delta x + \frac{\Delta x^2}{2}.\left(\frac{\partial^2 T}{\partial x^2}\right)_{x=i} - \frac{\Delta x^3}{3!}.\left(\frac{\partial^3 T}{\partial x^3}\right)_{x=i} + \ldots\ldots$$

Adding these two expressions we get

$$T_{i+1} + T_{i-1} = 2T_i + \Delta x^2.\left(\frac{\partial\, T}{\partial x^2}\right) + \ldots\ldots$$

After rearranging we finally get

$$\left(\frac{\partial^2 T}{\partial x^2}\right)_i = \frac{T_{i+1} + T_{i-1} - 2T_i}{\Delta x^2} + \ldots\ldots$$

Selection of differencing scheme.

The central difference scheme for both the first and second order derivatives was second order accurate and considered to be more attractive due to the smaller truncation error. However, second order schemes required the values of the field variables (in this case temperature) to be known at cell I, cell $i\text{-}1$ and cell $i+1$.

Spatial discretisation.

Since at the present timestep the values of cell temperature T_i and the upstream and downstream cell temperatures T_{i+1} and T_{i-1} are known from the previous timestep a second order central differencing scheme for the spatial discretisation could be adopted.

Temporal discretisation.

Time discretisation

The time derivative $\frac{\partial T}{\partial t}$ in the governing equation $\frac{\partial T}{\partial t} = \alpha . \frac{\partial^2 T}{\partial x^2}$ was replaced with a forward difference formula.

i.e. $\frac{\partial T}{\partial t} = \frac{T_i^{n+1} - T_i^n}{\Delta t}$

Spatial discretisation

Similarly, the spatial derivative $\frac{\partial^2 T}{\partial x^2}$ in the governing equation $\frac{\partial T}{\partial t} = \alpha . \frac{\partial^2 T}{\partial x^2}$ was replaced with a central difference formula.

i.e. $\left(\frac{\partial^2 T}{\partial x^2} \right)_i = \frac{T_{i+1} + T_{i-1} - 2T_i}{\Delta x^2}$

These expressions were substituted into the original governing equation $\frac{\partial T}{\partial t} = \alpha . \frac{\partial^2 T}{\partial x^2}$

to give the following expression for T_i^{n+1}

$$T_i^{n+1} = T_i^n + \frac{\alpha . \Delta t}{\Delta x^2} . \left(T_{i+1} + T_{i-1} - 2T \right)$$

Since first order forward differencing has been applied to the time derivative, and second order central differencing has been applied to the spatial derivative, this scheme was described as a Forward Time, Centred Space method, which is hereafter denoted FTCS.

3.2 Finite Volume Methods.

Since it was intended to adopt integral methods for the solution of the unsteady Euler equations, an integral, or finite volume solution for the 1D conduction problem was also examined.

Considering the 1D domain to consist of a number of finite volumes as shown below

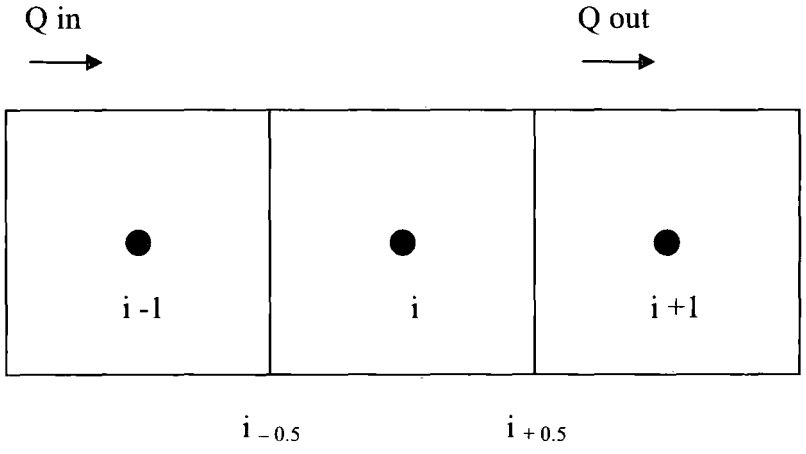

Figure 3.2.1

The heat flux into the cell i was given by $$Q_{in} = -k.A.\frac{\partial T}{\partial x}$$

Central differencing for cell $i_{-0.5}$ $$\frac{\partial T}{\partial x} = \frac{T_i - T_{i-1}}{\Delta x}$$

Therefore $$Q_{i-0.5} = -k.A.\frac{\partial T}{\partial x_{i-0.5}} = -k.A.\frac{T_i - T_{i-1}}{\Delta x}$$

Similarly the heat flux out of cell i was given by $$Q_{out} = -k.A.\frac{\partial T}{\partial x}$$

Central differencing for cell $i_{+0.5}$ $$\frac{\partial T}{\partial x} = \frac{T_{i+1} - T_i}{\Delta x}$$

Therefore $$Q_{i+0.5} = -k.A.\frac{\partial T}{\partial x_{i+0.5}} = -k.A.\frac{T_{i+1} - T_i}{\Delta x}$$

Now, considering a control volume about cell *i*. The energy stored in the control volume was given by $Q_{stored} = \dot{m}.Cp.\Delta T$ and the mass of the control volume was given by $\dot{m} = \rho.A.\Delta x$. Hence the element temperature T_i may be expressed as

$$\frac{Q_{stored}}{\rho.A.\Delta x.Cp} = T_i$$

Now, the energy stored in the element can be evaluated by considering a heat balance $Q_{in} - Q_{out} = Q_{stored}$ .Using the expression derived for Q_{in} and Q_{out} we could derive an expression for Q_{stored} as

$$k.A.\frac{T_i - T_{i-1}}{\Delta x} - k.A\frac{T_{i+1} - T_i}{\Delta x} = Q_{stored}$$

which can be rearranged as $Q_{stored} = k.A.\frac{T_{i+1} - 2T_i + T_{i-1}}{\Delta x}$

This represented the heat flux over the control volume for cell *i* at time $t = n$

At time $t=n+1$ $Q_i^{n+1} = Q_i^n + \Delta t.\left[\frac{\partial Q_i}{\partial t}\right]$ where $\frac{\partial Q_i}{\partial t} = k.A.\frac{T_{i+1} - 2T_i + T_{i-1}}{\Delta x}$

Isolating for Q_i^{n+1} we get

$$Q_i^{n+1} = Q_i^n + k.A.\Delta t..\left[\frac{T_{i+1}^n - 2T_i^n + T_{i-1}^n}{\Delta x}\right]$$

It has already been shown that the temperature within the cell is given by

$$T_i = \frac{Q_{stored}}{\rho.A.\Delta x.Cp}$$

Therefore substituting this into our expression for Q_i^{n+1} we get

$$T_i^{n+1} = T_i^n + \frac{k.A.\Delta t}{\rho..A..\Delta x.Cp}.\left[\frac{T_{i+1}^n - 2T_i^n + T_{i-1}^n}{\Delta x}\right]$$

Canceling and collecting like terms we finally arrive at the following expression

$$T_i^{n+1} = T_i^n + \frac{k.\Delta t}{\rho..Cp.\Delta x^2}.\left[T_{i+1}^n - 2T_i^n + T_{i-1}^n\right]$$

Which was seen to be identical for that derived using the differential method.

3.3 Stability Analysis And Convergence.

When devising a numerical scheme the concepts of stability and convergence must be addressed. Frequently stability criteria impose a limiting factor upon the maximum value of timestep permitted. The stability of a chosen numerical scheme can frequently be assessed using Von Neumann or discrete perturbation analysis methods. This was applied to the FTCS scheme as follows

Considering the original governing equation for heat conduction.

$$\frac{\partial T}{\partial t} = \alpha . \frac{\partial^2 T}{\partial x^2}$$

The FTCS numerical scheme was presented as

$$T_i^{n+1} = T_i^n + \frac{k.\Delta t}{\rho..Cp.\Delta x^2}.\left[T_{i+1}^n - 2T_i^n + T_{i-1}^n\right]$$

Or, for brevity

$$T_i^{n+1} = T_i^n + \frac{\alpha.\Delta t}{\Delta x^2}.\left[T_{i+1}^n - 2T_i^n + T_{i-1}^n\right] \quad \text{Where } \alpha = k/(\rho.Cp)$$

The discrete perturbation method allowed the propagation of errors to the next timestep to be estimated if the error values at the present timestep were known. Essentially if an error is introduced at grid point *i* at timestep T_i^n such that $T_i^n = T_i^n + \varepsilon$ where ε is the error value, then we can rewrite the differencing expression as

$$\varepsilon_i^{n+1} = T_i^n + \varepsilon + \frac{\alpha.\Delta t}{\Delta x^2}.\left[T_{i+1}^n - 2(T_i^n + \varepsilon) + T_{i-1}^n\right]$$

Starting with an initial value of the error of zero at all grid points, then T_i^n, T_{i+1}^n and T_{i-1}^n are all equal to zero, .i.e.

$$\varepsilon_i^{n+1} = 0 + \varepsilon + \frac{\alpha.\Delta t}{\Delta x^2}.\left[0 - 2(0 + \varepsilon) + 0\right]$$

$$\varepsilon_i^{n+1} = \varepsilon + \frac{\alpha.\Delta t}{\Delta x^2}.\left[-2\varepsilon\right]$$

$$\varepsilon_i^{n+1} = \varepsilon - 2\frac{\alpha.\Delta t}{\Delta x^2}\varepsilon \text{ or alternatively } \varepsilon_i^{n+1} = \varepsilon.\left(1 - 2\frac{\alpha.\Delta t}{\Delta x^2}\right)$$

This expression provided an error estimate for grid point *i* at timestep *n+1*.

For the solution to be stable, it was considered reasonable to assume that the errors must decrease in magnitude as the solution progresses. It was also considered that if the starting error at grid point *i* were given a value of 1, then the error at subsequent timesteps must lie between 0 and 1 if the scheme was stable. Returning to the expression for the error at grid point *i* at timestep n+1, it was possible to derive an expression for the error at this grid point for subsequent timesteps, i.e.

$$\varepsilon_i^{n+1} = \varepsilon.\left(1 - 2\frac{\alpha.\Delta t}{\Delta x^2}\right)$$

This could then be evaluated for the case of error sum equal to zero or unity, as below.

Considering the case where $\varepsilon_i^{n+1} = 1$

$$1 = 1.\left(1 - 2\frac{\alpha.\Delta t}{\Delta x^2}\right)$$

$$1 = 1 - 2\frac{\alpha.\Delta t}{\Delta x^2}$$

$$0 = 2\frac{\alpha.\Delta t}{\Delta x^2}$$

i.e. $$\frac{\alpha.\Delta t}{\Delta x^2} = 0$$

Considering the case where $\varepsilon_i^{n+1} = 0$

$$0 = 1.\left(1 - 2\frac{\alpha.\Delta t}{\Delta x^2}\right)$$

$$0 = 1 - 2\frac{\alpha.\Delta t}{\Delta x^2}$$

$$1 = 2\frac{\alpha.\Delta t}{\Delta x^2}$$

i.e. $$\frac{\alpha.\Delta t}{\Delta x^2} = \frac{1}{2}$$

From this analysis it appeared that for the FTCS differencing scheme to be stable, the value of $\frac{\alpha.\Delta t}{\Delta x^2}$ must lie between 0 and 0.5.

3.4 Numerical Damping and Dissipation.

The study of the one dimensional heat conduction problem undertaken previously had required the use of a first order backward differencing method to evaluate the spatial derivative as it had been found that a second order differencing scheme was unconditionally unstable. However it is widely known that first order schemes, whilst conditionally stable within limiting values of the Courant Number do suffer from numerical diffusion. Second order schemes based upon the use of central differencing methods for the spatial derivatives ought to yield a more accurate solution, however central differencing schemes tend to be unstable unless a small amount of numerical damping (often referred to as artificial viscosity) is introduced into the solution.

In order to study the effects of numerical diffusion it was elected to study the propagation of a rectangular waveform within a one dimensional domain. It was therefore proposed to consider the one dimensional wave equation employing both first order and second order approximations for the spatial derivatives. It was evident that two numerical schemes could be applied to the wave equation - a first order rearward difference upwind method and a second order central difference method. These were considered in turn.

3.4.1 First Order Upwind Scheme For The Wave Equation

Consider a wave traveling a distance Δx along the 1D duct at velocity u as in Figure 3.4.1.

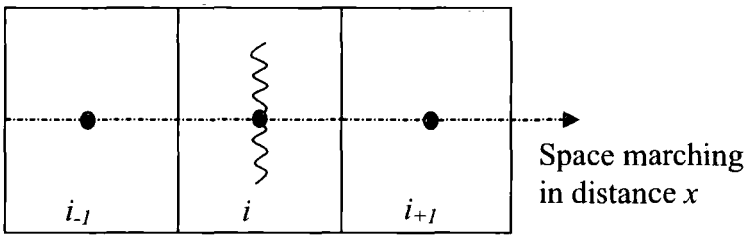

Figure 3.4.1

This could be represented using the 1D wave equation

$$\frac{\partial u}{\partial t} = -c.\frac{\partial u}{\partial x}$$

Employing a forward difference for the time derivative and a rearward difference for the spatial derivative the finite difference expression for the original equation now becomes.

$$\frac{\partial u}{\partial x} = \frac{u_i^n - u_{i-1}^n}{\Delta x} \qquad \text{Which can be rewritten as} \qquad \frac{u_i^{n+1} - u_i^n}{\Delta t} = -c.\frac{u_i^n - u_{i-1}^n}{\Delta x}$$

3.4.2 Numerical Experiments To Investigate Numerical Diffusion And Damping

The FTBS scheme applied to the one dimensional wave equation was solved numerically using a computer program written by the author. The program considered the linear advection of a square wave along a one dimensional domain in which the wave speed was taken to be constant and positive right running, hence the theoretical position of the wave within the domain could be easily calculated from the known wave speed and the solution elapsed time. The domain length was specified as being 100 metres and the wave velocity specified to be 1 metre per second. The grid size was calculated from the domain length and the user specified number of cells. The Courant number was variable and user specified. When running the program the user was prompted to enter the domain length, wave speed, Courant number and number of cells.

At the start of the solution the domain was initialised with the amplitude of all cells being set to zero. An initial waveform of width equal to $1/10^{th}$ of the cell count was applied in the first timestep and the propagation of the wave then computed at subsequent timesteps using the specified numerical scheme. For this study the rectangular waveform was chosen as this was considered to represent a more severe test of the scheme. Comparisons could be made to the exact solution which was generated by setting the Courant number to 1.0.

The studies were conducted on a 100, 200 and 1000 cell grid and at Courant Numbers ranging from 0.10 to 1.0, although for convenience only the results for the 200 cell grid obtained for a Courant Number equal to 0.50 are presented here. Figure 3.4.2 below shows the instantaneous pressure time waveform evaluated at a location half way between the inlet and outlet boundaries.

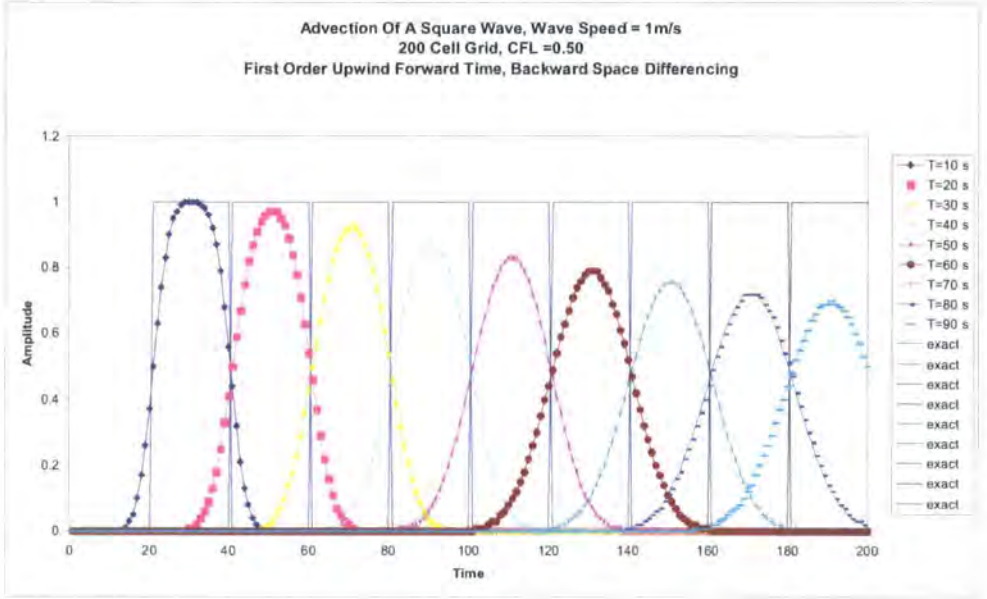

Figure 3.4.2

Numerical Solution - Discussion Of Results FTBS Scheme

Referring to Figure 3.4.2 it was found that the original square waveform was both damped (dissipated) and smoothed (dispersed) as the solution proceeded. In general the dissipation and dispersion increased as the number of timesteps increased, and as the Courant number was reduced. Comparison of results evaluated on the 100 and 200 cell grids indicated that whilst grid refinement reduced the dissipative and dispersive effects of the scheme, the first order upwind method resulted in a waveform that was both heavily dissipated and dispersed.

In order to understand why the first order scheme behaved in this way a Taylor Series expansion was applied to the original wave equation employing a forward difference for the time derivative , and a rearward difference for the spatial derivative the finite difference expression as follows.

$$\frac{u_i^{n+1}-u_i^n}{\Delta t}+c.\frac{u_i^n-u_{i-1}^n}{\Delta x}=0$$

Using a Taylor Series expansion for u_i^{n+1}

$$\frac{u_i^n+\Delta t.\frac{\partial u}{\partial t}+\frac{\Delta t^2}{2}.\frac{\partial^2 u}{\partial t^2}+\frac{\Delta t^3}{6}.\frac{\partial^3 u}{\partial t^3}-u_i^n}{\Delta t}+\frac{c}{\Delta x}.u_i^n-\left[u_i^n-\Delta x.\frac{\partial u}{\partial x}+\frac{\Delta x^2}{2}.\frac{\partial^2 u}{\partial x^2}-\frac{\Delta x^3}{6}.\frac{\partial^3 u}{\partial x^3}\right]=0$$

Rearranging and canceling like terms gives

$$\frac{\partial u}{\partial t}+c.\frac{\partial u}{\partial x}=\frac{-\Delta t}{2}.\frac{\partial^2 u}{\partial t^2}+\frac{c.\Delta x}{2}.\frac{\partial^2 u}{\partial x^2}-\frac{\Delta t^2}{6}.\frac{\partial^3 u}{\partial t^3}-\frac{c.\Delta x^2}{6}.\frac{\partial^3 u}{\partial x^3}$$

Which is seen to be the original wave equation plus an additional truncation term. Considerable evaluation and expansion of the derivatives (see Appendix 2) gives

$$\frac{\partial u}{\partial t}+c.\frac{\partial u}{\partial x}=\left[\frac{c.\Delta x}{2}-\frac{c^2\Delta t}{2}\right].\frac{\partial^2 u}{\partial x^2}+\left[-\frac{c^3\Delta t^2}{2}+\frac{c^2.\Delta x.\Delta t}{2}+\frac{c^3.\Delta t^2}{6}-\frac{c.\Delta x^2}{6}\right].\frac{\partial^3 u}{\partial x^3}$$

Now the timestep Δt may also be written in terms of the Courant Number (CFL), i.e.

$\Delta t=\frac{CFL.\Delta x}{c}$ so that finally we have an expression for the truncation, or damping term, i.e.

$$\frac{\partial u}{\partial t}+c.\frac{\partial u}{\partial x}=\frac{c.\Delta x}{2}[1-CFL].\frac{\partial^2 u}{\partial x^2}-\frac{c.\Delta x^2}{6}[2.CFL^2-3.CFL+1].\frac{\partial^3 u}{\partial x^3}$$

Now, from an examination of this modified equation it was apparent that as the Courant number was reduced the amount of damping increased, therefore giving the first order method it's strongly dissipative behaviour . In order to investigate this further, the effect of a change of Courant Number upon a square wave propogated along the 1D domain was studied. In order to allow the dissipative effects to adequately develop, the numerical results were evaluated at a time period corresponding to half way through the total solution time, in this case, at t = 50 seconds. The resulting waveforms evaluated on a 1000 cell grid are presented below as Figure 3.4.3.

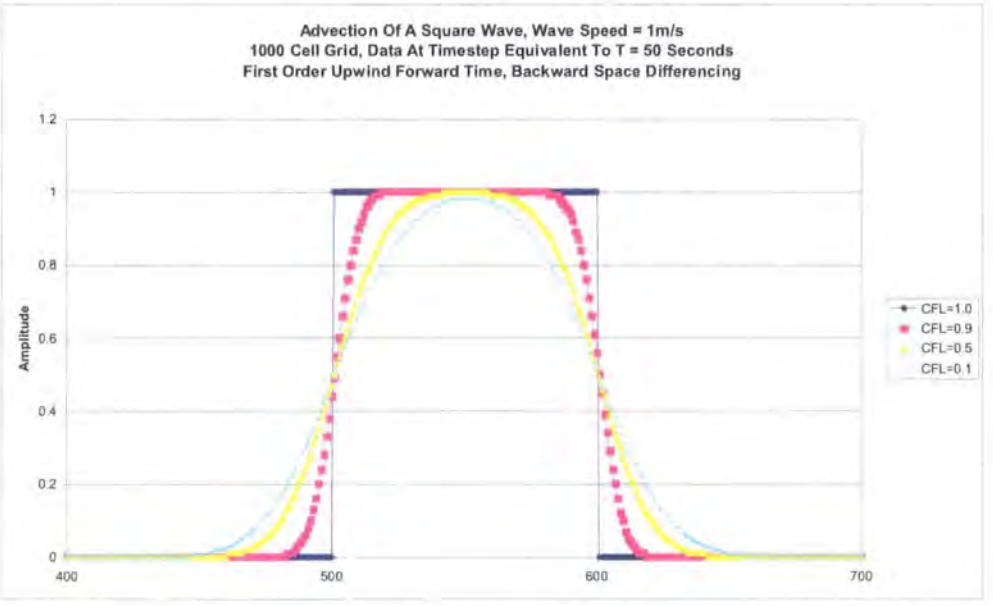

Figure 3.4.3

From an examination of Figure 3.4.3 it was obvious that a reduction of Courant number did indeed have significant dissipative and dispersive effects. At CFL = 1.0 no dissipation of the original square waveform is apparent, this was as expected from the study of the modified equation earlier. At a value of CFL = 0.90 a small amount of dissipation is evident although the dispersion of the waveform due to phase errors is significant resulting in a waveform shape more representative of a sinusoid. Further reduction of the Courant number resulted in increasing dissipation and dispersion of the original waveform such that at CFL=0.10 the waveform resembled more of a sinusoid than it's original square waveform.

Similar studies conducted on 100 and 200 cell grids indicated that whilst dissipative effects of the FTBS scheme could be relieved to some extent by an increase of grid resolution, the dispersive effects were still quite strong resulting in the eventual distortion of the original square waveform to a sinusoid, even on the 1000 cell grid.

3.5 The Need For Artificial Viscosity.

The first order upwind method whilst stable was found to be heavily damped and therefore considered to be of no use since its use would introduce unacceptable attenuation of the acoustic wave amplitudes. The second order central difference scheme whilst accurate suffered from numerical oscillations that ultimately led to divergence. However from an examination of the modified form of the wave equation it was reasoned that the addition of the truncation term could be used to dampen the oscillations inherent in the central differencing scheme and hence result in an accurate and stable solution.

3.5.1 Formulation Of The Artificial Viscosity Terms

Again considering the 1D wave equation and adopting Forward Time Backward Space differencing for positive wave speed c.

$$\frac{u_i^{n+1} - u_i^n}{\Delta t} + \frac{c.u_i^n - u_{i-1}^n}{\Delta x} = 0$$

And evaluating the time derivative using Taylor's Series such that

$$u_i^{n+1} = u_i^n + \frac{\partial u}{\partial t}\Delta t + \frac{\partial^2 u}{\partial t^2}\frac{\Delta t^2}{2} + \text{H.O.T.}$$

Now since $\frac{\partial u}{\partial t} = -c.\frac{\partial u}{\partial x}$ and $\frac{\partial^2 u}{\partial t^2} = c^2\frac{\partial^2 u}{\partial x^2}$

We can write $u_i^{n+1} = u_i^n - c\frac{\partial u}{\partial x}\Delta t + c^2.\frac{\partial^2 u}{\partial x^2}\frac{\Delta t^2}{2}$

Employing a Central Difference Scheme for the spatial derivatives, i.e.

$$\frac{\partial u}{\partial x} = \frac{u_{i+1} - u_{i-1}}{2\Delta x} \quad \text{and} \quad \frac{\partial^2 u}{\partial x^2} = \frac{u_{i+1} - 2u_i + u_{i-1}}{\Delta x^2}$$

We can now write

$$u_i^{n+1} = u_i^n - \frac{c\Delta t}{2\Delta x}.\left[u_{i+1}^n - u_{i-1}^n\right] + \frac{c^2.\Delta t^2}{2.\Delta x^2}.\left[u_{i=1}^n - 2u_i^n + u_{i-1}^n\right]$$

Which can be rewritten as

$$u_i^{n+1} = u_i^n - \frac{CFL}{2}.\left[u_{i+1}^n - u_{i-1}^n\right] + \frac{CFL^2}{2}.\left[u_{i=1}^n - 2u_i^n + u_{i-1}^n\right]$$

3.5.2 Numerical Experiment To Investigate Effect Of Adding Artificial Viscosity

The modified form of the wave equation was solved numerically. All program and domain parameters were identical to those adopted for the earlier FTBS scheme except the magnitude of the artificial viscosity coefficient was set to 2 percent. The studies were conducted on 100, 200 and 1000 cell grids and at Courant Numbers ranging from 0.10 to 1.0, although only the results for the 1000 cell grid obtained for a Courant Number equal to 0.50 are presented here. Figure 3.5.1 below shows the pressure time waveform evaluated at a location half way between the inlet and outlet boundaries. In addition, the effect of a change of Courant Number was evaluated in the same manner as before. The resulting time waveforms for Courant Numbers of 0.10, 0.50, 0.90 and 1.0 are shown below in Figure 3.5.2.

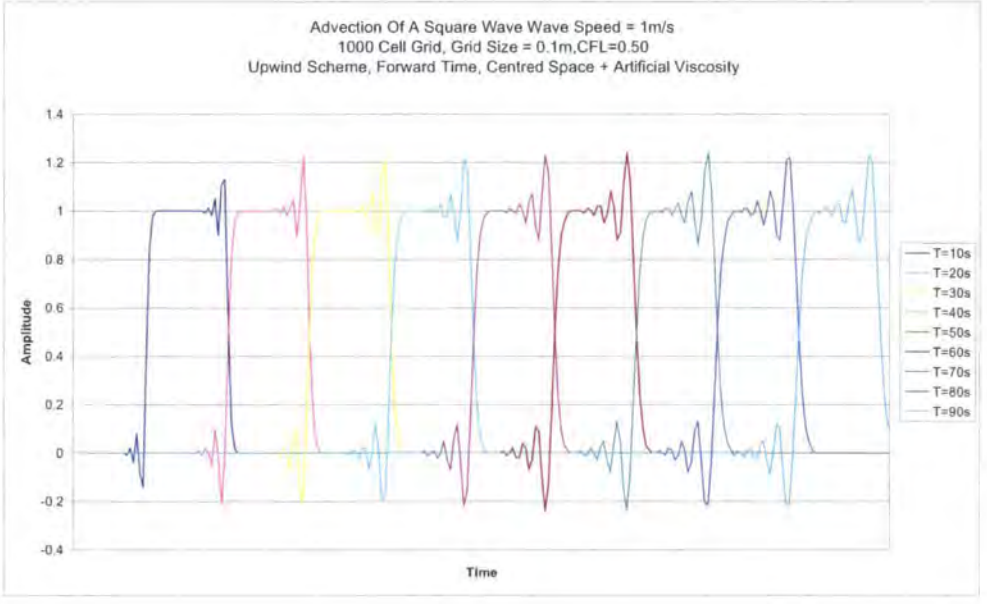

Figure 3.5.1

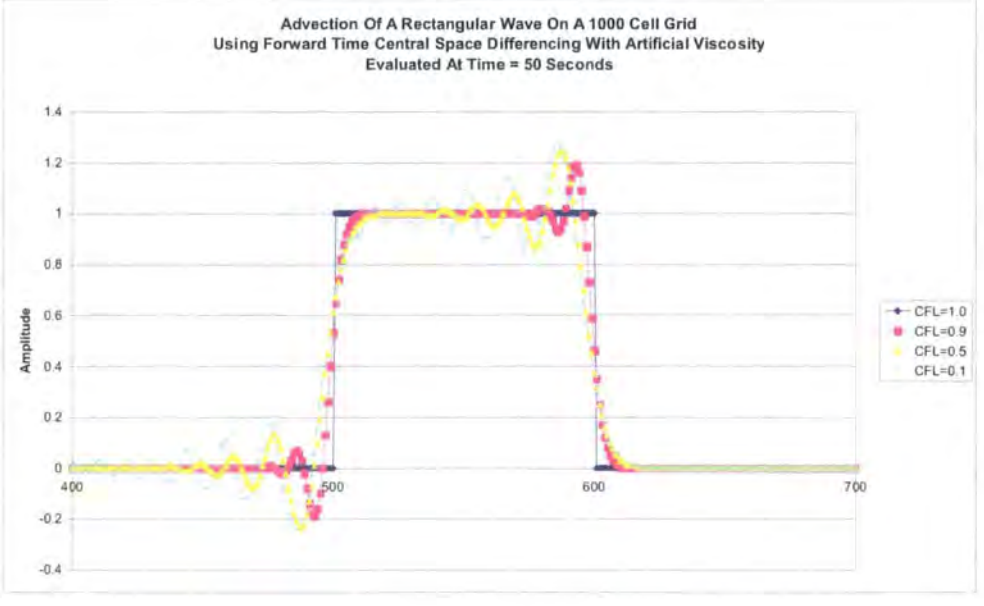

Figure 3.5.2

Discussion Of Results

It was found that the addition of artificial viscosity had a stabilizing effect on the FTCS scheme such that it became conditionally stable for values of the Courant Number equal to or less than 1.0. However it was found that new extrema were generated at the leading and trailing edges of the waveform where the gradients of velocity were greatest resulting in artificially high and negative wave amplitudes. These "ringing type" oscillations were found to increase in both their amplitude and their dispersive characteristics as the Courant Number was reduced or the number of timesteps increased. However from an examination of the results evaluated on the 100, 200 and 1000 cell grids it was found that grid refinement greatly reduced the dissipative and dispersive effects of the scheme.

Reduction of the Courant Number generally led to an increase in the amplitude of the extrema at the leading and trailing edges of the waveform, and also greater dispersion of the waveform resulting from the propagation of the 'ringing' oscillations from the waveform leading and trailing edges.

It was concluded that in order to minimize the effects of numerical diffusion using the FTCS scheme with artificial viscosity for a given wave speed the timestep and grid size should be chosen such as to maintain the value of the Courant Number at or close to 1.0. Adoption of low values of the Courant Number, whilst ensuring numerical stability would tend to increase numerical dissipation and dispersion errors within the scheme leading to increased numerical diffusion and hence reduced solution accuracy and slower convergence.

Having successfully developed a stable form of the FTCS scheme the next step was to apply the scheme to the solution of the Euler Equations. However it was also foreseen that this scheme would be of particular value for the acoustic studies to be undertaken later. The ability to change the inherent damping in the scheme by manipulation of the coefficient of artificial viscosity ought to facilitate convergence of a mean flow solution yet would also allow the damping in the scheme to be later reduced in a manner so as to minimize undesirable numerical dissipation of the physical acoustic wave behaviour.

3.6 Numerical Methods For The 1D Euler Equations

Having developed a conditionally stable form of the second order central differencing scheme for the 1D wave equation it was elected to adopt this method for the solution of the Euler equations. However, before proceeding with the intended study of the two dimensional Euler equations it was considered prudent to develop a solution for the one dimensional Euler equations (often referred to as a quasi 1D solution) as development of the numerical scheme and Fortran code would be simplified and the solution could be easily applied to the study of 1D nozzle flows for which analytical solutions existed. In this way the accuracy, stability and convergence properties of the numerical scheme could be evaluated before applying it to the more complex two dimensional study.

The development of the quasi 1D Euler scheme is presented below.

3.6.1 Forward Time Centred Space Scheme With Artificial Viscosity

Consider the flow of an isentropic gas through a one dimensional domain, represented by a nozzle of linear convergent profile as shown below in Figure 3.6.1.

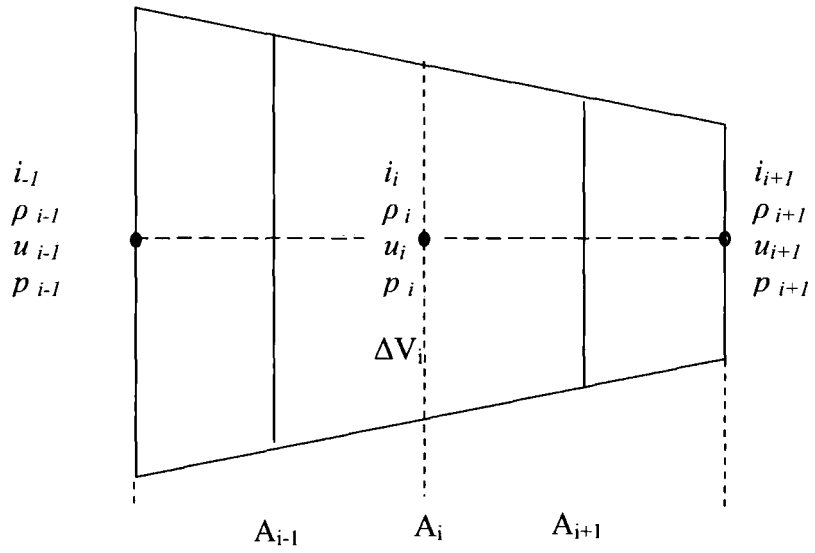

Figure 3.6.1

Governing Equations.

For the purpose of the study viscous effects at the walls was neglected and the flow computed using the inviscid Euler equations. These are given below.

Continuity

$$\frac{\partial \rho}{\partial t} + \frac{\partial \rho u}{\partial x} = 0$$

Momentum

$$\frac{\partial \rho u}{\partial t} + \frac{\partial \left(\rho . u^2 + p\right)}{\partial x} = 0$$

Energy

$$\frac{\partial (\rho . E)}{\partial t} + \frac{\partial (\rho . u . E + p . u)}{\partial x} = 0$$

It had already been determined that a rearward differencing scheme was found to be conditionally stable. Therefore the use of a rearward differencing scheme to approximate the spatial derivative was explored for the 1D Euler equations. In addition, since it was intended to adopt the finite volume method, it was necessary to develop a scheme where the flux quantities were evaluated over a cell volume. Considering again the 1D domain of Figure 3.6.1 and evaluating the mass flux using the continuity equation as an example.

$$\frac{\partial \rho}{\partial t} + \frac{\partial \rho u}{\partial x} = 0$$

The Flux stored in cell i is equal to the Flux $_{in}$ – Flux $_{out}$ This can be expressed as

$$\frac{\partial \rho}{\partial t} . \Delta V_i = (\rho u)_i A_i - (\rho u)_{i+1} A_{i+1}$$

Using a rearward differencing scheme for the left hand and right hand cell boundaries where the flux quantities are averaged over adjacent cells, an expression for the mass flux became.

$$\frac{\partial \rho}{\partial t} . \Delta V_i = \frac{(\rho u)_{i-1} + (\rho u)_i}{2} . A_i - \frac{(\rho u)_{i+1} + (\rho u)_i}{2} . A_{i+1}$$

Which could be simplified to

$$\frac{\partial \rho}{\partial t} . \Delta V_i = 0.5 . [(\rho u)_{i-1} + (\rho u)_i] . A_i - 0.5 . [(\rho u)_{i+1} + (\rho u)_i] . A_{i+1}$$

This therefore provided an expression to approximate the spatial derivative at time *n*. It can be seen that if this scheme were to be applied to the Euler equations, we now would possess a spatial solution for the flow variables at time *n*. Since our objective is to develop a scheme for the unsteady Euler equations, this solution could be marched forward in time to obtain a solution at the "future" time *n+1*. Therefore again, considering the simple case of the 1D continuity equation, if the time derivative was approximated by a forward difference, then the time rate change of density would be given by.

$$\frac{\partial \rho_i}{\partial t} = \frac{\rho_i^{n+1} - \rho_i^n}{\Delta t}$$

Rearranging so as to isolate ρ_i^{n+1} we get

$$\rho_i^{n+1} = \rho_i^n + \Delta t . \frac{\partial \rho_i}{\partial t}$$

Replacing the time derivative of density with our differencing expression we get

$$\rho_i^{n+1} = \rho_i^n + \frac{\Delta t}{V_i} . [[0.5.(\rho u_{i-1} + \rho u_i).A_i] - 0.5.[(\rho u_{i+1} + \rho u_i).A_{i+1}]]$$

Which is an expression for the density in cell *i* at future time *n+1*.

3.6.2 Selection Of Differencing Scheme For The Euler Equations.

Spatial Discretisation

Replacing the spatial derivatives with a rearward differencing expression averaged over adjacent cells as required by our finite volume method, the following expressions were obtained for the continuity, momentum and energy equations.

Continuity Equation

$$\frac{\partial \rho}{\partial t} + \frac{\partial \rho u}{\partial x} = 0$$

$$\frac{\partial \rho}{\partial t} . \Delta V_i = (\rho u_i).A_i - (\rho u)_{i+1} . A_{i+1}$$

$$\frac{\partial \rho}{\partial t} . \Delta V_i = \frac{(\rho u)_{i-1} + (\rho u)_i}{2} . A_i - \frac{(\rho u)_{i+1} + (\rho u)_i}{2} . A_{i+1}$$

$$\frac{\partial \rho}{\partial t} . \Delta V_i = 0.5.[(\rho u)_{i-1} + (\rho u)_i] A_i - 0.5.[(\rho u)_{i+1} + (\rho u)_i] A_{i+1}$$

Momentum Equation

$$\frac{\partial \rho u}{\partial t} + \frac{\partial \left(\rho.u^2 + p\right)}{\partial x} = 0$$

$$\frac{\partial \rho u}{\partial t}.\Delta V_i = \left(\rho u^2 + p\right)_i.A_i - \left(\rho u^2 + p\right)_{i+1}.A_{i+1}$$

$$\frac{\partial \rho u}{\partial t}.\Delta V_i = 0.5.\left[\left(\rho u^2 + p\right)_{i-1} + \left(\rho u^2 + p\right)_i\right]A_i - 0.5.\left[\left(\rho u^2 + p\right)_i + \left(\rho u^2 + p\right)_{i+1}\right]A_{i+1}$$

Energy Equation

$$\frac{\partial \left(\rho.E\right)}{\partial t} + \frac{\partial \left(\rho.u.E + p.u\right)}{\partial x} = 0$$

$$\frac{\partial \left(\rho.E\right)}{\partial t}.\Delta V_i = 0.5.\left[\left(\rho.u.E + p.u\right)_{i-1} + \left(\rho.u.E + p.u\right)_i\right]A_i - 0.5.\left[\left(\rho.u.E + p.u\right)_{i+1} + \left(\rho.u.E + p.u\right)_i\right]A_{i+1}$$

To eliminate the total internal energy E in the Energy Equation we have

$$E = e + \frac{u^2}{2} \text{ and } e = C_v.T_0 = \frac{R.T}{\gamma - 1}$$

From the equation of state $p = \rho.R.T$ we rearrange such that $T = \frac{p}{\rho.R}$

Therefore $e = C_v.T = \frac{R.T}{\gamma - 1} = \frac{R}{\gamma - 1}.\frac{p}{\rho.R} = \frac{1}{\gamma - 1}.\frac{p}{\rho}$

Therefore the total internal energy E is given by $E = \frac{1}{\gamma - 1}.\frac{p}{\rho} + \frac{u^2}{2}$

Alternatively, since ρE + p = ρH where H is Total Enthalpy, the energy can be re-written as

$$\frac{\partial \left(\rho.E\right)}{\partial t} + \frac{\partial \left(\rho.u.H\right)}{\partial x} = 0$$

i.e.

$$\frac{\partial \left(\rho.E\right)}{\partial t}.\Delta V_i = 0.5.\left[\left(\rho.u.H\right)_{i-1} + \left(\rho.u.H\right)_i\right]A_i - 0.5.\left[\left(\rho.u.H\right)_{i+1} + \left(\rho.u.H\right)_i\right]A_{i+1}$$

Since this expression was considered to be more computationally efficient it was used to evaluate the energy equation.

Time Marching.

To march the solution forward in time a forward difference method could be used for the continuity, momentum and energy equations, as shown below.

Continuity

$$\frac{\partial \rho_i}{\partial t} = \frac{\rho_i^{n+1} - \rho_i^n}{\Delta t} \text{ Therefore } \rho_i^{n+1} = \rho_i^n + \Delta t . \frac{\partial \rho_i}{\partial t},$$

$$\text{i.e. } \rho_i^{n+1} = \rho_i^n + 0.5 . \frac{\Delta t}{V_i} . [(\rho u_{i-1} + \rho u_i) . A_i - (\rho u_{i+1} + \rho u_i) . A_{i+1}]$$

Momentum

$$\frac{\partial \rho u_i}{\partial t} = \frac{\rho u_i^{n+1} - \rho u_i^n}{\Delta t} \text{ Therefore } \rho u_i^{n+1} = \rho u_i^n + \Delta t . \frac{\partial \rho u_i}{\partial t}$$

$$\text{i.e. } \rho u_i^{n+1} = \rho u_i^n + 0.5 . \frac{\Delta t}{V_i} . [((\rho u^2 + p)_{i-1} + (\rho u^2 + p)_i) . A_i - . ((\rho u^2 + p)_i + (\rho u^2 + p)_{i+1}) A_{i+1}]$$

Energy

$$\frac{\partial \rho E_i}{\partial t} = \frac{\rho E_i^{n+1} - \rho E_i^n}{\Delta t} \text{ Therefore } \rho E_i^{n+1} = \rho E_i^n + \Delta t . \frac{\partial \rho E_i}{\partial t}$$

$$\text{i.e. } \rho E_i^{n+1} = \rho E_i^n + 0.5 . \frac{\Delta t}{V_i} . [((\rho u H)_{i-1} + (\rho u H)_i) . A_i - . ((\rho u H)_i + (\rho u H)_{i+1}) A_{i+1}]$$

These expressions allowed the mass, momentum and energy fluxes to be calculated at future time $n+1$ from their present known values at time n.

3.6.3 Boundary Conditions.

For unsteady, compressible 1D flow four possible boundary conditions exist as follows [24]. At a subsonic inlet two characteristics enter the flow domain and one characteristic leaves the domain, therefore 2 physical boundary conditions (stagnation temperature and pressure) are specified and one numerical boundary condition is extrapolated from the interior. At a subsonic outlet one characteristic enters the flow domain and two characteristics leave the flow domain. Therefore one physical boundary condition (exit or static pressure) is specified and two numerical boundary conditions are extrapolated from the interior. At a supersonic inlet three characteristics enter the flow domain and no characteristics leave the domain. Therefore three physical boundary conditions are specified at a supersonic inlet. At a supersonic outlet no characteristics enter the flow domain and three characteristics leave the flow domain. Therefore no physical boundary conditions are specified and all three numerical boundary conditions are extrapolated from the interior.

3.6.4 Numerical Solution Of The 1D Euler Equations

Having derived a suitable form of the finite volume formulation for the 1D Euler equations a computer program was written by the author to perform the numerical computations. The construction of the code is briefly described below.

Considering the case of a simple 10 cell domain, a computational stencil may be drawn as follows.

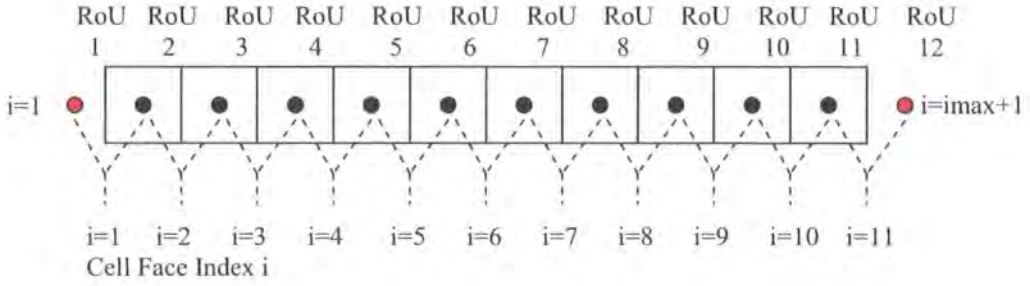

Figure 3.6.2

In this simple 10 cell stencil the boundary conditions have been defined by dummy nodes, shown coloured red. If the number of cells = 10 then the number of adjacent cell faces = 11 and the total number of locations is equal to the number of real cells + the two dummy nodes.

i.e. *ncells* = 10
imax = number of cell faces = ncells+1
total number of cell centres over which scheme is applied = *imax+1*
number of cell volumes in domain = *imax-1* (also equal to ncells)

Now in order to implement the scheme the mass, momentum and energy fluxes at the cell faces must be calculated, these could then be used to compute new updated values of the primitive flow variables in each cell centre.

3.6.5 Calculation of Flux Terms

For each cell the flux at cell centre *i* is given by

Flux at cell centre *i* = [(flux at cell face *i* + flux at cell face *i+1*)/2] * Area of face *i*

This was now applied to the continuity, momentum and energy equations in turn as follows.

Continuity Equation

The mass flux CMASS at cell centre i was given by

$$CMASS_i = 0.50 \times \left(\frac{ROU_i + ROU_{i+1}}{2} \right) \times Area_i$$

Knowing the values of CMASS at the cell faces, the value of density RO for cell i was calculated as follows.

$$RO_{i+1} = RO\_OLD_{i+1} + 0.50 \times \frac{\Delta t}{\Delta V_i} \times (CMASS_i - CMASS_{i+1})$$
$$+ SF \times (RO\_OLD_{i+2} - (2 \times RO\_OLD_{i+1}) + RO\_OLD_i)$$

Momentum Equation

The momentum flux XFLUX at cell centre i was given by

$$XFLUX_i = (CMASS_i \times U_i) + \left(\frac{P_i + P_{i+1}}{2} \right) \times Area_i$$

Knowing the values of XFLUX at the cell faces, the value of ROU for cell i was calculated as follows.

$$ROU_{i+1} = ROU\_OLD_{i+1} + 0.50 \times \frac{\Delta t}{\Delta V_i} \times ((XFLUX_i - XFLUX_{i+1}) + P\_SIDE_{i+1})$$
$$+ SF \times (ROU\_OLD_{i+2} - (2 \times ROU\_OLD_{i+1}) + ROU\_OLD_i)$$

Where the axial pressure force P_SIDE was given by

$$P\_SIDE_{i+1} = P_{i+1} \times (Area_{i+1} - Area_i)$$

Energy Equation

The energy flux, EFLUX at cell centre i was given by

$$XFLUX_i = CMASS_i \times \left(\frac{H_i + H_{i+1}}{2} \right)$$

Knowing the values of EFLUX at the cell faces, the value of ROE for cell i was calculated as follows.

$$ROE_{i+1} = ROE\_OLD_{i+1} + 0.50 \times \frac{\Delta t}{\Delta V_i} \times (EFLUX_i - EFLUX_{i+1})$$
$$+ SF \times (ROE\_OLD_{i+2} - (2 \times ROE\_OLD_{i+1}) + ROE\_OLD_i)$$

3.6.6 Calculation Of Primitive Variables

Referring again to the 10 cell stencil (Figure 3.6.2) it was now apparent that the values of RO, ROU and ROE were known at each interior cell centre within the domain. Therefore it became possible to calculate the primitive flow variables from the following relations.

Velocity U

$$U = \frac{\rho u}{\rho} \qquad \text{i.e. } U_i = \frac{ROU_i}{RO_i}$$

Static Pressure P

$$P = \left(\rho E - \frac{\rho . u^2}{2} \right) . \gamma - 1 \qquad \text{i.e. } P_i = \left(ROE_i - \frac{RO_i \times U_i^{\,2}}{2} \right) . \gamma - 1$$

Total Enthalpy H

$$H = \frac{\rho . E + P}{\rho} \qquad \text{i.e. } H_i = \frac{ROE_i + P_i}{RO_i}$$

Static Temperature T

$$T = \frac{P}{\rho . R} \qquad \text{i.e. } T_i = \frac{P_i}{RO_i \times R}$$

Local Sonic Velocity C

$$c = \sqrt{\gamma . R . T} \qquad \text{i.e. } C_i = \sqrt{\gamma \times R \times T_i}$$

Mach Number M

$$M = \frac{u}{c} \qquad \text{i.e. } M_i = \frac{u_i}{c_i}$$

3.6.7 Boundary Condition Implementation - Inlet

For the case of a subsonic flow at the inlet boundary it was known that two characteristics must enter the flow domain and one characteristic must leave the domain, therefore 2 physical boundary conditions must be specified and one numerical boundary condition must be calculated from the interior domain.

Since it was reasonable to assume that the stagnation pressure P0 and stagnation temperature T0 would be known physical boundary conditions at the inlet, if the static pressure were also known at the inlet this would enable calculation of the inlet Mach Number and subsequently all other primitive flow variables at the inlet.

Therefore at the inlet the two physical boundary conditions specified were the stagnation pressure P0 and stagnation temperature T0. The numerical boundary condition was taken to be the static pressure, calculated by extrapolation from the interior as follows.

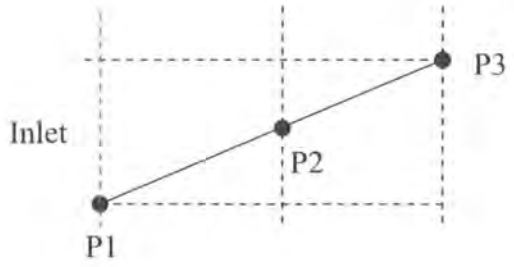

Figure 3.6.3

The gradient, m , of static pressure P evaluated between interior cell centres P2 and P3 was given by the following expression.

$$m = \frac{P3 - P2}{\Delta x}$$

And from the linear relation $y = mx + c$ we see that to obtain the pressure P1 we could write

$$P1 = P2 - \left(\frac{P3 - P2}{\Delta x} \right) \times \Delta x$$

Which becomes

P1 = P2- (-P2) – P3 i.e. P1 = 2P2-P3

The calculation of each of the primitive flow variables at the inlet boundary is described as follows.

Mach Number At Inlet

With the stagnation pressure P0 and the static pressure P at the inlet boundary known, using the isentropic flow relations the inlet Mach Number could be calculated as follows.

From $\frac{P_0}{P} = \left(1 + \frac{\gamma - 1}{2}.M^2\right)^{\frac{\gamma}{\gamma - 1}}$ Rearranging gives $\left(\frac{P_0}{P}\right)^{\frac{\gamma - 1}{\gamma}} = 1 + \frac{\gamma - 1}{2}.M^2$

Rearranging further such that

$$\frac{2}{\gamma - 1}.\left[\left(\frac{P_0}{P}\right)^{\frac{\gamma - 1}{\gamma}} - 1\right] = M^2 \qquad \text{i.e. } M = \sqrt{\frac{2}{\gamma - 1}.\left[\left(\frac{P_0}{P}\right)^{\frac{\gamma - 1}{\gamma}} - 1\right]}$$

Static Temperature At Inlet

$\frac{T_0}{T} = 1 + \frac{\gamma - 1}{2}.M^2$ Rearranging gives $T = \frac{T_0}{1 + \frac{\gamma - 1}{2}.M^2}$

Velocity U At Inlet

$$T_0 = T + \frac{U^2}{2.Cp} \qquad \text{where } Cp = \frac{\lambda.R}{\gamma - 1}$$

Therefore we can write $(T_0 - T).2Cp = U^2$

i.e. $U = \sqrt{2.(T_0 - T).\frac{\gamma.R}{\gamma - 1}}$

Density At Inlet

$$\rho = \frac{P}{R.T}$$

Sonic Velocity At Inlet

$$c = \sqrt{\gamma.R.T}$$

Total Enthalpy H At Inlet

$$H = \frac{\rho E + P}{\rho}$$

3.6.8 Boundary Condition Implementation - Outlet

For the case of a subsonic flow at the outlet boundary it was known that one characteristic must enter the flow domain and two characteristics must leave the domain. Therefore 1 physical boundary condition must be specified and two numerical boundary conditions must be calculated from the interior domain.

Since the backpressure or static pressure downstream was known, this could be prescribed as the physical boundary condition downstream. If ρU and ρE were extrapolated from the interior of the domain to the outlet boundary, then these 3 boundary conditions would permit calculation of the outlet velocity U and subsequently all other primitive flow variables at the outlet boundary. Therefore at the outlet one physical boundary condition was specified (static pressure) and two numerical boundary conditions (ρU and ρE) were extrapolated from the interior in the same manner as that employed at the inlet as shown below in Figure 3.6.4

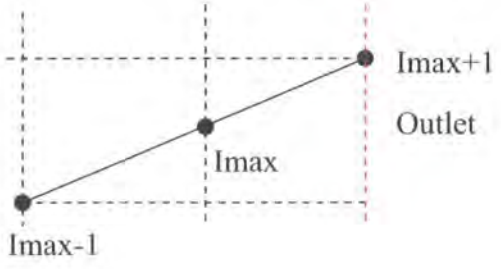

Figure 3.6.4

The gradient, m, of ρU evaluated between interior cell centres Imax and Imax-1 was given by $m = \dfrac{\rho U_{\mathrm{Im}ax-1} - \rho U_{\mathrm{Im}ax}}{\Delta x}$

And by again using the linear relation $y = mx + c$, we see that to obtain the value of ρU at the outlet boundary, $\rho U_{\mathrm{imax+1}}$ we could write

$$\rho U_{\mathrm{Im}ax+1} = \rho U_{\mathrm{Im}ax} - \left(\frac{\rho U_{i\max-1} - \rho U_{i\max}}{\Delta x} \right) \times \Delta x$$

Which becomes

$\rho U_{\mathrm{Imax+1}} = \rho U_{\mathrm{Imax}} - (-\rho U_{\mathrm{Imax}}) - \rho U_{\mathrm{Imax-1}}$, i.e. $\rho U_{\mathrm{Imax+1}} = 2.\ \rho U_{\mathrm{Imax}} - \rho U_{\mathrm{Imax-1}}$

Similarly we could calculate ρE at the outlet boundary as

$\rho E_{\mathrm{Imax+1}} = 2.\ \rho E_{\mathrm{Imax}} - \rho E_{\mathrm{Imax-1}}$

With ρU, ρE and the static pressure now known at the outlet boundary the calculation of the primitive flow variables at the outlet could proceed as follows.

Velocity U At Outlet

Conservative variables ρE and ρU were extrapolated from the interior of the domain to the outlet boundary.

Now the Specific Total Energy E was given by $E = \rho E / \rho$

Which could also be expressed as

$$E = \frac{P}{(\gamma - 1).\rho} + 0.5.U^2$$

Therefore, multiplying throughout by ρ we obtained

$$\rho E = \frac{P}{\gamma - 1} + \frac{\rho U.U}{2}$$

Simplifying and isolating for the local velocity U we obtained the following expression for U

$$\frac{2.\left[\rho E - \frac{P}{\gamma - 1}\right]}{\rho U} = U$$

Local Density At Outlet

$$\rho = \frac{\rho U}{U}$$

Local Temperature At Outlet

$$T = \frac{P}{\rho.R}$$

Local Sonic Velocity At Outlet

$$c = \sqrt{\gamma.R.T}$$

Local Mach Number At Outlet

$$M = \frac{U}{c}$$

Total Enthalpy H At Outlet

$$H = \frac{\rho E + P}{\rho}$$

3.7 Numerical Methods For The 2 D Euler Equations.

Having developed an accurate, stable and easily implemented finite volume scheme for the one dimensional Euler equations it was elected to extend this method for the solution of the Euler equations in two dimensions. Whilst the fundamental form of the numerical scheme remained unchanged, the scheme was amended to include the additional flux calculations and wall boundary conditions required for a two dimensional study.

3.7.1 Governing Equations.

For the purpose of the study viscous effects at the walls was neglected and the flow computed using the two dimensional inviscid Euler equations. These are given below.

Continuity

$$\frac{\partial}{\partial t}.\rho = \frac{\partial}{\partial x}.\rho u + \frac{\partial}{\partial y}.\rho v$$

X Momentum

$$\frac{\partial}{\partial t}.\rho u = \frac{\partial}{\partial x}.\left(\rho u^2 + p\right) + \frac{\partial}{\partial y}.(\rho uv)$$

Y Momentum

$$\frac{\partial}{\partial t}.\rho v = \frac{\partial}{\partial x}.(\rho uv) + \frac{\partial}{\partial y}.\left(\rho v^2 + p\right)$$

Energy

$$\frac{\partial}{\partial t}.E = \frac{\partial}{\partial x}.(E + p)u + \frac{\partial}{\partial y}.(E + p)v$$

Alternatively this may be re written as

$$\frac{\partial}{\partial t}.\rho E = \frac{\partial}{\partial x}.(\rho.u.H) + \frac{\partial}{\partial y}.(\rho.v.H)$$

Where

$$E = \frac{p}{\gamma - 1} + 0.5.\rho.\left(u^2 + v^2\right)$$

Forward Time Centred Space Scheme With Artificial Viscosity

Following on from the work undertaken for the 1D Euler studies it was elected to use the same central differenced method with the addition of artificial viscosity, with the flux quantities of mass, momentum and energy evaluated over a cell volume using the finite volume method as before. The development of the two dimensional Euler scheme is presented below. A program flowchart for the 2D Euler code is presented in Appendix 1.

Consider the flow through a two dimensional domain, represented below in Figure 3.7.1.

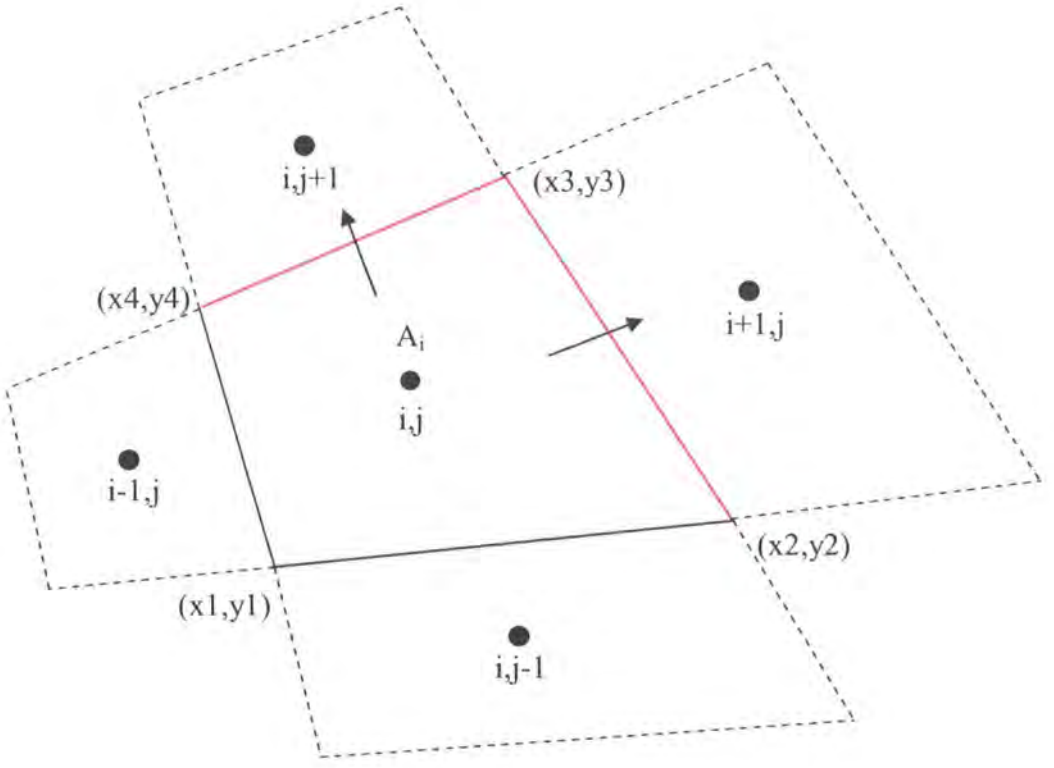

Figure 3.7.1

3.7.2 Evaluation Of 2D Continuity Equation.

To evaluate the mass fluxes across the cell faces consider Figure 3.7.2 below.

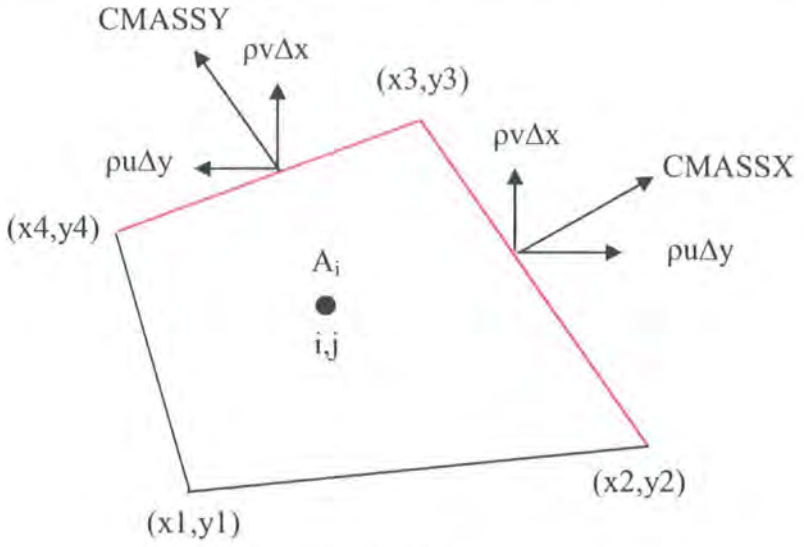

Figure 3.7.2

The mass flux across face 2-3, denoted CMASSX is given as

$$CMASSX = 0.50.\left[\left(\rho u\Delta y + \rho v\Delta x\right)_{i,j} + \left(\rho u\Delta y + \rho v\Delta x\right)_{i+1,j}\right]$$

i.e.

$$CMASSX = 0.50.\left(\rho u_{i,j} + \rho u_{i+1,j}\right).y_3 - y_2 - 0.50.\left(\rho v_{i,j} + \rho v_{i+1,j}\right).x_3 - x_2$$

The mass flux across face 3-4, denoted CMASSY is given as

$$CMASSY = 0.50.\left[\left(\rho u\Delta y + \rho v\Delta x\right)_{i,j} + \left(\rho u\Delta y + \rho v\Delta x\right)_{i,j+1}\right], \text{ or}$$

$$CMASSY = -0.50.\left(\rho u_{i,j} + \rho u_{i,j+1}\right).y_3 - y_4 + 0.50.\left(\rho v_{i,j} + \rho v_{i,j+1}\right).x_3 - x_4$$

Having generated expressions for the mass flux across faces 2-3 and 3-4, the cell centred value of density may be calculated using the continuity update expression shown below.

$$RO_{i,j} = RO\_OLD_{i,j} + RK \times \frac{Tstep}{Vol_i} \times \left[\left(CMASSX_{i,j} - CMASSX_{i+1,j}\right) + \left(CMASSY_{i,j} - CMASSY_{i,j+1}\right)\right]$$

Where RO_OLD is the value of RO calculated in the previous timestep. RK is the value of the Runge Kutta coefficient. Tstep is the timestep in seconds and Vol is the cell volume = cell area x unit depth (unit depth taken to be 1.0)

3.7.3 Evaluation Of 2D X Momentum Equation.

To evaluate the X-momentum fluxes across the cell faces consider Figure 3.7.3 below.

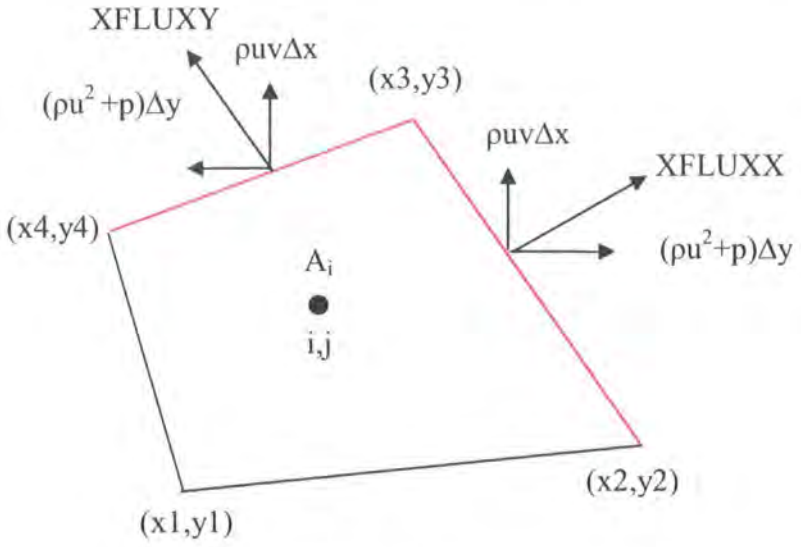

Figure 3.7.3

The X component of X momentum flux across face 2-3, denoted XFLUXX is given as

$$XFLUXX_{i,j} = 0.50.\left[\left(\left(\rho u^2 + p\right)\Delta y + \left(\rho uv\Delta x\right)\right)_{i,j} + \left(\left(\rho u^2 + p\right)\Delta y + \left(\rho uv\Delta x\right)\right)_{i+1,j}\right]$$

which can also be expressed using the conservative variable CMASSX as

$$XFLUXX_{i,j} = CMASSX_{i,j} \times 0.50.\left(u_{i,j} + u_{i+1,j}\right) + 0.50.\left(p_{i,j} + p_{i+1,j}\right).y_3 - y_2$$

The Y component of X momentum flux across face 3-4, denoted XFLUXY is given as

$$XFLUXY_{i,j} = 0.50.\left[\left(\left(\rho u^2 + p\right)\Delta y + \left(\rho uv\Delta x\right)\right)_{i,j} + \left(\left(\rho u^2 + p\right)\Delta y + \left(\rho uv\Delta x\right)\right)_{i,j+1}\right]$$

which can also be expressed using the conservative variable CMASSY as

$$XFLUXY_{i,j} = CMASSY_{i,j} \times 0.50.\left(u_{i,j} + u_{i,j+1}\right) - 0.50.\left(p_{i,j} + p_{i,j+1}\right).y_3 - y_4$$

Having expressions for the X-momentum flux across faces 2-3 and 3-4, the cell centred value of the conservative variable ROU may be calculated using the X momentum update expression shown below.

$$ROU = ROU\_OLD + RK \times \frac{Tstep}{Vol_i} \times \left[\left(XFLUXX_{i,j} - XFLUXX_{i+1,j}\right) + \left(XFLUXY_{i,j} - XFLUX_{i,j+1}\right)\right]$$

Where ROU_OLD is the value of ROU calculated in the previous timestep, RK is the value of the Runge Kutta coefficient, Tstep is the timestep in seconds and Vol is the cell volume = cell area x unit depth (unit depth taken to be 1.0)

3.7.4 Evaluation Of 2D Y Momentum Equation.

To evaluate the Y-momentum fluxes across the cell faces consider Figure 3.7.4 below.

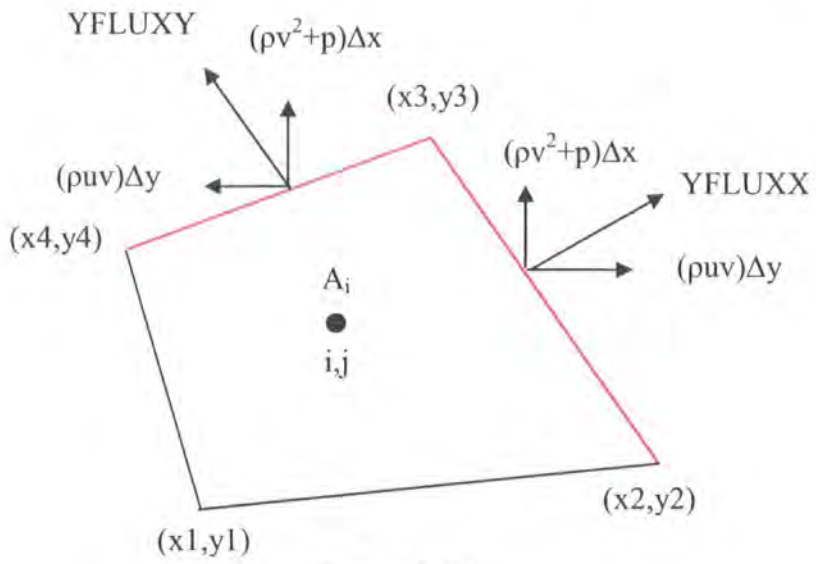

Figure 3.7.4

The X component of Y momentum flux across face 2-3, denoted YFLUXX is given as

$$YFLUXX_{i,j} = 0.50.\left[\left(\left(\rho v^2 + p\right)\Delta x + \left(\rho uv\Delta y\right)\right)_{i,j} + \left(\left(\rho v^2 + p\right)\Delta x + \left(\rho uv\Delta y\right)\right)_{i+1,j}\right]$$

which can also be expressed using the conservative variable CMASSX as

$$YFLUXX_{i,j} = CMASSX_{i,j} \times 0.50.\left(v_{i,j} + v_{i+1,j}\right) - 0.50.\left(p_{i,j} + p_{i+1,j}\right).x_3 - x_2$$

The Y component of Y momentum flux across face 3-4, denoted YFLUXY is given as

$$XFLUXY_{i,j} = 0.50.\left[\left(\left(\rho v^2 + p\right)\Delta x + \left(\rho uv\Delta y\right)\right)_{i,j} + \left(\left(\rho v^2 + p\right)\Delta x + \left(\rho uv\Delta y\right)\right)_{i,j+1}\right]$$

which can also be expressed using the conservative variable CMASSY as

$$YFLUXY_{i,j} = CMASSY_{i,j} \times 0.50.\left(v_{i,j} + v_{i,j+1}\right) + 0.50.\left(p_{i,j} + p_{i,j+1}\right).x_3 - x_4$$

Having generated expressions for the Y-momentum flux across faces 2-3 and 3-4, the cell centred value of the conservative variable ROV may be calculated using the Y momentum update expression shown below.

$$ROV_{i,j} = ROV\_OLD_{i,j} + RK \times \frac{Tstep}{Vol_i} \times \left[\left(YFLUXX_{i,j} - YFLUXX_{i+1,j}\right) + \left(YFLUXY_{i,j} - YFLUX_{i,j+1}\right)\right]$$

Where ROV_OLD is the value of ROV calculated in the previous timestep, RK is the value of the Runge Kutta coefficient, Tstep is the timestep in seconds and Vol is the cell volume = cell area x unit depth (unit depth taken to be 1.0)

3.7.5 Evaluation Of 2D Energy Equation.

To evaluate the energy fluxes across the cell faces consider Figure 3.7.5 below.

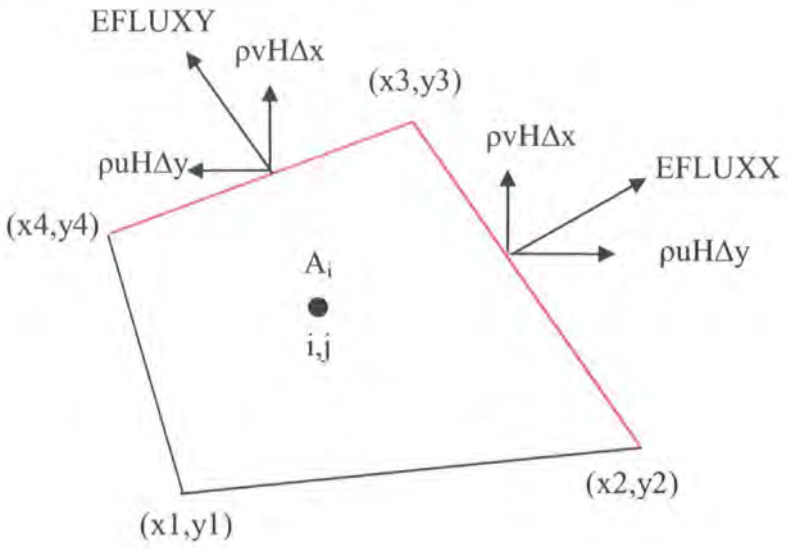

Figure 3.7.5

The energy flux across face 2-3, denoted EFLUXX is given as

$$EFLUXX = 0.50.\left[\left(\rho uH\Delta y + \rho vH\Delta x\right)_{i,j} + \left(\rho uH\Delta y + \rho vH\Delta x\right)_{i+1,j}\right]$$

i.e.

$$EFLUXX = CMASSX \times 0.50.\left(H_{i,j} + H_{i+1,j}\right)$$

The energy flux across face 3-4, denoted EFLUXY is given as

$$EFLUXY = 0.50.\left[\left(\rho uH\Delta y + \rho vH\Delta x\right)_{i,j} + \left(\rho uH\Delta y + \rho vH\Delta x\right)_{i,j+1}\right], \text{ or}$$

$$EFLUXY = CMASSY \times 0.50.\left(H_{i,j} + H_{i,j+1}\right)$$

Having generated expressions for the mass flux across faces 2-3 and 3-4, the cell centred value of the conservative variable ROE may be calculated using the energy update expression shown below.

$$ROE_{i,j} = ROE\_OLD_{i,j} + RK \times \frac{Tstep}{Vol_i} \times \left[\left(EFLUXX_{i,j} - EFLUXX_{i+1,j}\right) + \left(EFLUXY_{i,j} - EFLUXY_{i,j+1}\right)\right]$$

Where ROE_OLD is the value of ROE calculated in the previous timestep, RK is the value of the Runge Kutta coefficient, Tstep is the timestep in seconds and Vol is the cell volume = cell area x unit depth (unit depth taken to be 1.0)

3.7.6 Construction Of Artificial Viscosity Terms.

It had already been determined that the central differencing employed for the spatial differences in the chosen scheme required the addition of an artificial viscosity term to dampen high frequency oscillatory behaviour. The artificial viscosity was added at the update stage for the continuity, momentum and energy equations resulting. The update expressions for RO, ROU,ROV and ROE therefore became.

Continuity Update

$$RO_{i,j} = RO\_OLD_{i,j} + RK \times \frac{Tstep}{Vol_i} \times \left[\left(CMASSX_{i,j} - CMASSX_{i+1,j}\right) + \left(CMASSY_{i,j} - CMASSY_{i,j+1}\right)\right]$$
$$+ SF \times \left(RO\_OLD_{i+1} - .\left(2 \times RO\_OLD_i\right) + RO\_OLD_{i-1}\right)$$
$$+ SF \times \left(RO\_OLD_{j+1} - .\left(2 \times RO\_OLD_j\right) + RO\_OLD_{j-1}\right)$$

X momentum update

$$ROU_{i,j} = ROU\_OLD_{i,j} + RK \times \frac{Tstep}{Vol_i} \times \left[\left(XFLUXX_{i,j} - XFLUX_{i+1,j}\right) + \left(XFLUXY_{i,j} - XFLUXY_{i,j+1}\right)\right]$$
$$+ SF \times \left(ROU\_OLD_{i+1} - .\left(2 \times ROU\_OLD_i\right) + ROU\_OLD_{i-1}\right)$$
$$+ SF \times \left(ROU\_OLD_{j+1} - .\left(2 \times ROU\_OLD_j\right) + ROU\_OLD_{j-1}\right)$$

Y momentum update

$$ROV_{i,j} = ROV\_OLD_{i,j} + RK \times \frac{Tstep}{Vol_i} \times \left[\left(YFLUXX_{i,j} - YFLUX_{i+1,j}\right) + \left(YFLUXY_{i,j} - YFLUXY_{i,j+1}\right)\right]$$
$$+ SF \times \left(ROV\_OLD_{i+1} - .\left(2 \times ROV\_OLD_i\right) + ROV\_OLD_{i-1}\right)$$
$$+ SF \times \left(ROV\_OLD_{j+1} - .\left(2 \times ROV\_OLD_j\right) + ROV\_OLD_{j-1}\right)$$

Energy update

$$ROE_{i,j} = ROE\_OLD_{i,j} + RK \times \frac{Tstep}{Vol_i} \times \left[\left(EFLUXX_{i,j} - EFLUX_{i+1,j}\right) + \left(EFLUXY_{i,j} - EFLUXY_{i,j+1}\right)\right]$$
$$+ SF \times \left(ROE\_OLD_{i+1} - .\left(2 \times ROE\_OLD_i\right) + ROE\_OLD_{i-1}\right)$$
$$+ SF \times \left(ROE\_OLD_{j+1} - .\left(2 \times ROE\_OLD_j\right) + ROE\_OLD_{j-1}\right)$$

Where SF was the artificial viscosity smoothing coefficient and was generally set to 0.02 corresponding to a value of 2 percent.

3.7.7 Calculation Of Primitive Variables

With the numerical values of the conservative variables RO, ROU, ROV and ROE known at each interior cell centre within the domain it now became possible to calculate the primitive flow variables from the following relations.

Velocity U

$$U = \frac{\rho u}{\rho} \qquad \text{i.e. } U_{ij} = \frac{ROU_{ij}}{RO_{ij}}$$

Velocity V

$$V = \frac{\rho v}{\rho} \qquad \text{i.e. } V_{ij} = \frac{ROE_{ij}}{RO_{ij}}$$

Velocity Magnitude VEL

$$V = \sqrt{u^2 + v^2} \qquad \text{i.e. } V_{ij} = \sqrt{u_{ij}^{\ 2} + v_{ij}^{\ 2}}$$

Energy E

$$E = \frac{\rho E}{\rho} \qquad \text{i.e. } V_{ij} = \frac{ROV_{ij}}{RO_{ij}}$$

Static Pressure P

$$P = \rho.(\gamma - 1) \times \left(E - 0.5.\left(u^2 + v^2\right)\right) \qquad \text{i.e. } P_{ij} = RO_{ij}.(\gamma - 1) \times \left(E_{ij} - 0.5.\left(u_{ij}^{\ 2} + v_{ij}^{\ 2}\right)\right)$$

Total Enthalpy H

$$H = E + \frac{P}{\rho} \qquad \text{i.e. } H_{ij} = E_{ji} + \frac{P_{ij}}{RO_{ij}}$$

Static Temperature T

$$T = \frac{P}{\rho.R} \qquad \text{i.e. } T_{ij} = \frac{P_{ij}}{RO_{ij} \times R}$$

Local Sonic Velocity C

$$c = \sqrt{\gamma.R.T} \qquad \text{i.e. } C_{ij} = \sqrt{\gamma \times R \times T_{ij}}$$

Local Mach Number M

$$M = \frac{\sqrt{u^2 + v^2}}{\sqrt{(\gamma.P)/\rho}} \qquad \text{i.e. } M_{ij} = \frac{\sqrt{u_{ij}^{\ 2} + v_{ij}^{\ 2}}}{\sqrt{(\gamma.P_{ij})/RO_{ij}}}$$

3.7.8 Boundary Condition Implementation - Inlet

Assuming a subsonic inlet and subsonic outlet, then as before values for the stagnation pressure P0 and stagnation temperature T0 were prescribed at the inlet and a value for the static pressure prescribed at the outlet. Extrapolation of numerical boundary conditions at the inlet and outlet where required were undertaken in the same manner as in the Euler1D code. The flow variables at the inlet boundary were calculated as follows.

Mach Number At Inlet

$$M = \sqrt{\frac{2}{\gamma - 1}.\left[\left(\frac{P_0}{P}\right)^{\frac{\gamma-1}{\gamma}} - 1\right]}$$

Static Temperature At Inlet

$$T = \frac{T_0}{1 + \frac{\gamma - 1}{2}.M^2}$$

Sonic Velocity At Inlet

$$c = \sqrt{\gamma.R.T}$$

Velocity Magnitude At Inlet

i.e. $$VEL = \sqrt{2.(T_0 - T).\frac{\gamma.R}{\gamma - 1}}$$

U Velocity At Inlet

Assuming the flow enters normal to the inlet boundary, then the local U velocity would be equal to the velocity magnitude VEL.

V Velocity At Inlet

Assuming the flow enters normal to the inlet boundary, then the local V velocity would be equal to zero.

Density At Inlet

$$\rho = \frac{P}{R.T}$$

Total Energy E At Inlet

$$E = \frac{\rho.E}{\rho}$$

Total Enthalpy H At Inlet

$$H = E + \frac{P}{\rho}$$

3.7.9 Boundary Condition Implementation - Outlet

For the two dimensional study the boundary conditions were implemented in an identical manner to that employed for the previous one dimensional study, i.e. a subsonic inlet and subsonic outlet were specified. Therefore, at the outlet the static pressure was specified and the conservative variables ρU and ρE were extrapolated from the interior. In addition the conservative variable ρ was also extrapolated from the interior. The flow variables at the inlet boundary were calculated as follows.

U Velocity At Outlet

$$U = \frac{\rho U}{\rho}$$

V Velocity At Outlet

$$V = \frac{\rho V}{\rho}$$

Temperature At Outlet

$$T = \frac{P}{\rho . R}$$

Sonic Velocity At Outlet

$$c = \sqrt{\gamma . R . T}$$

Mach Number At Outlet

$$M = \frac{VEL}{c}$$

Total Enthalpy H At Outlet

$$H = \frac{\rho E + P}{\rho}$$

3.7.10 Boundary Condition Implementation - Walls.

At impermeable walls no mass transfer could occur therefore the value of the mass fluxes CMASSX and CMASSY could be set to zero at the walls as required with the values of the flow variables in the ghost cells at the wall simply extrapolated from the adjacent interior cell.

3.8 Solution Of The Acoustic Field.

If the acoustic propagation within the domain is considered to be unaffected by viscosity and the acoustic wave amplitudes small compared to the mean flow then the unsteady pressure field arising due to an applied acoustic perturbation can be described using the Euler equations. These can again be solved using the Jameson scheme in the same manner as that applied to the solution for the mean flow.

It can be seen therefore that computation of the acoustic field within the domain could be made via a two step method wherein in the first step the aerodynamic pseudo steady state solution is solved for using the time domain finite volume solution of the Euler equations. This would then be followed by a second step wherein a perturbation representing an acoustic disturbance is introduced into the flow and the unsteady pressure field again solved for using the finite volume scheme. Subtraction of the pseudo steady state pressure amplitudes from the unsteady pressure amplitudes arising from the introduction of the acoustic disturbance into the mean flow will then provide the pressure field due to the acoustic disturbance alone. Hence the propagation and interaction of the original acoustic source within the domain can be observed.

3.8.1 Description Of The Method.

The two step method for computing the acoustic field is described as follows.

In the first step a time domain solution to the non linear Euler equations is obtained using the Jameson finite volume scheme. Iterations are performed until convergence to a pseudo steady state is achieved.

In the second step the acoustic solution is obtained as follows.

Firstly, the static boundary condition at the inlet is modified by the addition of an unsteady perturbation representing an incoming acoustic wave. In the application considered in this study a sinusoidal disturbance simulating a selected amplitude and frequency component of the known acoustic power spectrum at the gas turbine bellmouth is introduced to the mean flow at the system inlet.

Secondly, to prevent spurious non physical numerical reflections from the domain boundaries from reflecting back into the computational domain and contaminating the acoustic solution, non reflecting boundary conditions are prescribed at the inlet and outlet boundaries. In this study Local One Dimensional Inviscid characteristic based non reflecting boundary conditions were applied as these were easy to implement and computationally efficient.

Thirdly, the unsteady Euler equations are then again solved in the time domain in the same manner as for the pseudo steady state solution, although the magnitude of the artificial viscosity coefficient may be reduced to a small value such as 0.1 percent. The pseudo steady state pressure amplitudes from the mean flow solution are then

subtracted from those obtained from the acoustic solution thereby giving a solution for the pressure field due to the applied acoustic perturbation only.

The time domain data for the acoustic field alone can then be postprocessed by Fast Fourier Transform (FFT) to provide the acoustic pressure amplitudes and frequency spectra at any location within the computational domain. Comparison of frequency spectra and wave amplitudes may then be undertaken to assess the systems acoustic characteristics. In addition animated movies of the acoustic propagation throughout the domain can be obtained by post processing in a commercial graphics plotting program such as Tecplot.

3.8.2 Requirements Of The Method

In order to undertake the solution for the acoustic field two new criteria must be defined, these being the specification of the acoustic perturbation at the inlet boundary and the prescription of the non reflecting boundary conditions.

Specification of inlet perturbation.

The acoustic power spectrum emanating from the gas turbine and entering the inlet boundary of the computational domain of the intake or exhaust system under consideration is very complex, featuring a large number of fundamental and harmonic components of compressor and turbine blade pass frequencies, mechanical sources arising from ancillaries such as lube oil pumps as well as aerodynamic noise associated with the turbine core and exhaust. It is common practice for the acoustic designer therefore to select a frequency band of interest and seek to achieve specific levels of attenuation in this band. In the example considered in this study the acoustic disturbance was considered to behave as a sinusoidal component superimposed upon the mean flow having a user defined frequency and amplitude. The incoming pressure wave amplitude at the inlet boundary could then be represented as follows.

$$p_{specified} = p_0 + Amplitude \times \sin(\omega t + \phi_p)$$

Where *Amplitude* is the amplitude of the applied perturbation (this being specified by the user) and the angular frequency $\omega=2.\pi.f$ where f is the frequency of the applied perturbation (this also being specified by the user). P_0 represents the stagnation pressure at the inlet boundary and ϕ_p represents phase angle (taken to be zero).

Prescription of the non reflecting boundary conditions.

These are described in Section 3.9.

3.9 Non Reflecting Boundary Conditions.

Introduction

In the numerical study the domain terminated at the outlet cowl of the bleed system where the static pressure was considered to be fixed at a value equal to the ambient atmospheric pressure. By doing so this effectively imposed a form of rigid wall condition at the outlet boundary with the result being that a pressure wave incident upon the outlet boundary would be reflected back into the interior of the domain. This was clearly evident in the animated contours of the pressure data and was contrary to the expected physical behaviour where the outgoing pressure wave would simply pass through the outlet boundary to the ambient atmosphere.

For the steady state case, where the pressure wave amplitudes due to flow velocity were an order of magnitude greater than the acoustic pressure due to reflection at the outlet boundary, this phenomena did not present a concern. However for a study of the acoustic wave behaviour within the bleed system such artificial reflections from the outlet and inlet boundaries could not be tolerated. Therefore some means of eliminating numerical reflection at the inlet and outlet boundaries had to be devised. To enable this non reflecting boundary conditions (hereafter referred to as NRBC's) had to be implemented at the inlet and outlet boundaries. Their development and application is described below.

3.9.1 Formulation Of The Non Reflecting Boundary Conditions.

Starting with the conservation form of the 2D Euler equations expressed in vector form as follows.

$$\frac{\partial}{\partial t}\begin{pmatrix}\rho\\ \rho u\\ \rho v\\ \rho E\end{pmatrix}+\frac{\partial}{\partial x}\begin{pmatrix}\rho u\\ \rho u^2+p\\ \rho uv\\ \rho uE+pu\end{pmatrix}+\frac{\partial}{\partial y}\begin{pmatrix}\rho v\\ \rho uv\\ \rho v^2+p\\ \rho vE+pv\end{pmatrix}=0$$

Transformation to the 1D characteristic variables yielded the following.

$$\begin{bmatrix}\partial C_1\\ \partial C_2\\ \partial C_4\\ \partial C_5\end{bmatrix}=\begin{bmatrix}-c^2 & 0 & 0 & 1\\ 0 & 0 & \rho c & 0\\ 0 & \rho c & 0 & 1\\ 0 & -\rho c & 0 & 1\end{bmatrix}\times\begin{bmatrix}\delta\rho\\ \delta u\\ \delta v\\ \delta p\end{bmatrix}$$

Transformation from the characteristic variables to obtain the perturbation variables yielded the following.

$$\begin{bmatrix} \partial\rho \\ \partial u \\ \partial v \\ \partial p \end{bmatrix} = \begin{bmatrix} -1/c^2 & 0 & 1/2c^2 & 1/2c^2 \\ 0 & 0 & 1/2\rho c & -1/2\rho c \\ 0 & 1/\rho c & 0 & 0 \\ 0 & 0 & 1/2 & 1/2 \end{bmatrix} \times \begin{bmatrix} \delta C_1 \\ \delta C_2 \\ \delta C_4 \\ \delta C_5 \end{bmatrix}$$

We could therefore write expressions for the characteristic variables as follows.

$$\delta C_1 = -c^2\delta\rho + \delta p$$

$$\delta C_2 = \rho c\delta v$$

$$\delta C_4 = \rho c\delta u + \delta p$$

$$\delta C_5 = -\rho c\delta u + \delta p$$

And hence we could also write expressions for the perturbation variables as follows.

$$\delta\rho = \frac{-1}{c^2}\delta C_1 + \frac{1}{2c^2}\delta C_4 + \frac{1}{2c^2}\delta C_5$$

$$\delta u = \frac{1}{2\rho c}\delta C_4 - \frac{1}{2\rho c}\delta C_5$$

$$\delta v = \frac{1}{\rho c}\delta C_2$$

$$\delta p = \frac{1}{2}\delta C_4 + \frac{1}{2}\delta C_5$$

3.9.2 Non Reflecting Boundary Conditions - Inlet Boundary.

Considering Figure 3.9.1 below.

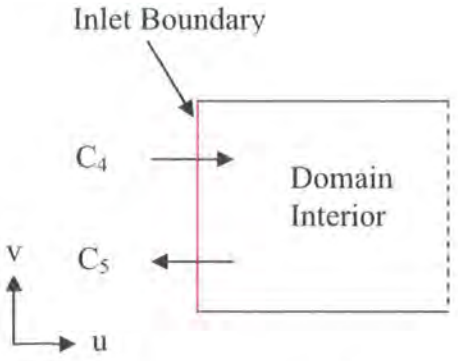

Figure 3.9.1

Considering the u velocity to be positive if it is entering the domain (right running) and negative if exiting the domain (left running), then from the previous definition of the characteristics it is seen that characteristics C1, C2 and C4 are right running and characteristic C5 is left running.

In addition we also know that for incoming (right running) characteristics variables must be specified, whereas for outgoing (left running) characteristics the variables must be extrapolated from the interior.

Therefore we can re write the definition of the characteristics as follows.

$$\delta C_1 = -c^2 \delta\rho + \delta p$$
i.e. $$\delta C_1 = -c^2 \left(\rho_{specified} - \rho_{old}\right) + \left(p_{specified} - p_{old}\right)$$

$$\delta C_2 = \rho c \delta v$$
i.e. $$\delta C_2 = \rho c \left(v_{specified} - v_{old}\right)$$

$$\delta C_4 = \rho c \delta u + \delta p$$
i.e. $$\delta C_4 = \rho c \left(u_{specified} - u_{old}\right) + \left(p_{specified} - p_{old}\right)$$

$$\delta C_5 = -\rho c \delta u + \delta p$$
i.e. $$\delta C_5 = -\rho c \left(u_{extrapolated} - u_{old}\right) + \left(p_{extrapolated} - p_{old}\right)$$

3.9.3 Non Reflecting Boundary Conditions - Outlet Boundary.

Considering Figure 3.9.2 below.

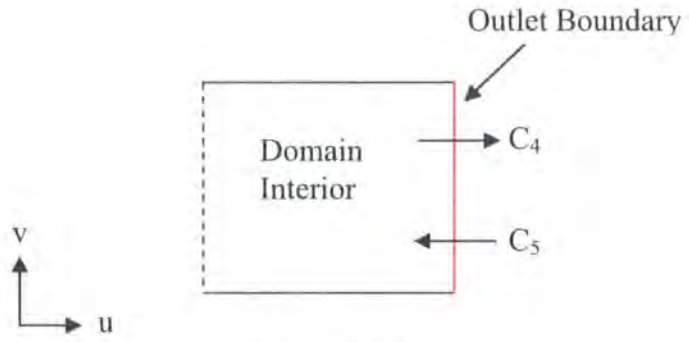

Figure 3.9.2

From the previous definition of the characteristics it is seen that at the outlet boundary the characteristics C1, C2 and C4 are right running and characteristic C5 is left running. In addition at the outlet boundary we also know that for outgoing (right running) characteristics variables must be extrapolated from the interior to the outlet boundary. Therefore we can re write the definition of the characteristics as follows.

$$\delta C_1 = -c^2 \delta\rho + \delta p$$
$$\text{i.e. } \delta C_1 = -c^2 \left(\rho_{extrapolated} - \rho_{old}\right) + \left(p_{extrapolated} - p_{old}\right)$$

$$\delta C_2 = \rho c \delta v$$
$$\text{i.e. } \delta C_2 = \rho c \left(v_{extrapolated} - v_{old}\right)$$

$$\delta C_4 = \rho c \delta u + \delta p$$
$$\text{i.e. } \delta C_4 = \rho c \left(u_{sextrapolated} - u_{old}\right) + \left(p_{extrapolated} - p_{old}\right)$$

$$\delta C_5 = -\rho c \delta u + \delta p$$
$$\text{i.e. } \delta C_5 = -\rho c \left(u_{extrapolated} - u_{old}\right) + \left(p_{extrapolated} - p_{old}\right)$$

However, in order to apply the non reflecting boundary condition at the inlet boundary the incoming velocity of the left running, or incoming characteristic C5 across the boundary must be set to zero, and by doing so characteristic C5 becomes

$$\delta C_5 = \delta p$$
$$\text{i.e. } \delta C_5 = \left(p_{extrapolated} - p_{old}\right)$$

3.9.4 Implementation Of The Non Reflecting Boundary Conditions.

Inlet Boundary.

At the inlet boundary the stagnation pressure P_0 and stagnation temperature T_0 were specified, therefore the stagnation density ρ_0 could be calculated. Also, knowing the static pressure at the inlet (this having being extrapolated from the interior of the domain), the inlet Mach number could be calculated. With the inlet Mach number now known, the inlet velocity magnitude could be calculated, and hence the values of the velocity components u_0 and v_0. The method for applying the non reflecting boundary condition at the inlet was then as follows.

First of all, the characteristics C1, C2, C4 and C5 were calculated as follows.

$$C1\_inlet = -c^2\left(\rho_{specified} - \rho_{old}\right) + \left(p_{specified} - p_{old}\right)$$
$$C2\_inlet = \rho c\left(v_{specified} - v_{old}\right)$$
$$C4\_inlet = \rho c\left(u_{specified} - u_{old}\right) + \left(p_{specified} - p_{old}\right)$$
$$C5\_inlet = -\rho c\left(u_{extrapolated} - u_{old}\right) + \left(p_{extrapolated} - p_{old}\right)$$

Where

$$\rho_{specified} = \rho_0 + Amplitude \times \sin\left(\omega t + \phi_\rho\right)$$
$$u_{specified} = u_0 + Amplitude \times \sin\left(\omega t + \phi_u\right)$$
$$v_{specified} = v_0 + Amplitude \times \sin\left(\omega t + \phi_v\right)$$
$$p_{specified} = p_0 + Amplitude \times \sin\left(\omega t + \phi_p\right)$$

Where *Amplitude* is the amplitude of the applied perturbation (this being specified by the user for the pressure only with the corresponding amplitude for the other flow variables being inferred from this) and the angular frequency $\omega=2.\pi.f$ where f is the frequency of the applied perturbation (this also being specified by the user). The phase angle ϕ_ρ was set to zero.

Having calculated the characteristic values, the change of flow variables were calculated as follows.

$$delta\_rho\_inlet = \frac{-1}{c^2} C1\_inlet + \frac{1}{2c^2} C4\_inlet + \frac{1}{2c^2} C5\_inlet$$

$$delta\_u\_inlet = \frac{1}{2\rho c} C4\_inlet - \frac{1}{2\rho c} C5\_inlet$$

$$delta\_v\_inlet = \frac{1}{\rho c} C2\_inlet$$

$$delta\_p\_inlet = \frac{1}{2} C4\_inlet + \frac{1}{2} C5\_inlet$$

Finally the values of the flow variables themselves at the inlet boundary were calculated as follows.

rho_inlet = delta_rho_inlet + rho_old
u_inlet = delta_u_inlet + u_old
v_inlet = delta_v_inlet + v_old
p_inlet = delta_p_inlet + p_old

Outlet Boundary.

At the outlet boundary the static pressure P_{exit} had been specified. The values of the density, u and v velocity components and the static pressure were extrapolated from the interior of the domain. The method for applying the non reflecting boundary condition at the inlet was then as follows.

First of all, the characteristics C1, C2, C4 and C5 were calculated as follows.

$$C1\_outlet = -c^2\left(\rho_{extrapolated} - \rho_{old}\right) + \left(p_{extrapolated} - p_{old}\right)$$
$$C2\_outlet = \rho c\left(v_{extrapolated} - v_{old}\right)$$
$$C4\_outlet = \rho c\left(u_{extrapolated} - u_{old}\right) + \left(p_{extrapolated} - p_{old}\right)$$
$$C5\_outlet = \left(p_{extrapolated} - p_{old}\right)$$

Having calculated the values of the characteristic variables, the values of the flow variables were calculated as follows, with the inlet characteristic quantities now being replaced by the outlet characteristic quantities.

$$delta\_rho\_outlet = \frac{-1}{c^2} C1\_outlet + \frac{1}{2c^2} C4\_outlet + \frac{1}{2c^2} C5\_outlet$$
$$delta\_u\_outlet = \frac{1}{2\rho c} C4\_outlet - \frac{1}{2\rho c} C5\_outlet$$
$$delta\_v\_outlet = \frac{1}{\rho c} C2\_outlet$$
$$delta\_p\_outlet = \frac{1}{2} C4\_outlet + \frac{1}{2} C5\_outlet$$

Finally the values of the flow variables themselves at the outlet boundary are calculated as follows.

rho_outlet = delta_rho_outlet + rho_old
u_ outlet = delta_u_outlet + u_old
v_ outlet = delta_v_outlet + v_old
p_ outlet = delta_p_outlet + p_old

4.0 Verification And Validation

4.1 1D Euler Solution Of Transonic Nozzle Flow.

The one dimensional flow characteristics through a convergent divergent nozzle were studied and compared to values obtained from an analytical solution. The nozzle shape was defined by the curves $y=0.2x^2-0.24x+0.222$ (upper bound) and $y=-0.2x^2+0.24x-0.022$ (lower bound). The pressure ratio across the nozzle was defined to be equal to 0.80, chosen so as to form a normal shock in the divergent nozzle section.

The inlet conditions were defined as a stagnation pressure of 101330 Pa and stagnation temperature of 300 K, the outlet condition was prescribed as a static pressure of 81064 Pa.

The domain consisted of 1000 cells with the grid spacing specified to be 0.001 metre. The timestep was specified to be 5×10^{-6} seconds to maintain a Courant Number of 0.90 with the artificial viscosity damping coefficient set to 0.005. The solution was performed for 1×10^6 timesteps and convergence considered to have been reached when the residual of velocity U reached 1×10^{-6}.Total solution time was approximately 7 minutes on a 3 GHz Pentium IV pc with 1GB RAM.

Numerical values of the static pressure, Mach number and static temperature were evaluated along the nozzle horizontal centreline, the Mach number data are shown below in Figure 4.1.1. The red line indicates the Mach number, the grey line indicates the nozzle shape and area.

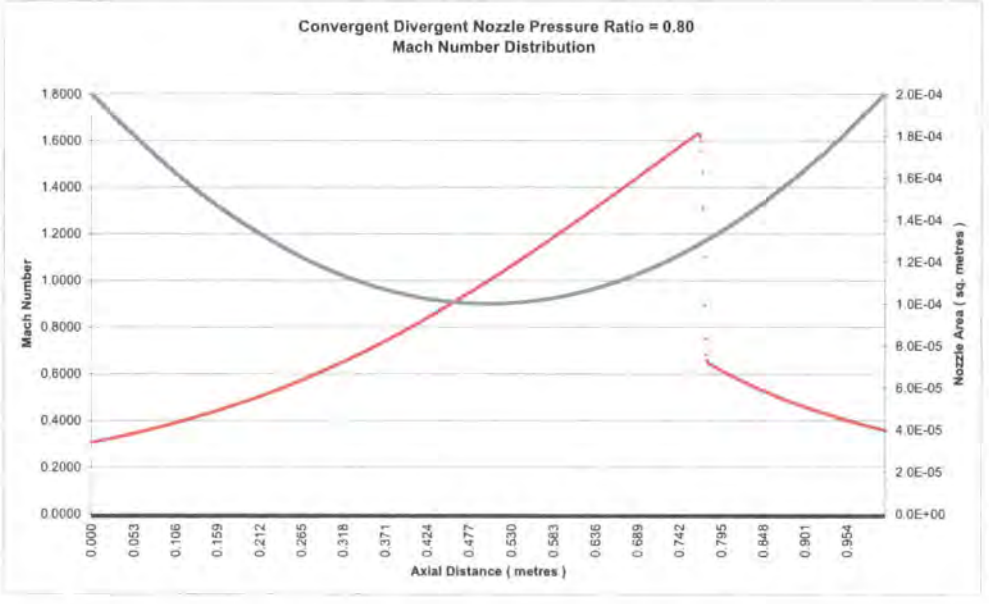

Figure 4.1.1 1D Euler Code Mach Number along nozzle axis.

Comparison With Analytical Solution

The mass flow through the nozzle domain was known to be constant, i.e. $P_{01}.A_1 = P_{exit}.A_{exit}$

The pressure ratio across the nozzle, P_{exit} / P_0 was known to be equal to 0.80, and the area ratio of the exit to the throat, A_{exit} / A_t was known to be 2.0.

i.e. $\frac{P_{exit}}{P_0} = 0.80$ and $\frac{A_{exit}}{A_t} = 2.0$, Therefore $\frac{P_{exit}.A_{exit}}{P_0.A_t} = 1.60$

Also

$$\frac{P_{exit}}{P_0} = \left(1 + \frac{\gamma - 1}{2}.M_{exit}^{\ 2}\right)^{\frac{-\gamma}{\gamma-1}} \quad \text{and} \quad \frac{A_{exit}}{A^*} = \frac{1}{M_{exit}}\left[\frac{2}{\gamma+1}\left(1 + \frac{\gamma-1}{2}.M_{exit}^{\ 2}\right)\right]^{\frac{\gamma+1}{2.(\gamma-1)}}$$

Therefore we can write

$$\left(1 + \frac{\gamma - 1}{2}.M_{exit}^{\ 2}\right)^{\frac{-\gamma}{\gamma-1}} \times \frac{1}{M_{exit}}\left[\frac{2}{\gamma+1}\left(1 + \frac{\gamma-1}{2}.M_{exit}^{\ 2}\right)\right]^{\frac{\gamma+1}{2.(\gamma-1)}} = 1.60$$

Solving by trial and error the Mach number at the nozzle exit was found to be equal to M_{exit} = 0.36.

Now, knowing the exit Mach number, it was possible to calculate the stagnation pressure ratio across the nozzle required to achieve this, i.e.

$$\frac{P_{exit}}{P_0} = \left(1 + \frac{\gamma - 1}{2}.M_{exit}^{\ 2}\right)^{\frac{-\gamma}{\gamma-1}}$$

Giving a value for the pressure ratio required for an exit Mach number of 0.36 to be equal to P_{exit}/P_0= 0.9165.

Since the actual pressure ratio across the nozzle was equal to 0.80, some mechanism must account for the difference between the two values of pressure ratio - the only mechanism available for this being the normal shock.

The pressure ratio across the normal shock could be expressed as

$$\frac{P_{02}}{P_{01}} = \frac{0.80}{0.9165} = \left[\frac{(\gamma+1).M_1^{\ 2}}{(\gamma-1).M_1^{\ 2}+2}\right]^{\frac{\gamma}{\gamma-1}} \times \left[\frac{\gamma+1}{2.\gamma.M_1^{\ 2}-(\gamma-1)}\right]^{\frac{1}{\gamma-1}}$$

Solving by trial and error the Mach number upstream of the shock was calculated to be M = 1.66.

It was now possible to apply the area-Mach number relation to calculate the position within the nozzle at which the Mach number was equal to 1.66 as follows.

$$\frac{A}{A_{throat}} = \frac{1}{M}\left[\frac{2}{\gamma+1}\left(1+\frac{\gamma-1}{2}.M^2\right)\right]^{\frac{\gamma+1}{2.(\gamma-1)}}$$

Substituting M = 1.66 it was calculated that the shock should form at a location in the nozzle where the area ratio was equal to 1.30.

Finally, it was possible to calculate the Mach number immediately downstream of the shock as follows.

$$M_2 = \sqrt{\frac{1+\frac{\gamma-1}{2}.M_1^{\,2}}{\gamma.M_1^{\,2}-\frac{\gamma-1}{2}}} = 0.65$$

Discussion Of Results

It was possible to compare the calculated values of Mach number at the nozzle inlet, exit and across the normal shock with those values provided by the graphical plot of Mach number shown in Figure 4.1.1. These are summarised below.

	1D Euler code result	Analytical solution
Mach number upstream of shock	1.63	1.66
Mach number downstream of shock	0.64	0.65
Mach number at nozzle exit	0.37	0.36
Axial location of shock	$A_{shock}/A_{throat} = 1.3$	$A_{shock}/A_{throat} = 1.3$

Conclusions

The quasi 1D solution of the Euler equations undertaken using the finite volume, time marching space centred method with artificial viscosity described previously and implemented in the code "Euler1D" was found to provide an accurate solution to the 1D nozzle problem with the solution data being in agreement with the analytical solution.

4.2 2D Euler Solution Of Transonic Nozzle Flow

The flow characteristics through a two dimensional convergent divergent nozzle having the same geometry as that considered for the 1D nozzle study were considered. The nozzle geometry was initially left unchanged from that adopted for the 1D study, however initial solution results indicated divergence of the solution at the inlet boundary. This was attributed to the sudden change in geometry at the inlet resulting in the static pressure exceeding the stagnation pressure and as a result a failure to compute the inlet Mach number. Therefore a short parallel section was added to the nozzle inlet to allow the solution to start without compromising the flow characteristics within the nozzle.

The inlet conditions were defined as a stagnation pressure of 101330 Pa and stagnation temperature of 300 K, the outlet condition was prescribed as a static pressure of 81064 Pa.

The timestep was chosen so as to provide a Courant number of 0.50 and the coefficient of artificial viscosity first set to 0.005 and then 0.02 to explore it's effect upon the normal shock characteristics. The solution was run for a total of 50,000 timesteps.

Numerical values of the static pressure, Mach number and static temperature were evaluated. A contour plot of the Mach number is shown as Figure 4.2.1.

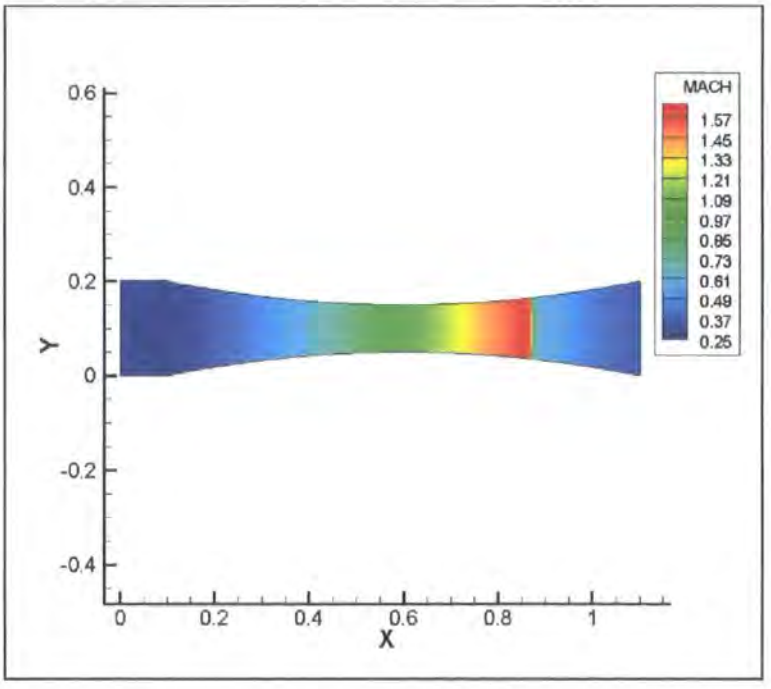

Figure 4.2.1 Mach number contours.

A graphical plot of Mach number evaluated along the nozzle centerline at two values of the artificial viscosity coefficient is shown below in Figure 4.2.2.

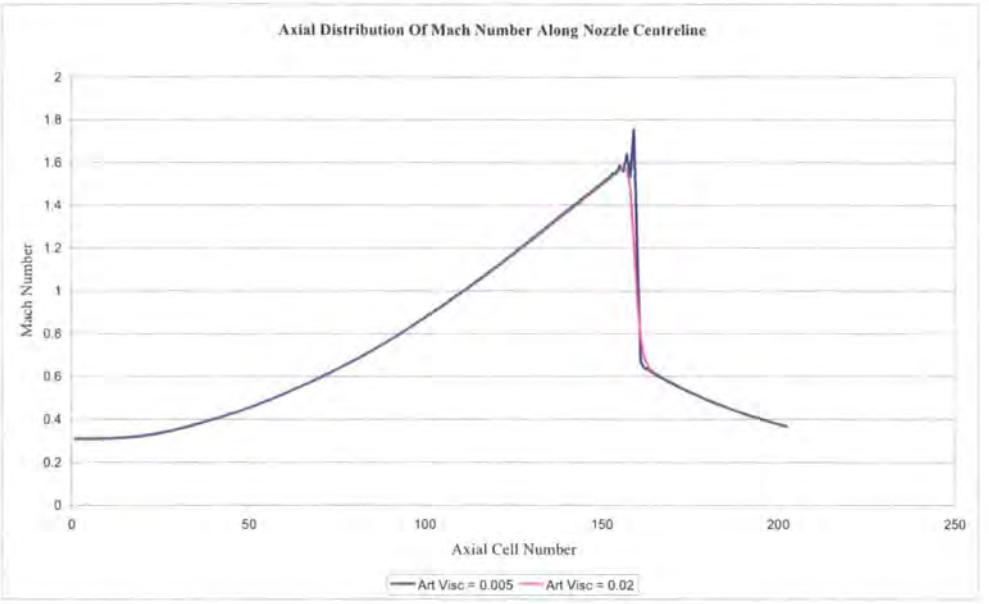

Figure 4.2.2 Axial Mach number distribution.

The values of Mach number upstream and downstream of the shock and at the nozzle outlet were compared against the analytical solution. These are summarized below.

	2D Euler code result	Analytical solution
Pre shock Mach number 0.5 % damping	1.77	1.66
Pre shock Mach number 2.0 % damping	1.58	1.66
Post shock Mach number 0.5 % damping	0.64	0.65
Post shock Mach number 2.0 % damping	0.62	0.65
Mach number at nozzle exit 0.5 % damping	0.37	0.36
Mach number at nozzle exit 0.5 % damping	0.37	0.36
Axial location of shock	$A_{shock}/A_{throat} = 1.3$	$A_{shock}/A_{throat}=1.3$

From an examination of Figure 4.2.2 it was evident that a low value of damping resulted in a better resolved shock wave, however the maximum Mach number was slightly overpredicted at the leading edge. An increase of the damping to 2 % attenuated the ringing oscillations although at the expense of a slight under prediction of the maximum Mach number and smearing of the shock wave over a greater number of grid cells.

In conclusion the numerical scheme and program formulated for the study of the two dimensional Euler equations were found to offer an accurate and stable solution to the two dimensional nozzle problem that was in agreement with the findings of the earlier one dimensional study and the analytical solution.

4.3 Multiblock 2D Euler Solution Of Supersonic Flow Over An Incline Wedge.

The flow characteristics of a Mach 2.0 flow passing over a 10 degree wedge were examined. This was chosen as the flow characteristics could be validated against an analytical solution, thereby providing further validation of the Euler scheme. The computational grid for the problem is shown below in Figure 4.3.1. Details of the interface method adopted in the multiblock implementation are given in Appendix 3.

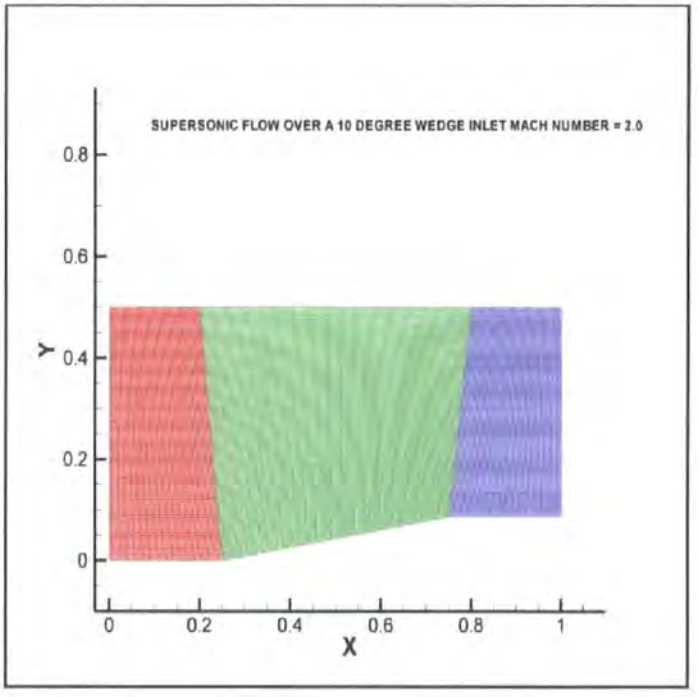

Figure 4.3.1

At the inlet boundary the stagnation pressure P0, the stagnation temperature T0 and the static pressure P were specified. Isentropic flow relations were used to calculate the stagnation conditions at M=2.0 as follows.

$$\frac{P_{static}}{P_0} = \left(1 + \frac{\gamma - 1}{2}.M^2\right)^{\frac{-\gamma}{\gamma - 1}}$$

Substituting M = 2.0 and P_{static} = 101325.0, P_0 was calculated to be 792812.0 Pa. The stagnation temperature T0 was evaluated from the isentropic relation.

$$\frac{T}{T_0} = \left(1 + \frac{\gamma - 1}{2}.M^2\right)^{-1}$$

Substituting M = 2.0 and T = 300 K, T_0 was calculated to be 540 K.

At the outlet boundary the values of the conservative variables RO, ROU,ROV and ROE were extrapolated from the interior of the domain.

The timestep was chosen so as to provide a Courant number of 0.50 and the coefficient of artificial viscosity set to 0.005. The solver was run for a total of 50,000 timesteps.
A contour plot of Mach number for a flow over a 10 degree wedge at an inlet Mach number of 2.0 obtained using the Euler2D code is shown below in Figure 4.3.2.

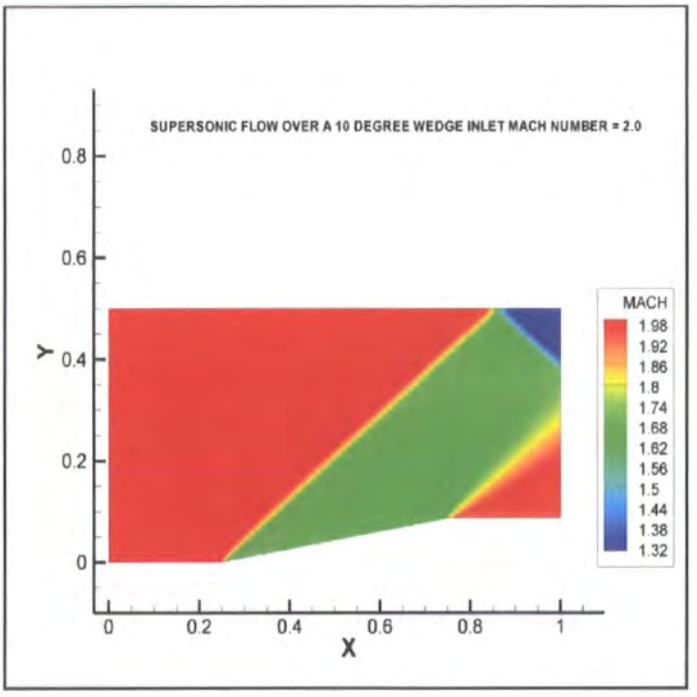

Figure 4.3.2

A line contour plot of static pressure for a flow over a 10 degree wedge at an inlet Mach number of 2.0 obtained using the Euler2D code is shown below in Figure 4.3.3.

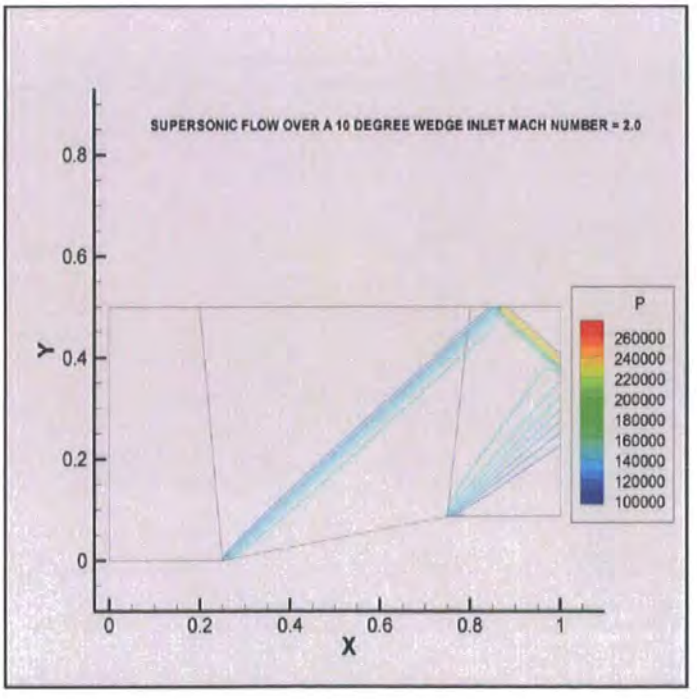

Figure 4.3.3

Comparison With Analytical Solution

The relations for the change of flow characteristics across an oblique shock were taken from NACA report 1135 [21] and were used to calculate the oblique shock angle and the increase of static pressure, static temperature and density across the shock formed as a result of a supersonic flow passing over the wedge profile shown below in Figure 4.3.4.

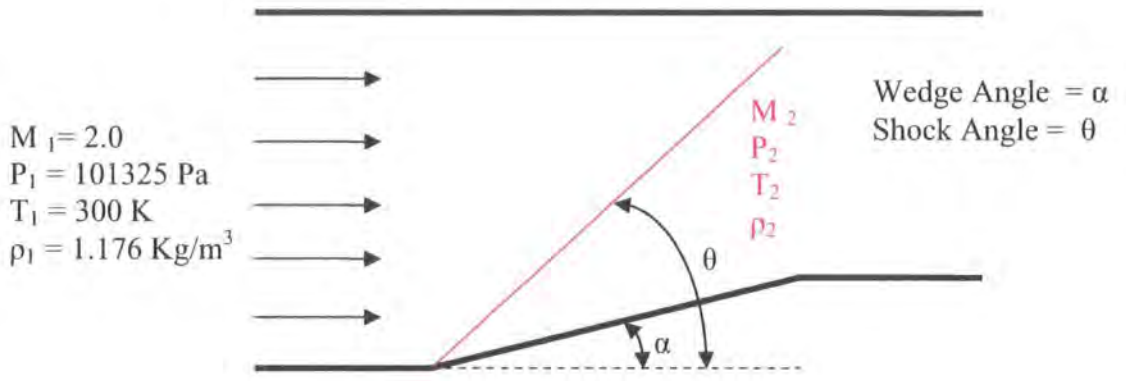

Figure 4.3.4

The shock angle θ was calculated from the following relation.

$$Cot(\alpha) = Tan(\theta)\left[\frac{(\gamma+1).M_1^2}{2.(M_1^2.\sin^2\theta - 1)} - 1\right]$$

Inserting values for the freestream Mach number $M_1 = 2.0$ and the wedge half angle $\alpha = 10^\circ$ the value of the shock angle θ was calculated implicitly to be equal to 39.3°.

The value of the post shock Mach number was calculated using the following relation.

$$M_2^2.\sin^2(\theta - \alpha) = \frac{(\gamma-1).M_1^2.\sin^2\theta + 2}{2.\gamma.M_1^2.\sin^2\theta - (\gamma-1)}$$

Inserting values for the freestream Mach number M_1 and the shock angle θ, the Mach number downstream of the oblique shock was calculated to be equal to 1.64.

The value of the ratio of the static pressure downstream of the oblique shock to the stagnation pressure P_0 was calculated using the following relation.

$$\frac{P_2}{P_0} = \frac{2.\gamma.M_1^2.\sin^2\theta - (\gamma-1)}{\gamma+1}$$

Inserting values for the freestream Mach number M_1 and the shock angle θ, the static pressure ratio across the shock was calculated to be 1.70. Therefore the static pressure downstream of the shock was calculated as being 101325.0 x 1.70 = 172252.5 Pa.

The value of the ratio of the static temperature downstream of the oblique shock to the stagnation temperature T_0 was calculated using the following relation.

$$\frac{T_2}{T_0} = \frac{\left[2.\gamma.M_1^2.\sin^2\theta - (\gamma-1)\right]\left[(\gamma-1).M_1^2.\sin^2\theta + 2\right]}{(\gamma+1)^2.M_1^2.\sin^2\theta}$$

Inserting values for the freestream Mach number M_1 and the shock angle θ, the static temperature ratio across the shock was calculated to be 1.17. Therefore the static temperature downstream of the shock was calculated as being 300.0 x 1.17 = 351 K.

The value of the ratio of density downstream of the oblique shock to the stagnation density ρ_0 was calculated using the following relation.

$$\frac{\rho_2}{\rho_0} = \frac{(\gamma+1).M_1^2.\sin^2\theta}{(\gamma-1).M_1^2.\sin^2\theta + 2}$$

Inserting values for the freestream Mach number M_1 and the shock angle θ, the density ratio across the shock was calculated to be 1.458. Therefore the density downstream of the shock was calculated as being 1.176 x 1.458 = 1.71 Kg/m^3

The values of the flow variables across the compression shock derived from the solution data are shown below in Figure 4.3.5 compared against their analytical values.

	Upstream of Shock	Downstream of Shock	
		Euler2D	Analytical
Mach Number	2.00	1.64	1.64
Static Pressure	101325.0	171405.0	172252.0
Static Temperature	300.0	350.10	351.00
Density	1.176	1.710	1.710

Figure 4.3.5

In conclusion the Euler2D code was found to accurately predict the formation of an attached oblique shock wave over a 10 degree wedge body. The values of the shock wave angle, Mach number reduction, static pressure rise, static temperature rise and increase of density predicted by the code were all found to be in close agreement with their theoretical values.

4.4 Acoustic Propagation In A 1D Duct

In order to choose an adequate grid resolution (number of cells per wavelength) for the acoustic studies and to investigate the behaviour of the non reflecting boundary conditions, a simple test problem was devised whereby a oscillatory boundary condition was applied to a rectangular duct of constant cross section with non reflecting boundary conditions being specified at the inlet and outlet of the domain.

The domain was defined as a rectangular geometry 2 metres in length and 0.2 metres in height to which a quadrilateral mapped grid was applied having 200 cells in the horizontal direction and 20 cells in the vertical direction.

Conventional reflecting boundary conditions for a subsonic flow were applied in order to achieve a steady state solution, and once steady state had been achieved the non reflecting boundary conditions were applied.

For the solution of the mean flow the boundary conditions prescribed at the inlet boundary were a stagnation pressure of 101325 Pa and a stagnation temperature of 300 K were applied. At the outlet boundary a static pressure of 90000 Pa was applied.

For the solution of the acoustic field a characteristic based non reflecting boundary condition was applied at the inlet with a sinusoidal oscillating wave of amplitude 0.07 percent and frequency of 200 Hz also applied. The frequency was later increased to 400, 800 and 1600 Hz to explore the effect of grid resolution and frequency upon the attenuation of the pressure waveform along the domain due to numerical effects.

At the outlet a characteristic based non reflecting boundary condition was applied with the exit pressure downstream remaining at the specified value of 90000 Pa.

The timestep was chosen so as to provide a Courant number of 0.90 and the coefficient of artificial viscosity set to 0.001, corresponding to 0.1 percent. The solver was run for a total of 10,000 timesteps for each case study.

The numerical values of the static pressure at the inlet and outlet were written to an output file and then summated to give an average value for the static pressure at the inlet and outlet boundary at frequencies of 200, 400, 800 and 1600 Hz and the attenuation calculated as the ratio of the peak amplitude of the pressure waveform at the inlet and outlet boundaries. These are summarized below in Figure 4.4.1

Frequency	200	400	800	1600
Cells/wavelength	170	85	42	21
Static pressure Inlet	90066	90066	90066	90066
Static pressure outlet	90064	90064	90063	90055
Attenuation	3 %	3 %	4 %	18 %

Figure 4.4.1

In addition graphical animations of the contours of static pressure were produced which permitted viewing of the propagation of the unsteady pressure amplitudes within the test duct domain. As an example a frame from the animation file for the case of an inlet perturbation frequency of 1.6 KHz is shown below as Figure 4.4.2.

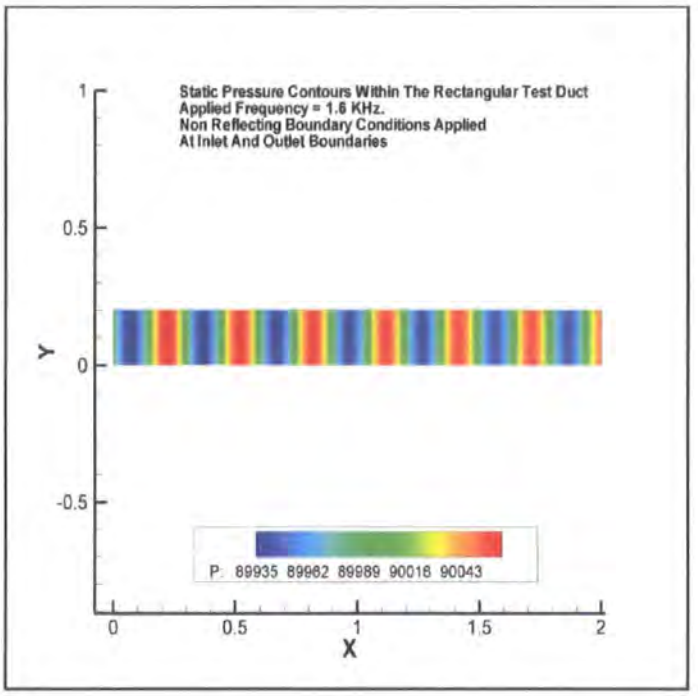

Figure 4.4.2

Inspection of Figure 4.4.2 revealed the distribution of the maxima and minima of static pressure to be periodic at a frequency of 1.6 KHz along the entire length of the domain. In addition no generation or reflection of spurious waves were observed from the outlet boundary. This indicated that no pressure wave reflection from the downstream boundary was occurring and therefore the non reflecting boundary conditions were performing as intended.

In addition it was found from Figure 4.4.1 that a grid resolution of 50 cells per wavelength should provide an acceptable compromise between minimizing the attenuation due to numerical damping and the computational requirements imposed by use of such a fine grid.

Therefore for all subsequent acoustic studies the grid resolution was specified to be 50 cells/wavelength.

5.0 Industrial Case Studies

5.1 Case Study 1
Flow Characteristics Of An Industrial Gas Turbine Combustion Intake System.

The flow characteristics of an industrial gas turbine combustion intake system were investigated using the Euler scheme. The intake system comprised of a series of intake ducts and transitions, a baffle type intake silencer and a radial inlet scroll. The combustion air mass flow was approximately 165 Kg/s at 27 Degrees Celsius.

5.1.1 Geometry and Computational Grid Definitions.

The combustion intake geometry was constructed as 14 discrete blocks in the grid program. For initial studies the presence of the intake silencer was neglected. The block layout is shown below as Figure 5.1.1.

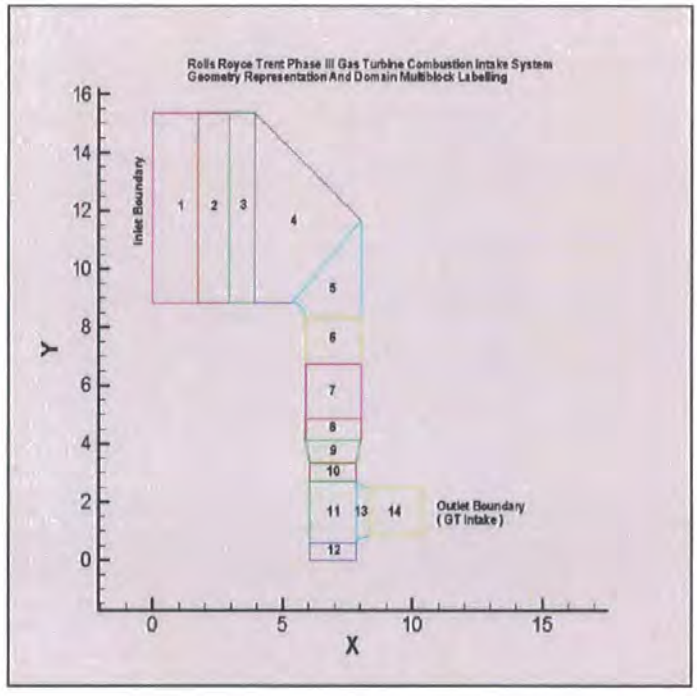

Figure 5.1.1

A mapped quadrilateral grid was created for each of the defined blocks within the domain using the method of transfinite interpolation. The domain consisted of 18564 cells in total.

5.1.2 Boundary Conditions.

At the subsonic inlet two physical boundary conditions were prescribed (a stagnation pressure of 101325 Pa and stagnation temperature of 300 K) and one numerical boundary condition (the static pressure) extrapolated from the interior to the inlet boundary.

At the subsonic outlet one physical boundary condition (the static pressure) was prescribed and two numerical boundary conditions (conservative variables ROU and ROE) extrapolated from the interior of the domain to the outlet boundary. The static pressure at the outlet boundary was specified to be 80,000 Pa, selected to give a mass flowrate at the outlet boundary of 165 Kg/s as required by the design specification.

At a wall boundary the component of velocity normal to the wall was set to zero. Since the walls were impermeable the values of CMASSY and CMASSX were set to zero at the upper/lower and left/right wall boundaries respectively, the flow variables at the walls then being extrapolated from the adjacent interior cells. Coupling of adjacent blocks was accomplished by the creation of interface blocks in the solver to exchange flow variables across cell boundaries between blocks 1&2, 2&3, 3&4, 4&5, 5&6, 6&7, 7&8, 8&9, 9&10, 10&11, 11&12, 11&13, and 13&14.

The timestep was chosen so as to provide a Courant number of 0.50 and the coefficient of artificial viscosity initially set to 0.02 (2%), later being reduced to 0.005 (0.5%). The solution proceeded for a total of 2.5×10^6 timesteps until the mass flow at the inlet and outlet boundaries were found to converge to within 1 percent.

5.1.3 Presentation Of Results.

A streamline and filled contour plot of the velocity magnitude data is shown below as Figure 5.1.2.

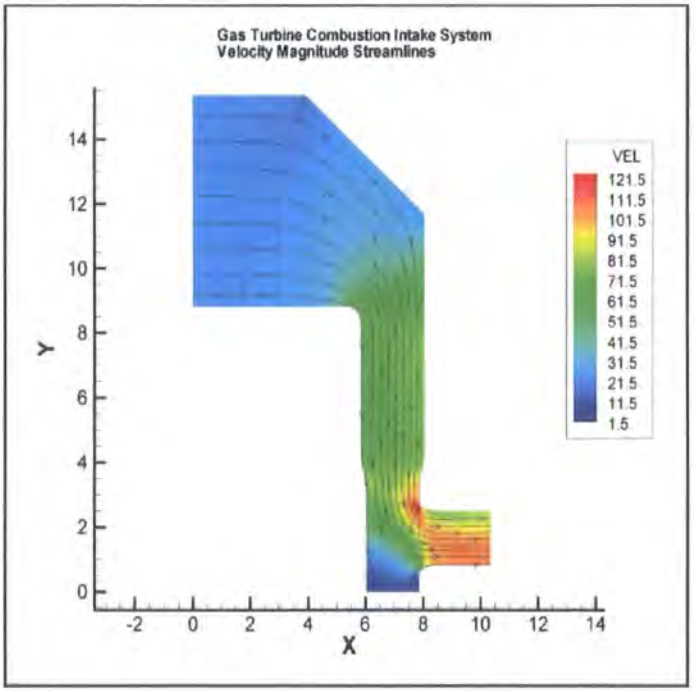

Figure 5.1.2

Convergence of the solution to steady state was assessed by monitoring the net mass flow and the residuals of u and v velocity. The solution required in excess of 2×10^6 timesteps to fully converge, however the residuals of u and v velocity had reduced to

the desired level of $1x10^{-6}$ after approximately 500,000 timesteps at which the net mass flow had become constant at approximately 20 Kg/second. It was suspected that mass flow convergence had not been achieved due to the value of the artificial viscosity damping coefficient of 2 percent. Therefore the value of the damping term was reduced to 0.5 percent and the solution continued until mass flow convergence was achieved.

Referring to Figure 5.1.2 it was found that a maximum flow velocity of 121 m/s was found at the interface between the intake scroll and the radiused entry to the gas turbine compressor bellmouth. Evidence of apparent flow separation can be seen here along the upper wall immediately downstream of the bellmouth, although this was considered likely to be both a true physical effect and the result of adopting an inviscid solution. In addition there existed a region of low flow velocity in the floor region of the intake scroll, however this was not unexpected due to the geometry at this location. Of more importance however were the low values of Mach number within the domain, particularly within the filter house and the floor region of the intake scroll where the Mach numbers were found to be approximately 0.08 and 0.04 respectively. This was of concern since the inviscid solution required significant changes of density to ensure rapid convergence. It was suspected that the low Mach numbers at these locations were responsible for the convergence difficulties and so in order to confirm this the contours of total enthalpy within the domain were examined. At steady state the value of the total enthalpy should be constant, however whilst this was found to be true within the bulk of the domain a change of total enthalpy was noted at the floor region of the intake scroll corresponding to the location of the lowest values of Mach number. This suggested that low values of the Mach number at the floor of the intake scroll could in part be responsible for the slow convergence of the solution.

The minimum values of the Mach number within the domain were a concern, since it was preferred to maintain the Mach number above a minimum value of 0.10 to ensure rapid convergence of the solution. It was apparent that in order to increase the Mach number at these locations the mass flow for the system would have to be increased significantly. An attempt to restart the solution using a higher mass flow was undertaken, however it was found that satisfactory convergence could only be achieved at a mass flow of over 300 Kg/s. This was considered unrepresentative of the true system, in addition the resulting higher flow velocities at the compressor bellmouth required a reduction of grid size and timestep to ensure solution stability.

For these reasons it was elected not to pursue the study of this particular intake system further and the study was terminated. Furthermore it was elected not to add the geometry of the intake silencer or porous media representation of the intake filtration as had been initially intended. An alternative system was sought which offered a lower internal volume and hence ought to offer higher velocity magnitudes more suited to the density based Euler scheme. This was found in the form of the Gas Turbine Compressor Emergency Bleed System studied hereafter.

5.2 Case Study 2
Flow Characteristics Of An Industrial Gas Turbine Compressor Emergency Bleed System.

The flow characteristics of a gas turbine compressor bleed system were investigated using the Euler scheme. This was chosen as the higher flow velocities encountered in the bleed system would be more suited to the density based Euler scheme and would offer improved solution convergence. The compressor bleed system comprised of a series of rectangular ducts and transitions together with a baffle type exhaust silencer. The system was designed to retard and acoustically attenuate the air released under pressure from the compressor stages of the gas turbine in the event of an emergency shutdown. The system was designed to accommodate a nominal mass flowrate of 54 Kg/s at a temperature of 104 degrees Celsius.

5.2.1 Geometry and Computational Grid Definitions.

The compressor bleed system geometry was constructed as 23 discrete blocks in the grid program. The block layout is shown below as Figure 5.2.1.

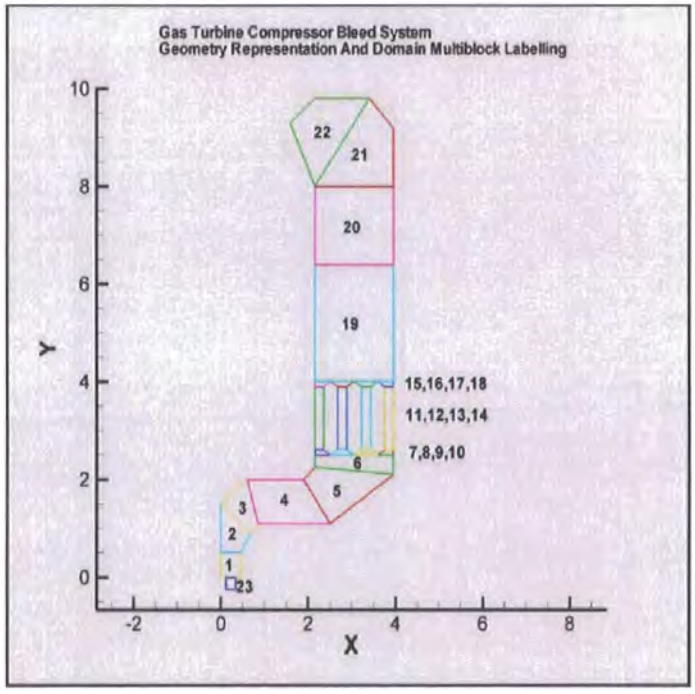

Figure 5.2.1

A mapped quadrilateral grid was constructed for each of the 23 defined blocks within the domain using the method of transfinite interpolation. The domain consisted of 15743 cells in total.

5.2.2 Boundary Conditions.

The design specification stated that the system mass flow was approximately 54 Kg/second at a temperature of 104 Degrees Celsius. It was known from discussions with the gas turbine manufacturer that the conditions within the three compressor stages were variable with the pressure within the high pressure compressor stage being up to 38 atmospheres. In addition the exact geometry of the discharge port from the compressor stages was not known, therefore a detailed representation of these could not be made for this study. As a compromise the dimensions of the inlet boundary were set to equal those of the bleed system to compressor stage interface flange which were known and the stagnation pressure at the inlet boundary adjusted to give the desired mass flow of 54 Kg/second. It was found that this was achieved at a value for the stagnation pressure of 130,000 Pa.

At the subsonic inlet two physical boundary conditions were prescribed (a stagnation pressure of 130000 Pa and stagnation temperature of 377 K) and one numerical boundary condition (the static pressure) extrapolated from the interior to the inlet boundary.

At the subsonic outlet one physical boundary condition (the static pressure) was prescribed and two numerical boundary conditions (conservative variables ROU and ROE) extrapolated from the interior of the domain to the outlet boundary. The static pressure at the outlet boundary was specified to be equal to atmospheric (101325 Pa).

At a wall boundary the component of velocity normal to the wall was set to zero. Since the walls were impermeable the values of CMASSY and CMASSX were set to zero at the upper/lower and left/right wall boundaries respectively, the flow variables at the walls then being extrapolated from the adjacent interior cells. Coupling of adjacent blocks was accomplished by definition of interface blocks in the solver at the boundaries between the following block assemblies

23 & 1 (Inlet interface to bleed system)
1&2, 2&3, 3&4, 4&5, 5&6 (Diverging transition and offset elbow transition)
6&7, 6&8, 6&9, 6&10 (Inlet of silencer)
10&11, 7&11, 8&12, 9&13, 10 &14, 11&15,12&16,13&17,14&18 (Bleed silencer pods)
15&19,16&19,17&19,18&19 (Outlet of silencer)
19&20,20&21 and 21&22 (Vertical duct, elbow transition and outlet cowl)

The timestep was chosen so as to provide a Courant number of 0.50 and the coefficient of artificial viscosity initially set to 0.01 (1%). The solution proceeded for a total of 300,000 timesteps until the mass flow at the inlet and outlet boundaries were found to converge to within 1 percent.

5.2.3 Presentation Of Results.

A streamline and filled contour plot of the velocity magnitude is shown below as Figure 5.2.2.

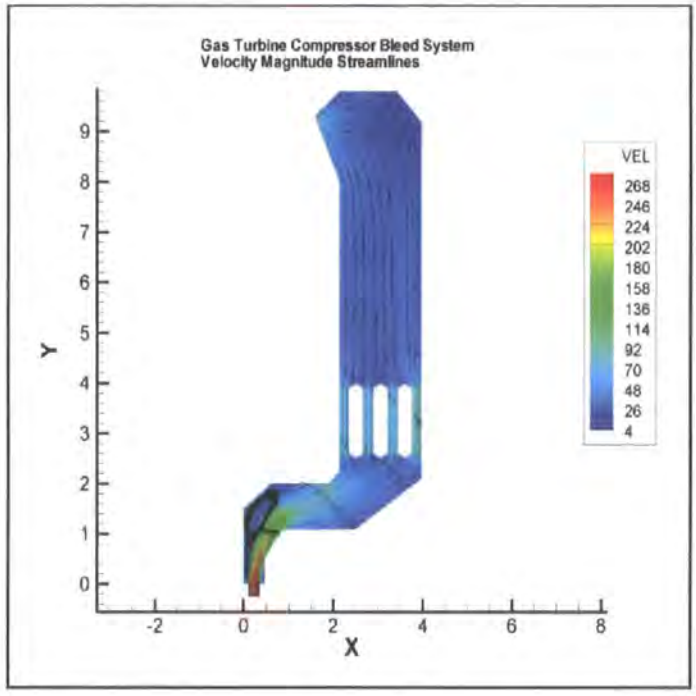

Figure 5.2.2

Convergence of the solution to steady state was assessed by monitoring the net mass flow and the residuals of u and v velocity. It was found that the net mass flow converged to within 1 percent and the residuals of u and v velocity decreased to the required value of 1×10^{-6} after approximately 200,000 timesteps.

Referring to Figure 5.2.2 the maximum value of the velocity magnitude was found to be approximately 260 m/s (corresponding to a Mach number of 0.73) occurring at the inlet boundary. Due to the geometry of the offset transition the flow was caused to turn through a right angle and as a result appeared to separate from the left wall forming a recirculation zone along the left wall which can be clearly seen in the velocity streamlines. It is noted however that an inviscid solution cannot technically produce viscosity dependent phenomena such as flow separation, it is suggested therefore that the presence of singularities in the domain caused by the creation of sharp corners at duct interfaces together with the addition of artificial viscosity in the solution could result in the formation of viscosity dependant phenomena such as the flow separation observed in the contour data.

The velocity distribution through the silencer pod flow apertures was also examined. Ideally the flow velocity through the silencer flow passages would be found to be uniform and equal to approximately 34 m/s. Examination of Figure 5.2.2 indicated the velocity magnitudes within the flow passages to be equal to approximately 67 m/s in the flowgaps adjacent to the left wall and between the central silencer splitter

pods but approximately 80 m/s within the flowgap adjacent to the right wall. However, whilst these magnitudes appear high it must be remembered that the 2D study here effectively assumed a unit silencer depth of 1 metre, whereas in fact the actual silencer internal depth was 2048 mm. Correcting for this the silencer flow gap velocity magnitudes became approximately 32.7 and 39 m/s. From the design specification for the mass flow and flowgap geometry the design spatial velocity through the silencer, assuming uniform flow was calculated to be 34 m/s. It can be seen therefore that in general terms the flow distribution through the silencer could be considered to be quite uniform except at the right wall where the presence of the solid boundary causes an increase in y momentum along the wall and a consequent increase in flow velocity through the flowgap between the right most splitter pod and the right hand wall boundary.

An examination of the Mach number contours indicated that despite a lower internal volume within the compressor emergency bleed system, low Mach numbers persisted within the domain particularly within the offset transition along the left wall. However despite this the required convergence criteria were met within 200,000 timesteps.

Although it was noted that the higher flow velocities in the numerical solution (by an approximate factor of 2) caused by the assumption of unit silencer depth would affect the acoustic solution, the acoustic wave speed (estimated in Case Study 3 to be approximately 389 m/s) was an order of magnitude greater than the mean flow velocity. Furthermore since the objective of the study was investigate the propagation of an applied acoustic disturbance onto the mean flow and not to directly predict flow generated noise it was considered that the higher flow velocities resulting from the use of a unit silencer depth in the numerical solution would not significantly affect the acoustic solution.

It was therefore decided that further study of the GT compressor bleed system to investigate it's acoustic characteristics could be undertaken.

5.3 Case Study 3
Acoustic Characteristics Of An Industrial Gas Turbine Compressor Emergency Bleed System.

The silencer configuration in the compressor bleed system was designed to offer an attenuation of approximately 3:1 at a frequency of 400 Hz and an attenuation ratio of 16:1 at a frequency of 800 Hz with maximum attenuation occurring at a frequency of approximately 2.5 KHz. However an acoustic solution at 2.5 KHz would require such a highly refined grid and small value of the timestep as to be impractical. It was therefore elected to conduct the acoustic studies at frequencies of 400 and 800 Hz. To obtain the acoustic solution a pseudo steady state solution was first obtained to provide a baseline mean flow solution. Non reflecting boundary conditions were then prescribed at the inlet and outlet of the domain and a simulated acoustic source in the form of an oscillatory pressure component superimposed upon the mean flow applied at the inlet. The pseudo steady state pressure amplitudes from the mean flow solution were then subtracted from those obtained from the acoustic solution thereby giving a solution for the pressure field due to the applied acoustic perturbation only.

5.3.1 Geometry and Computational Grid Definitions.

A grid resolution of 50 cells per wavelength was prescribed with the limiting grid size based upon a maximum frequency of 800 Hz. The acoustic wave speed from the steady state data was approximately 389 m/s, therefore the minimum wavelength λ was calculated to be 0.426 metres and the required grid size to be approximately to 8.5×10^{-3} metres. A quadrilateral mapped grid was constructed using transfinite interpolation. The completed grid consisted of approximately 325,000 cells.

5.3.2 Boundary Conditions - Steady State Solution

The boundary conditions were as prescribed for Case Study 2

The timestep was specified as being 5×10^{-7} seconds so as to maintain a Courant number of 0.50. The coefficient of artificial viscosity initially set to 0.01 (1%). The solution proceeded for a total of 1.3×10^{6} timesteps although convergence of the mass flow and the u and v velocity residuals occurred after approximately 800,000 timesteps. The cpu time for the solution was approximately 76 hours.

In order to avoid repetition it is not considered necessary to again give contour plots of the flow variables for the steady state flow case with the finer grid, since they were similar to the solution data obtained on the coarser grid of Case Study 2.

5.3.3 Boundary Conditions - Acoustic Perturbation At 400 Hz

The non reflecting boundary conditions employed in this study were actually one dimensional relations and had assumed that the flow entered or exited the domain normal to the boundary. For the two cases to be considered here (a rectangular test duct and the compressor bleed system) it was found that the inlet boundary lay normal to the flow direction and hence the flow could be considered to be one dimensional for the inlet boundary in both cases. However, in the case of the compressor bleed system the outlet boundary was known to be orientated at an angle in such a way that it was non orthogonal to either the x or y axes in the global coordinate system. To adopt the form of the non reflecting boundaries employed here would require the velocity components normal and tangential to the outlet boundary to be known, these are illustrated below in Figure 5.3.1.

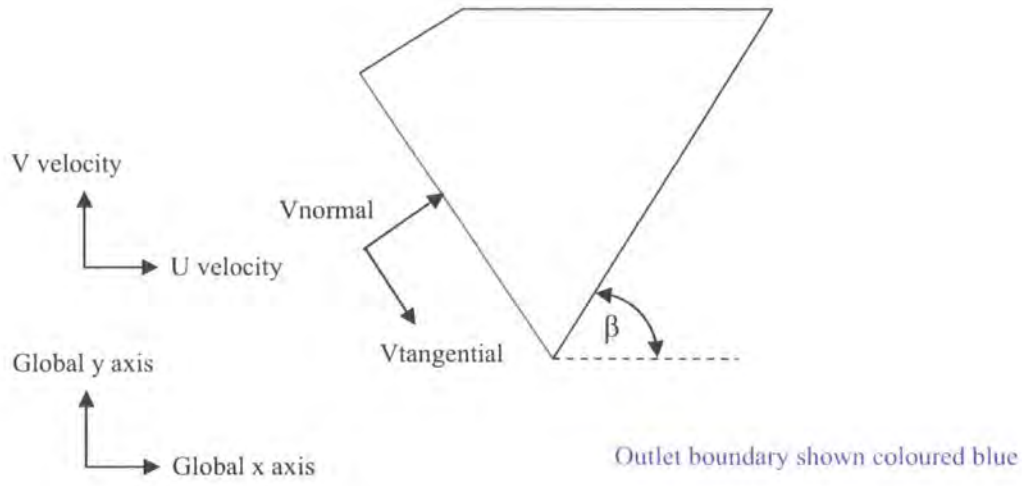

Figure 5.3.1

Knowing the values of the u and v velocity components at the outlet boundary and the angle (β) at which the outlet boundary lay with respect to the global x axis, the normal and tangential velocities at the outlet boundary, as required by the characteristic equations defining the non reflecting boundary could be calculated as follows.

V_normal(i) = (U_extrap_outlet(i)*cosine(beta)) +(V_extrap_outlet(i)*sin(beta))

V_tangential(i) = (V_extrap_outlet(i)*cosine(beta)) - (U_extrap_outlet(i)*sin(beta))

Where the angle β was calculated to be 23.44 degrees from engineering drawings for the compressor bleed system.

A characteristic based non reflecting boundary condition was applied at the inlet boundary having a stagnation pressure given by $P = P_0 + P_0.(Amp.\sin(\omega.t))$ where P0 was the stagnation pressure (equal to 130,000 Pa), *Amp* was the peak amplitude of the applied pressure perturbation and the angular frequency ω was calculated as $\omega = 2.\pi.f$ where f was the frequency of the applied perturbation. The stagnation temperature was specified as being 377 K

A characteristic based non reflecting boundary condition was applied at the outlet boundary with the exit pressure downstream being specified as being 101325.0 Pa.

The amplitude of the perturbation was specified as being 0.005 (corresponding to 0.5 percent of the stagnation pressure value) and the coefficient of artificial viscosity specified as being 0.001, corresponding to 0.1 percent.

5.3.4 Presentation Of Results- Acoustic Perturbation At 400 Hz.

For the unsteady case with the oscillatory inlet boundary condition the solution was run for a total of 300,000 timesteps. Since the initial flow field was taken to be from the converged steady state solution (i.e. Case Study 2) approximately 200,000 timesteps were initially performed to ensure that the perturbation applied at the inlet boundary could propagate fully through the entire domain. During this time the time histories of the mass flow at the inlet and outlet boundaries were closely examined and the solution continued until periodic behaviour at the same frequency was observed at the inlet and outlet boundaries. Once this was proven, an additional 100,000 timesteps were performed to generate the transient pressure data required for the acoustic study.

The desired outputs of the study were the pressure time history data acquired pre and post silencer and animated contour plots of the unsteady pressure wave amplitudes within the system.

To generate the time history data the instantaneous values of the static pressure were stored for each cell along a line of constant 'J' value at a location 0.20 metres above and below the silencer and at the inlet and outlet boundaries. The values for the static pressure for these same cells derived from the earlier steady state study (Case Study 2) were then subtracted to give values for the static pressure due only to the effect of the applied perturbation. These pressure values were then summated along the line of constant 'J' at each of the defined locations and the numerical value then divided by the number of cells to give a spatially averaged value for the static pressure due to the applied perturbation at each of the four desired locations. This value was then written to file at every timestep to give a continuous time history of the static pressure due to the applied perturbation at the four stated locations. Frequency spectra were then extracted using a Fast Fourier Transform (FFT) method thereby enabling a comparison of the frequency specific pressure amplitudes throughout the domain to be made. To generate animated contour plots of the unsteady pressure wave amplitudes within the domain the static pressure data for all cells in the domain was stored every 100 timesteps and from it subtracted the value of the static pressure obtained from the steady state solution.

A line contour plot of the instantaneous static pressure due to the applied perturbation is shown below as Figure 5.3.2.

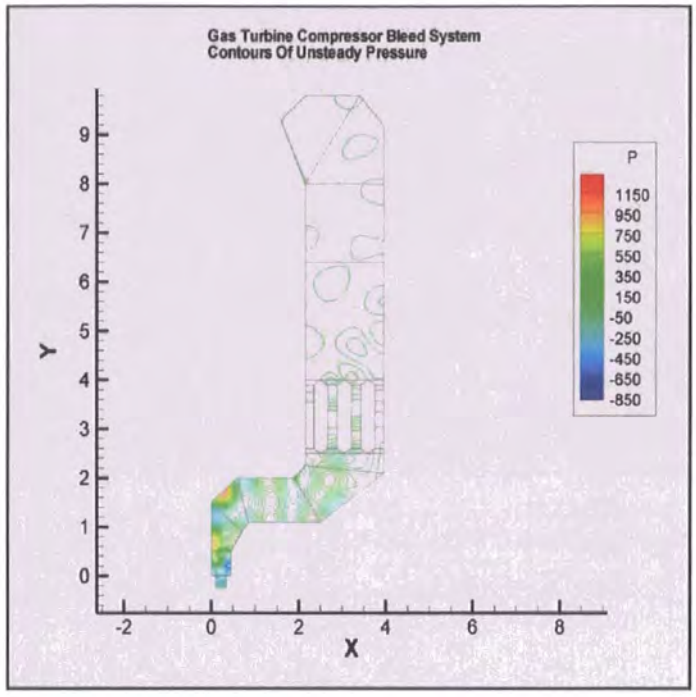

Figure 5.3.2

An FFT magnitude spectrum of the pressure time history pre and post silencer is shown below as Figure 5.3.3. A cosine (Hanning) window was applied during the FFT process.

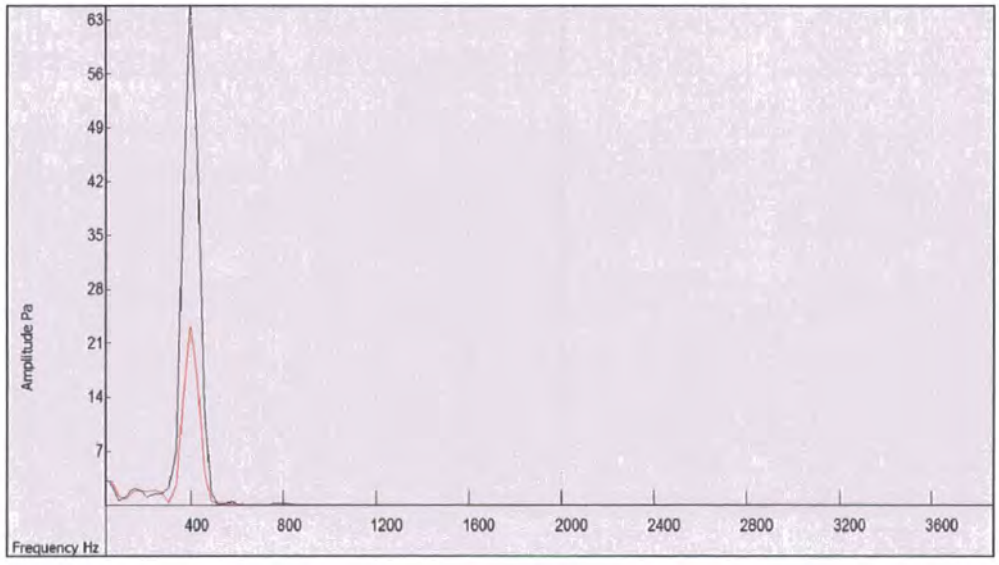

Figure 5.3.3
(Pre silencer spectrum shown black, post silencer spectrum shown red.)

5.3.5 Discussion Of Results - Acoustic Perturbation At 400 Hz.

Examination of the frequency spectrum (see Figure 5.3.3) showed some attenuation of the pressure wave amplitudes across the silencer with the magnitude of the 400 Hz frequency component decreasing from approximately 63 Pa pre silencer to 22 Pa post silencer. Unfortunately no analytical solution for the silencer attenuation existed and it was necessary to instead resort to comparisons with experimental test data available at AAF Ltd.

It was the author's understanding that acoustic testing had been undertaken in the past by acoustic engineers at AAF Ltd [23] where the silencer was installed into a section of unlined straight duct and a broadband white noise source applied. The insertion loss was then measured at a range of frequencies. The test data had indicated that at 400 Hz the peak pressure magnitude measured post silencer was approximately $1/3^{rd}$ of that measured pre silencer giving an effective attenuation of approximately 3:1 at this frequency.

Comparison of the frequency spectra pre and post silencer (see Figure 5.3.3) indicated that the apparent attenuation predicted by the Euler2D code was in general agreement with the test findings. This therefore provided some reassurance that the simple Euler method applied here could be usefully applied to the study of acoustic behaviour within such a complex domain such as the compressor bleed system studied here.

5.3.6 Boundary Conditions - Acoustic Perturbation At 800 Hz

Both the inlet and the outlet non reflecting boundary conditions were applied in an identical manner to that for the earlier 400 Hz study, except that the frequency of the applied perturbation at the inlet was increased from 400 Hz to 800 Hz.

The solver parameters were specified to be identical to those applied to the 400 Hz study undertaken earlier.

5.3.7 Presentation Of Results - Acoustic Perturbation At 800 Hz.

The pressure time history data pre and post silencer, and the animated contour data were produced in an identical manner as earlier. A line contour plot of the instantaneous static pressure due to the applied perturbation is shown as Figure 5.3.4. An FFT magnitude spectrum of the pressure time history pre and post silencer is shown as Figure 5.3.5. Note that a cosine (Hanning) window was applied during the FFT process.

In addition the waveform and FFT magnitude spectra of the pressure time history was evaluated at point locations defined in the geometric centres of each of the 23 blocks within the domain. These are presented for selected blocks as Figures 5.3.6 to 5.3.13. Note that a cosine (Hanning) window was applied during the FFT process.

Finally, plots of the static pressure at times t = 0.013 seconds and t = 0.024 seconds are provided as Figures 5.3.14 and 5.3.15.

A line contour plot of the instantaneous static pressure due to the applied perturbation is shown below as Figure 5.3.4.

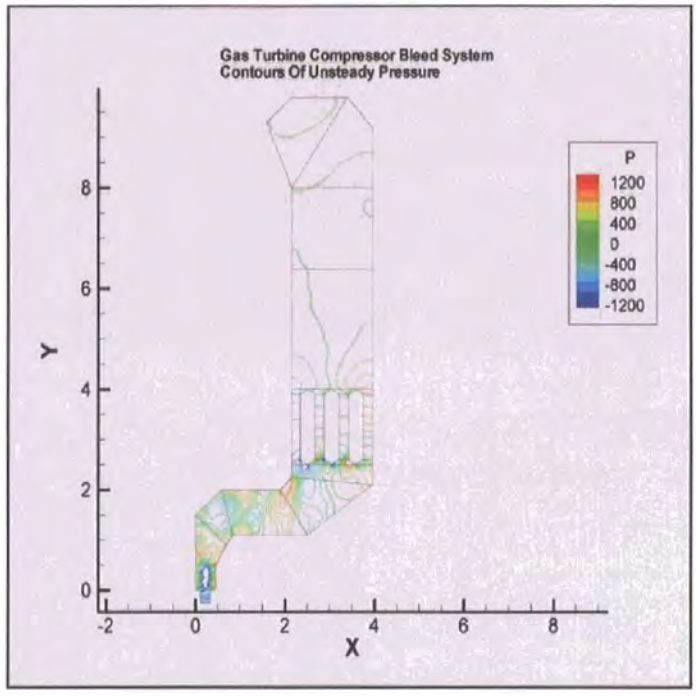

Figure 5.3.4

An FFT magnitude spectrum of the pressure time history pre and post silencer is shown below as Figure 5.3.5. A cosine (Hanning) window was applied during the FFT process.

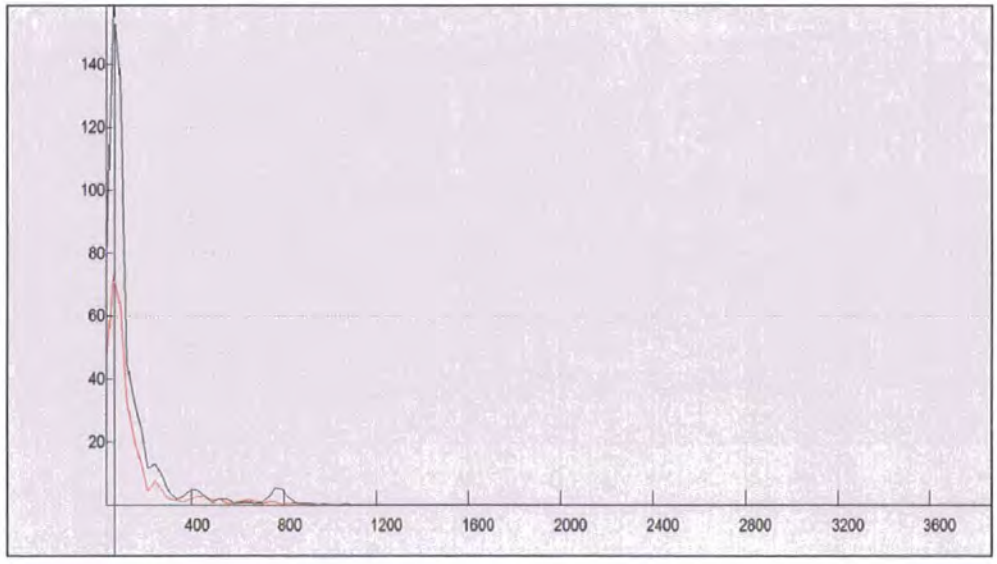

Figure 5.3.5

(Pre silencer spectrum shown black, post silencer spectrum shown red.)

Time history and frequency spectra acquired within the inlet and offset transition.

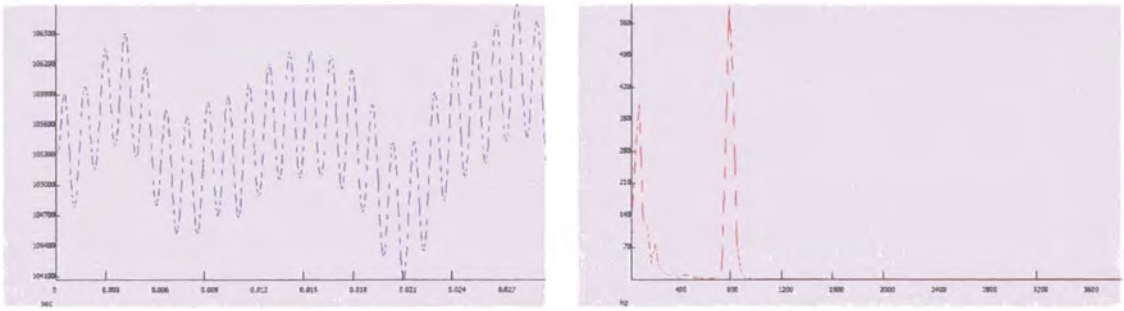

Figure 5.3.6 (Block 23 time history)

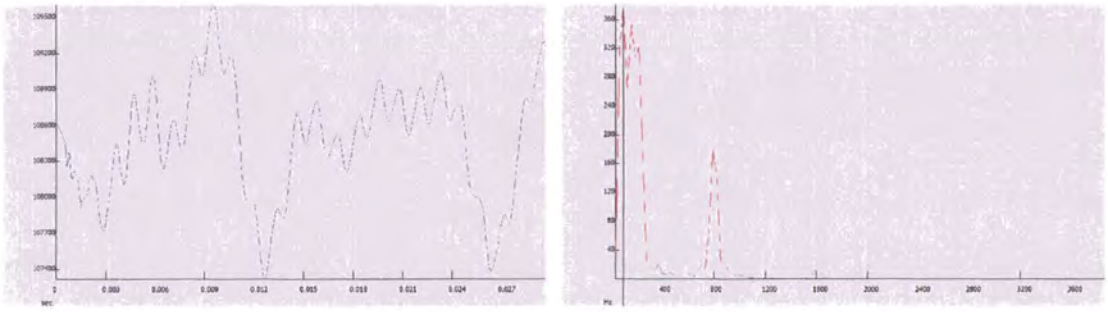

Figure 5.3.7 (Block 2 time history)

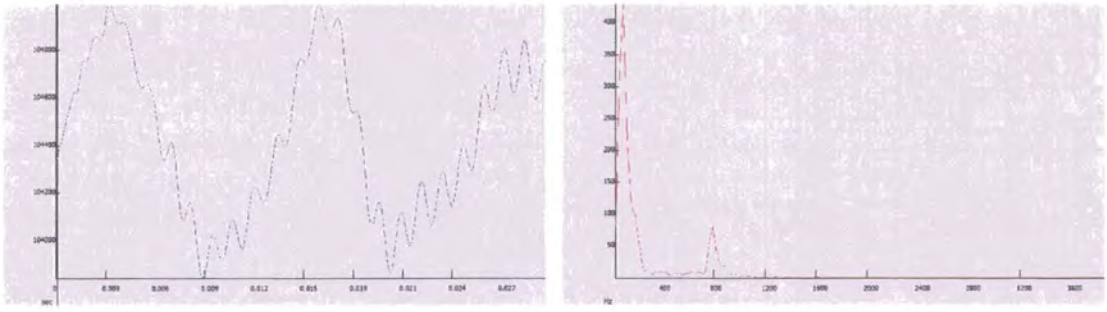

Figure 5.3.8 (Block 4 time history)

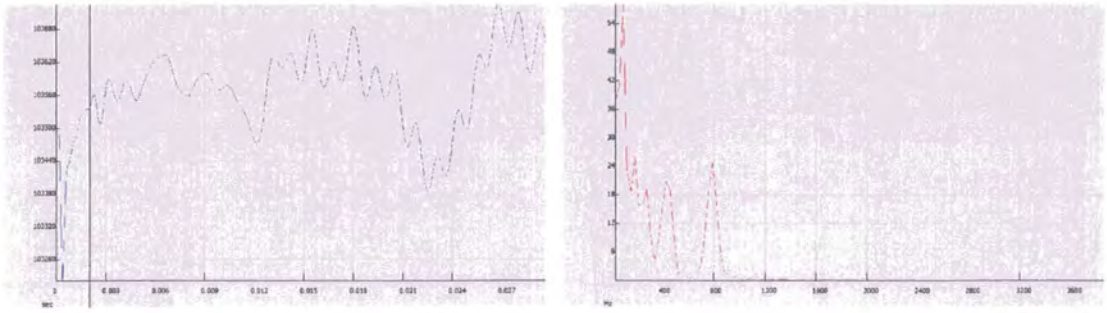

Figure 5.3.9 (Block 6 time history)

Time history and frequency spectra acquired within the bleed silencer.

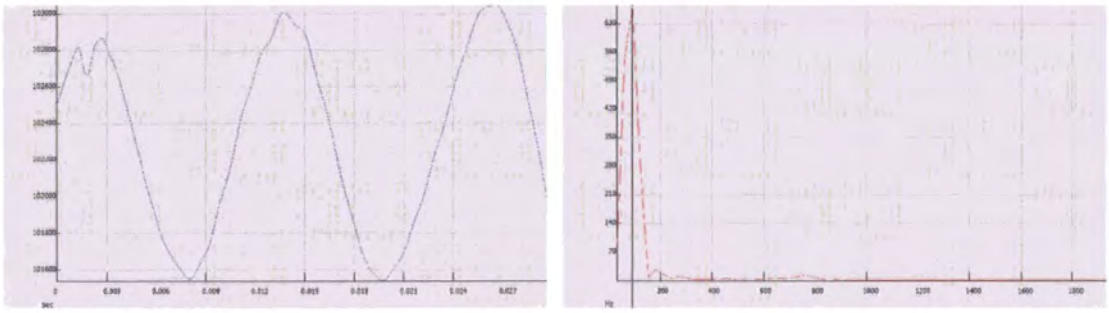

Figure 5.3.10 (Block 11 time history)

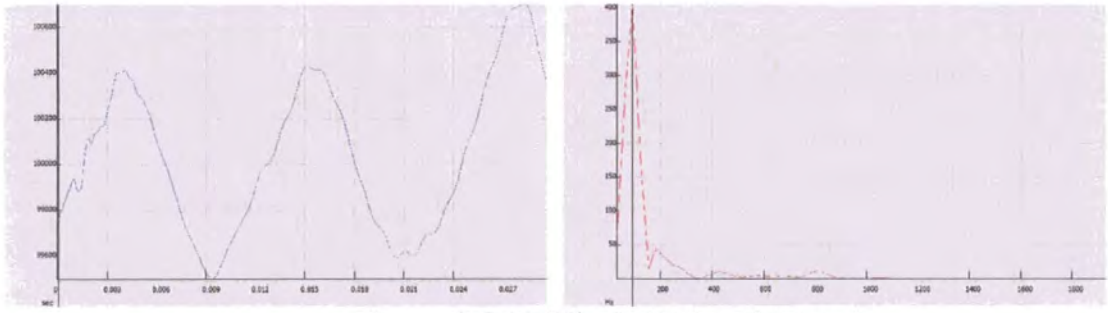

Figure 5.3.11 (Block 12 time history)

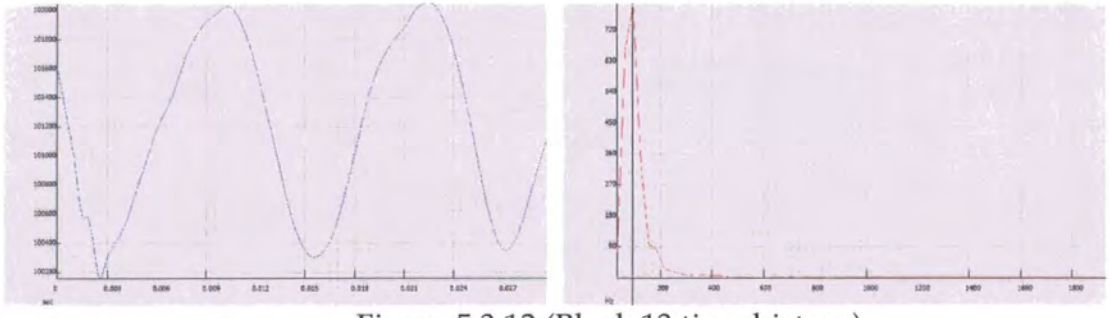

Figure 5.3.12 (Block 13 time history)

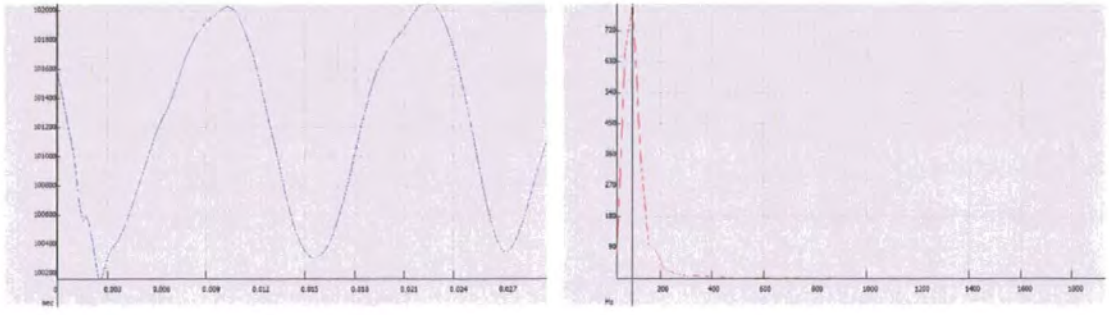

Figure 5.3.13 (Block 14 time history)

Vector data acquired at time t = 0.013 seconds and t = 0.024 seconds.

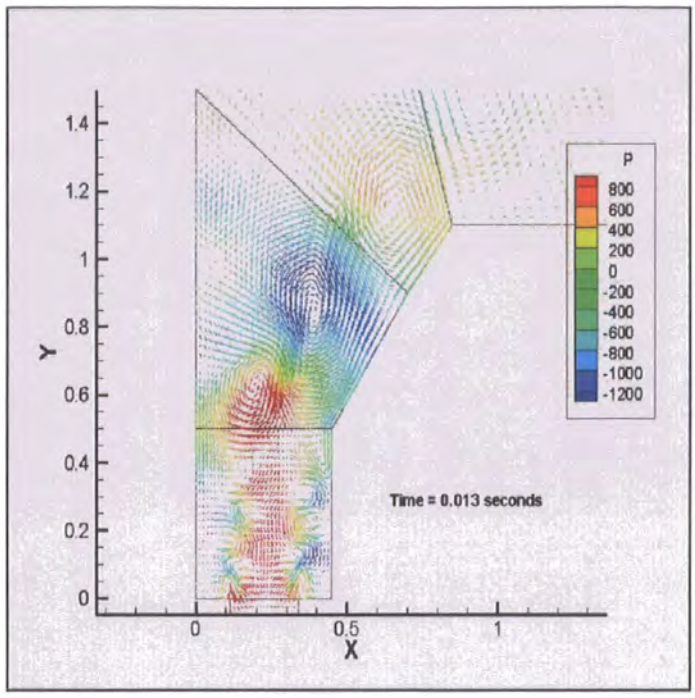

Figure 5.3.14 (Time t = 0.013 seconds)

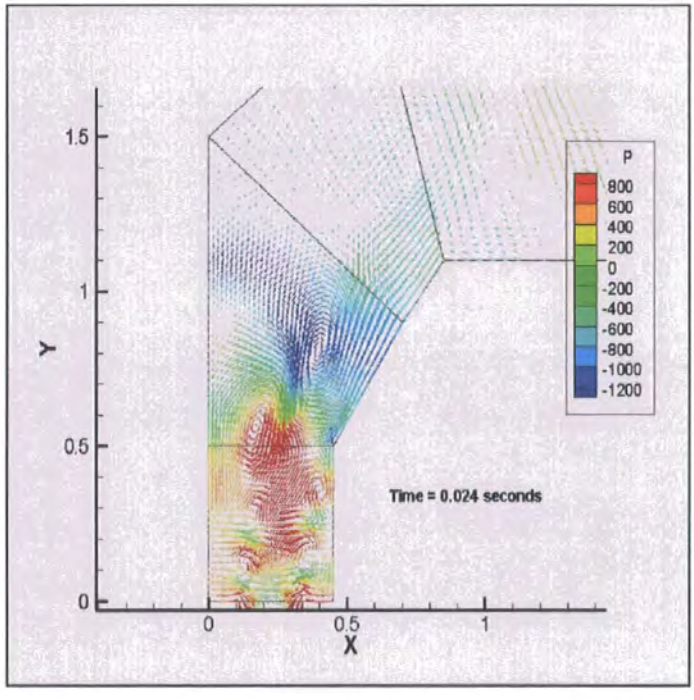

Figure 5.3.15 (Time t = 0.024 seconds)

5.3.8 Discussion Of Results - Acoustic Perturbation At 800 Hz.

Examination of the frequency spectrum (see Figure 5.3.5) showed some interesting, and unexpected characteristics. Most obvious was the emergence of a dominant lower frequency component at 91 Hz pre and post silencer. In addition the amplitude of the original 800 Hz frequency component pre silencer was significantly less than that found at the same location for the 400 Hz study. This was unexpected as the wave amplitude of the perturbation frequency applied at the inlet was identical for both the 400 Hz and the 800 Hz studies.

The causes of both the low amplitude of the frequency component pre silencer and the emergence of the dominant lower frequency component were not clear. However it was considered that these may possibly be due to the effects of numerical damping, errors in the signal processing of the original time history data or a true physical effect due to unexpected unsteady flow phenomena in the compressor bleed system. Each of these were considered in turn as follows.

The low amplitude of the 800 Hz component pre silencer was a concern in that it was thought that this could possibly be a result of numerical damping due to either an inadequate grid resolution or excessive value of the artificial viscosity damping coefficient. However, in accordance with the grid sensitivity studies undertaken earlier, great care had been taken to ensure that a minimum grid resolution of approximately 50 cells/wavelength had been maintained. The grid resolution for this study was calculated to be a minimum of 48 cells/wavelength, increasing to 100 cells/wavelength in blocks 23 and 1 (these being the two blocks closest to the inlet boundary). In addition the value of the artificial viscosity damping coefficient had been maintained at 0.1 percent. It was therefore considered unlikely that the unexpectedly low amplitude of the 800 Hz frequency component could be attributed to numerical damping.

The emergence of the dominant lower frequency components at 91 Hz was unexpected and it's origin not immediately obvious. However, one possibility was that it could be a result of under sampling, i.e. an alias frequency. However, based upon the value of the timestep of $5x10^{-7}$ seconds and the fact that the time history data had been written to file for every timestep the sampling frequency was calculated to be 2 MHz. Under sampling to produce an alias frequency at 61 Hz was therefore discounted.

A further possibility was that the creation of the lower frequency components were a result of unsteady flow behaviour or an acoustic mode within the bleed system itself. To investigate this the static pressure at the geometric centre of all blocks in the domain was written to file at every timestep to produce a pressure time history map for the entire domain. It was not considered practical to illustrate all of the time history waveform and FFT spectra in this study due to the large number of datasets. However, the pressure time history waveform and FFT were evaluated for a select number of blocks, these being block 23 (inlet), blocks 2, 4 & 6 (offset transition) and blocks 11,12,13,& 14 (flow passages within the bleed silencer).

Examination of the pressure time history data at the centre of block 23 (i.e. the block defining the inlet, see Figure 5.3.6) showed clearly the dominance of the applied perturbation frequency of 800 Hz, however an unexpected and large amplitude lower frequency component was also evident at 91.5 Hz. Inspection of the time waveform revealed that the 800 Hz perturbation frequency was modulated at a much lower frequency and measurements of the time interval between modulation periods indicated a modulation frequency of 91.5 Hz. This therefore was considered to be the origin of the unexpected lower frequency of 91.5 Hz evident in the frequency spectrum.

Continuing through the domain to block 4 (see Figure 5.3.8) it was again found that the 800 Hz frequency component due to the applied perturbation was detected, however the lower frequency component of 91.5Hz again dominated the frequency spectrum and modulation of the pressure time waveform at this frequency was clearly evident as the source.

Continuing further to the bleed silencer itself (see Figures 5.3.10 to 5.3.13) some interesting characteristics were evident. Firstly, the pressure time waveform evaluated at the centre of blocks 11 to 14 defining the silencer flowgaps resembled almost a pure sinusoid at a frequency of 91.5 Hz. Furthermore the time waveform data were seen to be in phase for blocks 11 & 12, and for blocks 13 & 14, however a 180 degree phase shift was apparent between block sets (11&12) and (13&14). This was quite unexpected, but indicative of an unsteady, oscillating flow developing within the silencer itself. Examination of the animated pressure contour data indicated that this appeared to be largely a result of flow separation from the inner radius of the offset transition adjacent to the leftmost flow gap at the interface between blocks 4 and 5.

However, the origin of the dominant frequency component of 91.5 Hz still remained to be determined. To investigate this animated contours of the pressure data generated from the unsteady flow solution were examined.

Referring to Figures 5.3.14 and 5.3.15 close examination appeared to show that the low frequency modulation of the pressure was a result of constructive interference of vortices shed at the interface between the domain inlet (block 23) and the first section of the offset transition (block 1) where sudden enlargement of the cross section area occurred. Examination of Figure 5.3.14 at time = 0.013 seconds showed the formation of a lower pressure region in the flow that was observed to propagate through the domain toward the silencer. This behaviour was repeated at time = 0.024 seconds. The time interval between occurrences was found to be equal to 0.011 seconds, equivalent to a frequency of 91 Hz.

This low frequency modulation of the acoustic pressure wave amplitudes within the bleed system was unexpected as technically an inviscid solution cannot produce viscosity dependent phenomena such as flow separation or vortex shedding. It is suggested that the presence of singularities in the domain caused by the creation of sharp corners at the inlet block interfaces together with the addition of artificial viscosity in the solution are responsible for the viscous type behaviour observed in

the solution. Furthermore it is also suggested that due to the relatively high inlet velocity and silencer flowgap spatial velocity this phenomena may be dominated by inertial rather than viscous effects, hence it's presence in the Euler solution is justified.

With regard to the attenuation properties of the silencer at the applied perturbation frequency of 800 Hz, close examination of the frequency spectrum pre and post silencer (see Figure 5.3.5) indicated the amplitude of the 800 Hz component to be approximately 5.3 Pa pre silencer and 1.1 Pa post silencer. Since no analytical solution for the silencer attenuation existed it was again necessary to resort to comparisons with experimental test data available at AAF Ltd. Unfortunately actual test data could not be procured, however during private discussions with senior acoustic staff at AAF Ltd it was suggested that based upon historical test data at a frequency of 800 Hz the attenuation ratio should be approximately 16:1, i.e. the pressure wave amplitude post silencer should be one sixteenth that of the wave amplitude pre silencer.

Although the numerical solution had indicated an attenuation ratio of approximately 5:1 rather than the 16:1 expected from the experimental test data, it was considered that the apparent attenuation predicted by the Euler2D code was in general agreement with expectations from historical test data. This thereby provided confirmation that the code could usefully be applied to the study of the acoustic behaviour of the compressor bleed system.

5.4 Case Study 4
Design Study Of An Industrial Gas Turbine Compressor Emergency Bleed System.

The studies undertaken so far had shown that the two stage Euler scheme combined with the use of non reflecting boundary conditions could provide useful information regarding the acoustic characteristics of the compressor bleed system and in particular the attenuation properties of the silencer. However, it was felt that it could also possibly provide a useful means to study the effects of silencer location on overall system attenuation.

In order to investigate this two studies were conducted as follows. The first was a baseline study utilising the same geometry as that featured in the steady state study undertaken earlier. The second would be an identical study to the first, except that the silencer would be moved 3.0 metres upward in the vertical ducting to a position nearer to the outlet cowl. By relocating the silencer to a position nearer to the outlet it was expected that the attenuation of the system as a whole could be reduced, thereby proving that a simple rearrangement of the system configuration could affect system performance.

5.4.1 Geometry and Computational Grid Definitions.

The geometry was modified such that the bleed silencer was relocated to a new position in the vertical duct 3.0 metres above it's previous location. The geometry configuration for the bleed system with the relocated silencer is shown below in Figure 5.4.1.

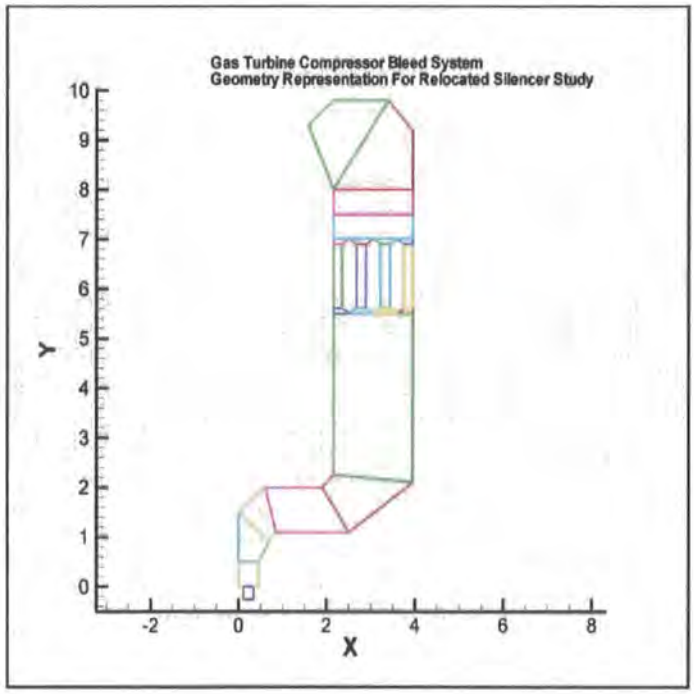

Figure 5.4.1

5.4.2 Computational Grid And Solution Parameters

It was considered essential that any changes in the attenuation properties of the system be due solely a result of the change of silencer location, therefore an identical computational grid featuring the same number and spacing of cells for each of the two system geometries considered was created. By doing so the numerical damping inherent in the solution ought to be identical for each of the two cases studied, and hence any visible changes in the acoustic characteristics ought to be solely a result of geometric changes. Furthermore all solution parameters (timestep, Courant number, artificial viscosity damping coefficient) and boundary condition specifications were identical for both studies.

In the interests of reducing the time required for solution of the problem, the study was conducted on the same computational grid as that employed for the original steady state study (Case Study 2). Based upon the grid spacing, and maintaining a grid resolution of 50 cells/wavelength, the perturbation frequency at the inlet was set to 200 Hz.

5.4.3 Boundary Conditions - Mean Flow.

Conventional reflecting boundary conditions for a subsonic flow were applied in order to achieve a steady state solution. These were as follows.

At the inlet boundary a stagnation pressure of 130000 Pa and a stagnation temperature of 377 K were applied.
At the outlet boundary a static pressure of 101325.0 Pa was applied to achieve a mass flow of 54 Kg/second.

5.4.4 Boundary Conditions - Unsteady.

At the inlet boundary a characteristic based non reflecting boundary condition was applied having a stagnation pressure given by $P = P_0 + P_0.(A.\sin(\omega.t))$ where P0 was the stagnation pressure (equal to 130,000 Pa), A was the peak amplitude of the applied pressure perturbation and the angular frequency ω was calculated as $\omega = 2.\pi.f$ where f was the frequency of the applied perturbation (in this case 200 Hz). The stagnation temperature was specified as 377 K.
At the outlet boundary a characteristic based non reflecting boundary condition was applied, with the exit pressure downstream being specified as being 101325.0 Pa.

5.4.5 Solver Parameters.

The amplitude of the perturbation was specified as being 0.005 (corresponding to 0.5 percent of the stagnation pressure value) and the coefficient of artificial viscosity specified as being 0.004, corresponding to 0.40 percent. As in the previous studies 200,000 timesteps were performed using reflecting boundary conditions until the solution was deemed to have reached a converged steady state, then the non reflecting boundary conditions were implemented and the solution continued for another 100,000 timesteps.

5.4.6 Presentation Of Results

The pressure time history data was generated in an identical manner as before with the frequency spectra then extracted using a Fast Fourier Transform (FFT) method.

Contour Data.

Contour plots showing velocity magnitude data are shown in Figures 5.4.2 and 5.4.3.

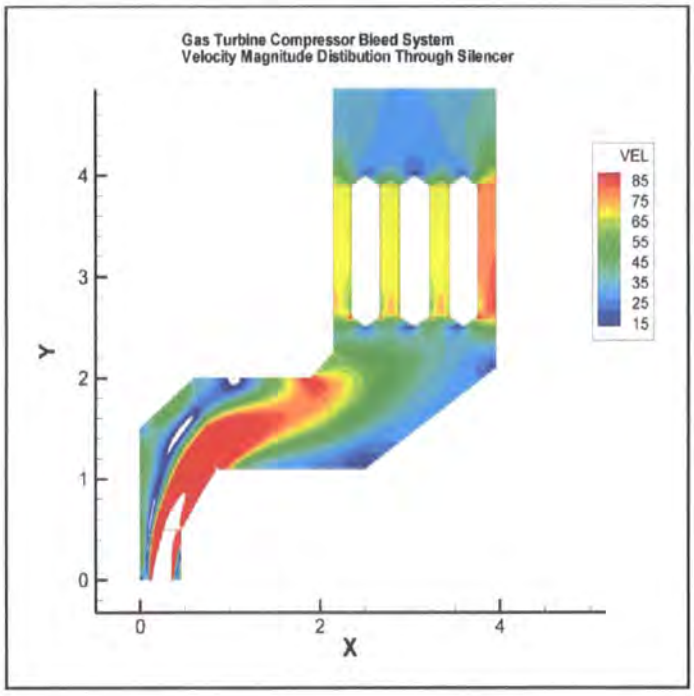

Figure 5.4.2

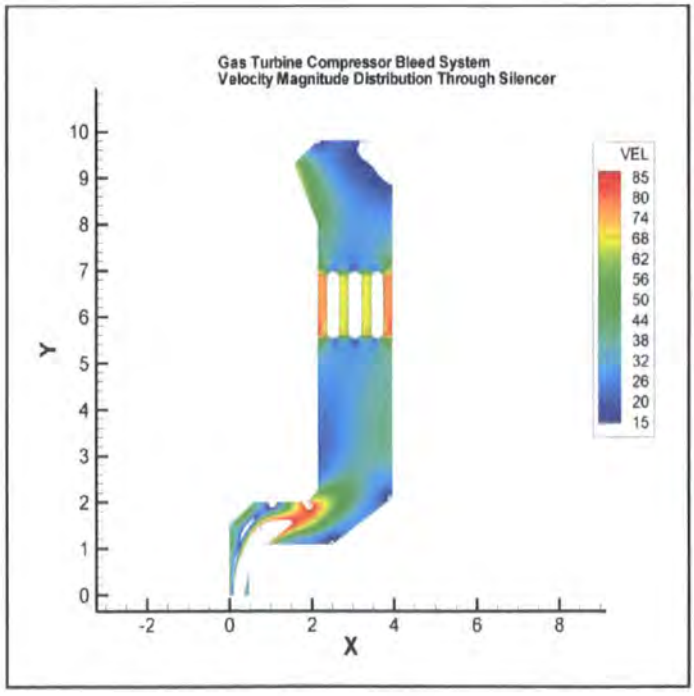

Figure 5.4.3

Time Waveform And Frequency Spectra.

Time domain and frequency spectra of the pressure wave amplitude at the inlet boundary are shown as Figures 5.4.4 and 5.4.5 respectively.

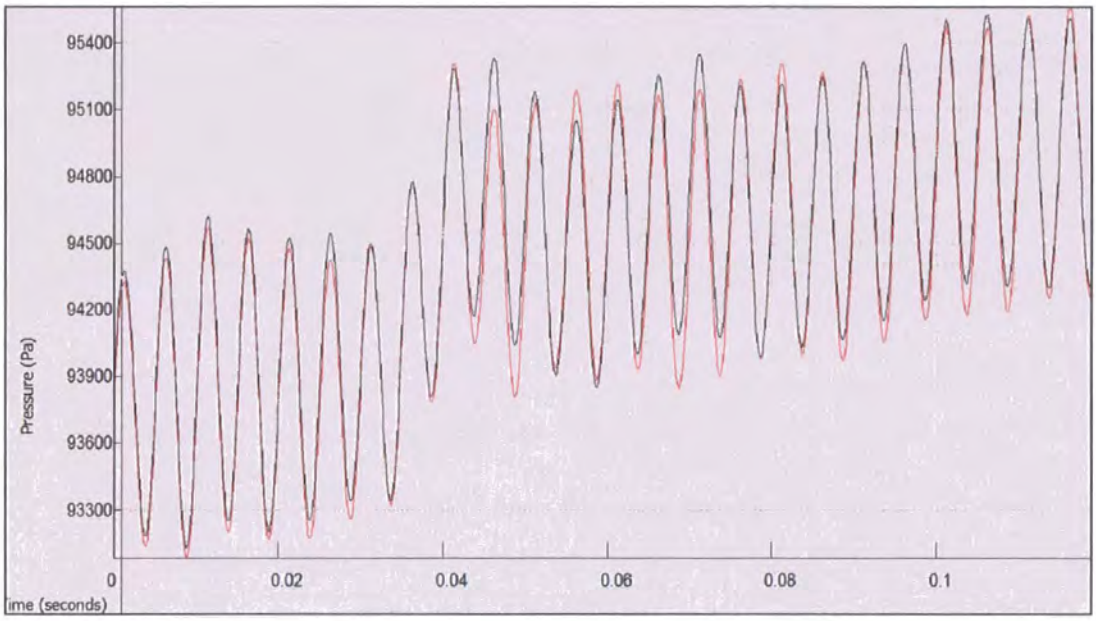

Figure 5.4.4
(Original silencer location is shown black, relocated silencer is shown red.)

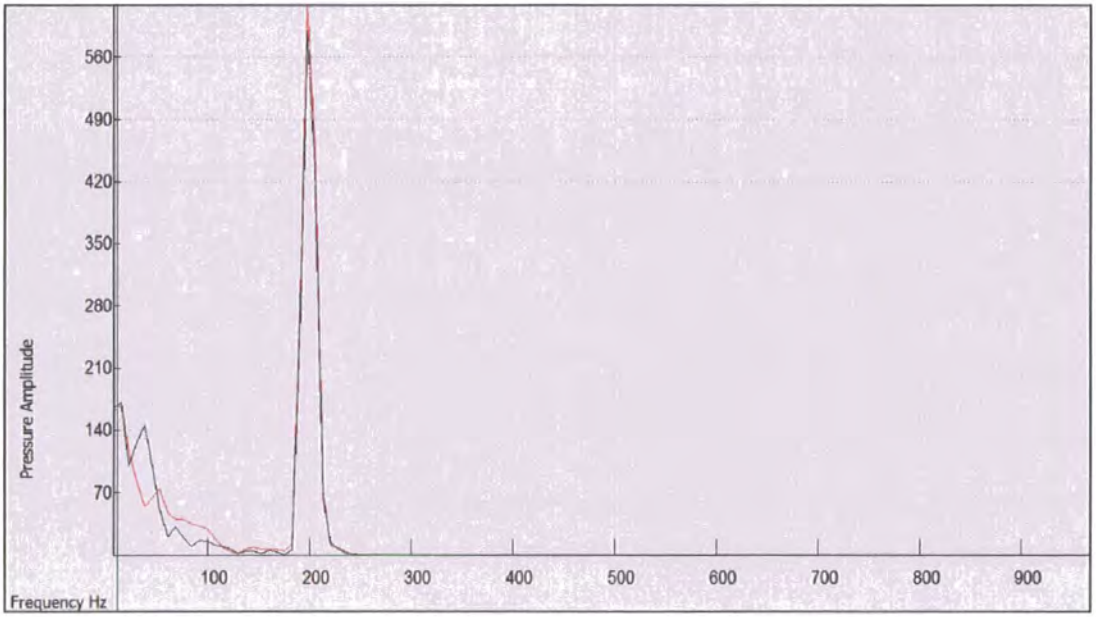

Figure 5.4.5
(Original silencer location is shown black, relocated silencer is shown red.)

Time domain and frequency spectra of the pressure wave amplitude pre silencer are shown as Figures 5.4.6 and 5.4.7 respectively.

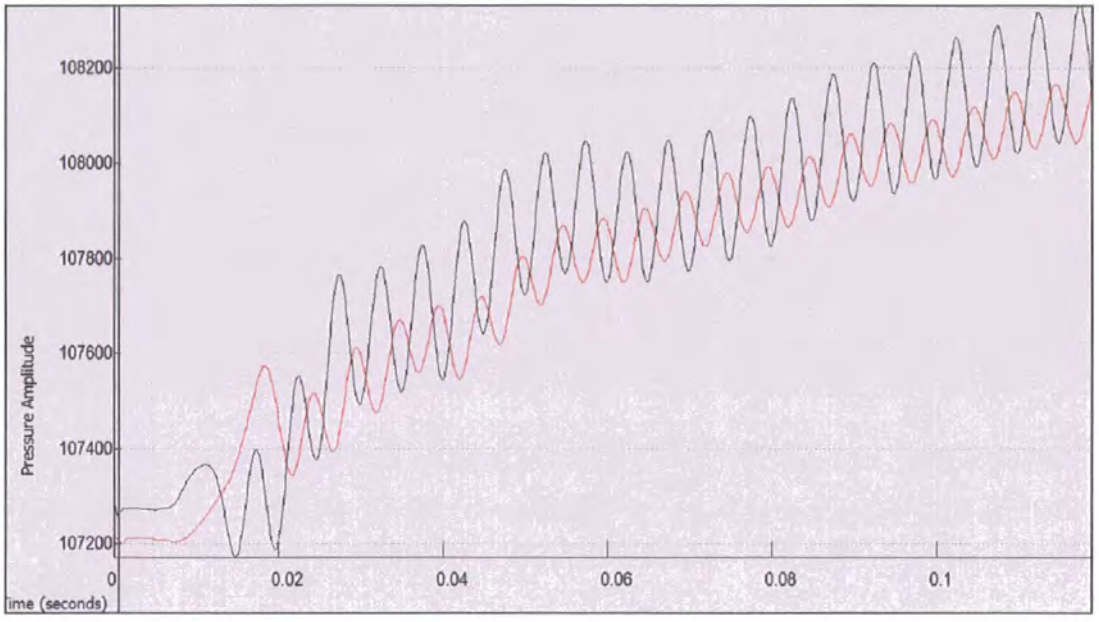

Figure 5.4.6
(Original silencer location is shown black, relocated silencer is shown red.)

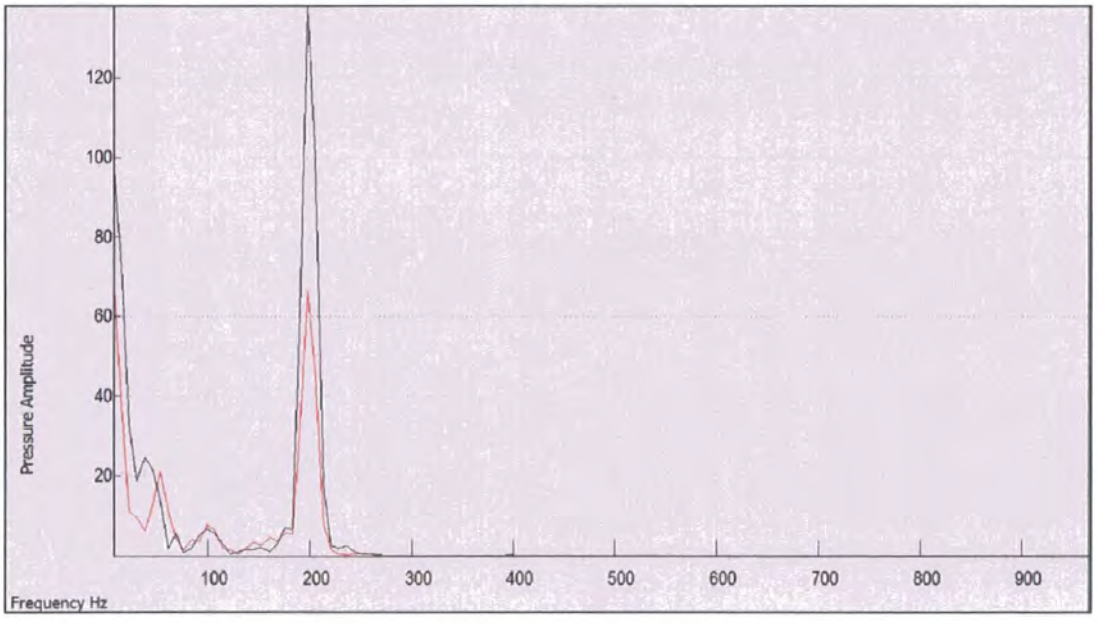

Figure 5.4.7
(Original silencer location is shown black, relocated silencer is shown red.)

Time domain and frequency spectra of the pressure wave amplitude post silencer are shown as Figures 5.4.8 and 5.4.9 respectively.

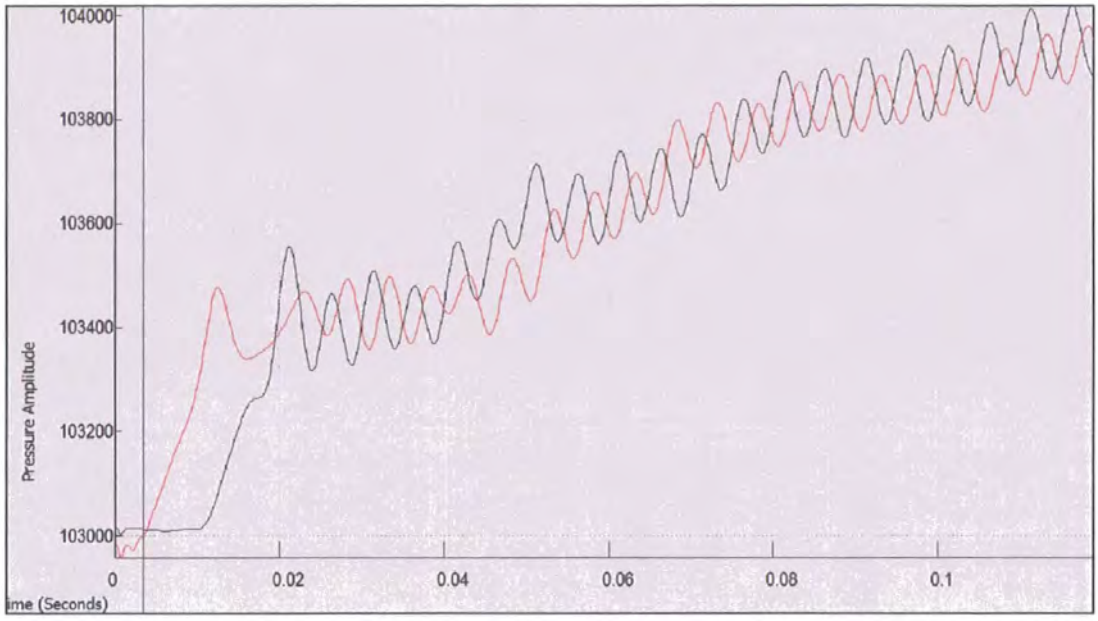

Figure 5.4.8
(Original silencer location is shown black, relocated silencer is shown red.)

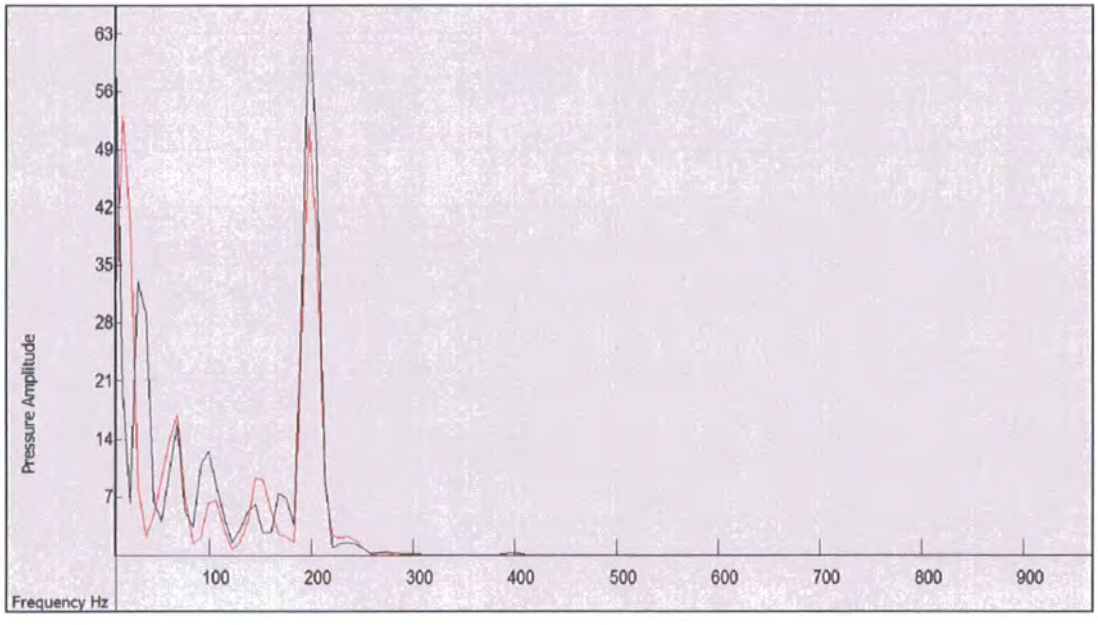

Figure 5.4.9
(Original silencer location is shown black, relocated silencer is shown red.)

Time domain and frequency spectra of the pressure wave amplitude at the outlet boundary are shown as Figures 5.4.10 and 5.4.11 respectively.

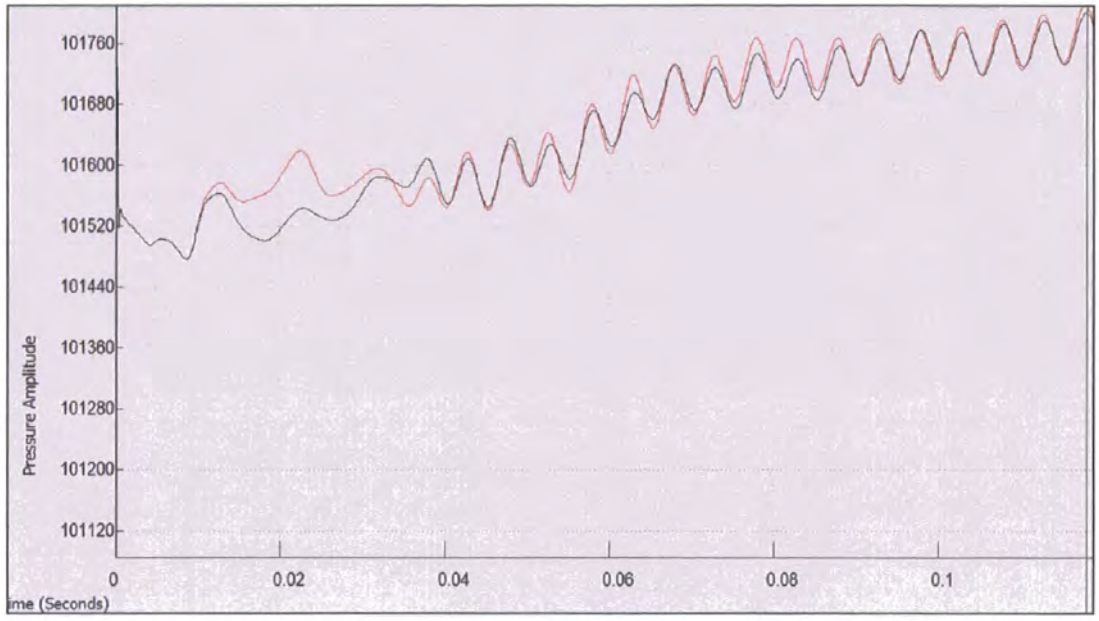

Figure 5.4.10
(Original silencer location is shown black, relocated silencer is shown red.)

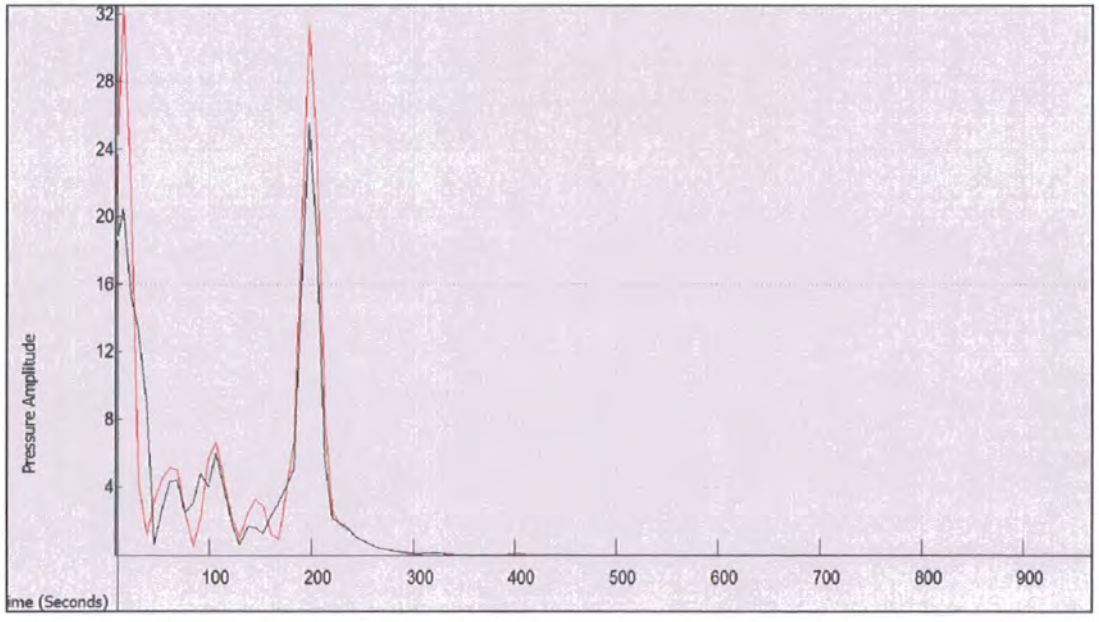

Figure 5.4.11
(Original silencer location is shown black, relocated silencer is shown red.)

5.4.7 Discussion Of results

General Flow Characteristics

Examination of the contours of velocity magnitude for both systems (see Figures 5.4.2 and 5.4.3) showed slightly higher flow velocity magnitudes through the silencer flow passages for the system featuring the relocated silencer. The actual values found at the mid point of the silencer flow passages were as follows (readings taken from left to right).

Original system : 66.7, 67.0, 67.1, 79.4 m/s
Relocated system : 75.0, 66.3, 67.0, 76.8 m/s
(Note that these figures are for unit silencer depth and have not been corrected for the true physical silencer depth).

The higher silencer spatial velocities found for the relocated system were attributed to flow separation and reattachment occurring downstream of the offset elbow transition as the flow entered into the vertical duct section containing the silencer. In the original system it appeared that the closer proximity of the silencer to the elbow duct reduced the tendency for the flow to separate, and whilst the flow velocity through the rightmost flow passage was higher at 79.4 m/s (due to an increase of static pressure at the wall at this location), the overall flow distribution through the remaining three flow passages was quite uniform ranging from 66.7 to 67.1 m./s.

It is also noted that higher flow velocities in the numerical solution (by an approximate factor of 2) caused by the assumption of unit silencer depth would affect the acoustic solution. However since the acoustic wave speed would be much greater than that of the mean flow it was considered that the higher mean flow velocities would not significantly affect the acoustic solution.

Acoustic Characteristics

Examination of the pressure time history and frequency spectra for the domain indicated a general loss of attenuation performance for the system featuring the relocated silencer. More specifically:

Examination of Figures 5.4.4 and 5.4.5 indicated that the pressure wave amplitudes were generally similar at the inlet boundary, this was as expected and provided a confirmation that the inlet conditions were equivalent for both layouts. At the pre silencer location examination of Figures 5.4.6 and 5.4.7 indicated a reduction of the pressure wave amplitudes recorded for the system featuring the relocated silencer. Again, this was not unexpected and was considered likely to be due to reflection effects from the walls of the offset transition being less and the flow being diffused within the vertical ducting before encountering the silencer.

At the post silencer location it was apparent that the differential between the magnitudes of the pressure wave amplitudes had reduced (see Figures 5.4.8 and 5.4.9). This was attributed to the diffusive effect of the silencer upon the airflow.

Furthermore a comparison of the pressure wave amplitudes at the outlet boundary (see Figures 5.4.10 and 5.4.11) indicated a noticeable increase of pressure wave amplitude for the system featuring the relocated silencer, in agreement with expectations.

5.4.8 Conclusions

It was found that the effect of relocating the silencer to a position nearer to the outlet cowl had an undesirable effect upon both the aerodynamic and acoustic characteristics of the system as a whole. More specifically an increased tendency for preferential flow through the baffle silencer and an elevation of the acoustic pressure wave amplitudes at the outlet boundary were found. These are discussed below.

The effect of relocating the silencer within the system appeared to permit some separation of the flow to occur at the elbow bend resulting in an asymmetric velocity profile within the vertical section of ducting and consequenct preferential flow through the silencer. This was prevented to some extent in the original configuration by the closer proximity of the silencer to the elbow bend imposing a higher backpressure upon the flow in the vicinity of the elbow bend thereby reducing the tendency for flow separation to occur. It could therefore be implied that from an aerodynamic perspective it would be desirable to locate the silencer as close as practically possible downstream of geometric features likely to promote flow separation such as elbow bends, sudden enlargements of duct cross section or divergent transitions.

In addition an increase of the acoustic pressure wave amplitudes measured at the outlet boundary was also found for the relocated system. This was not unexpected since it was envisaged that closer proximity of the silencer to the acoustic source should result in greater attenuation of the source as measured at the outlet boundary. Since the computational grid and solver parameters were identical for both studies it was reasoned that the numerical dissipation inherent in the numerical scheme ought to be equivalent for each study. Therefore it was concluded that the differences noted in pressure wave amplitudes within the domain and hence the attenuation properties of the system were not an artefact of the numerical scheme and therefore ought to be a genuine physical effect resulting from a change of system geometry. Since present methods for acoustic design reliant upon insertion loss measurements cannot account for the effects of system geometry and configuration this was considered to be an important finding since it indicated that the two stage Euler solution employed in this study could be used not only to predict the acoustic characteristics of an individual component such as the baffle silencer but could also be used to optimize it's placement and system configuration so as to improve the acoustic performance of the overall system. In this regard the two stage Euler solution could be considered to advance the present state of the art.

6 Conclusions And Recommendations.

6.1 Conclusions

It has been shown in this study that a simple two stage time domain solution of the Euler equations can be usefully applied to the aerodynamic and acoustic design of industrial gas turbine intake and exhaust silencing systems, providing an accurate and robust means for solving for both the mean flow and the acoustic field. The method developed herein was found to fulfil the primary objective of the study, this being to devise a numerically based design tool that could offer a means to predict the aerodynamic and acoustic behaviour of an industrial gas turbine intake or exhaust system without the need for the costly procurement and testing of physical prototypes. The advantages of adopting the numerical approach developed in this study over the current empirically based design methods may be summarised as follows.

Since the two stage CFD based numerical approach presented in this study permitted a solution for both the mean flow and the acoustic field to be obtained, unexpected or undesirable acoustic or aerodynamic characteristics could be readily identified and appropriate design changes implemented. For example undesirable aerodynamic characteristics such as asymmetry in duct velocity profiles and preferential flow were easily identified in both of the industrial case studies and from these their impact upon system performance criteria such as differential pressure drop could be assessed by engineers at the concept stage of the system design. Furthermore it was found that the acoustic solution may also indicate acoustic characteristics not foreseen at the concept design stage, an example of this being found in the study of the compressor bleed system where lower frequency acoustic components formed as a result of unsteady flow within the domain and unrelated to the original source were found to dominate the frequency spectrum.

It was also demonstrated that the two stage CFD based method offered the possibility of conducting 'what if' design scenarios where optimisation of system aerodynamic and acoustic performance could be undertaken. An example of this is demonstrated in the case of the emergency compressor bleed system where a reduction of overall system acoustic attenuation was found as a result of a simple rearrangement of the baffle silencer.

In summary the two stage CFD based method developed in this study was considered to offer a useful design tool which could be used by engineers on a day to day basis for the practical design and analysis of gas turbine silencing systems and consequently offers an advancement of the current state of the art. Some implementation issues exist that may present some inconvenience for it's use particularly in the areas of grid generation, however it is felt that these could be addressed by further work to include the use of adapted, unstructured or multigrid methods or the adoption of higher order schemes. These are discussed below.

6.2 Recommendations For Future Work

Whilst the Euler scheme developed herein was found to be a useful analysis tool, it was considered that its formulation or implementation could be improved. A number of areas where further work could be warranted are proposed below.

- Use of adapted grids, unstructured grids or multigrid methods.
- Use of higher order schemes to reduce grid requirements.
- Use of parallel processing or 64 bit compilation for the source code.
- Extension of the scheme to a Navier Stokes solution.
- Extension of the scheme to a 3D solution.

Each of these are considered in turn as follows.

Use of adapted grids, unstructured grids or multigrid methods.

Acoustic problems by their very nature tend to require considerable computational resource and it is in this area that it is felt the most significant improvements could be made. In particular the construction of the computational grid was found to be time consuming and represented by far the most significant time requirement on the user. A number of techniques exists that may serve to reduce either the user interaction required for grid generation or the overall time required for solution. Those which may be considered to be worthy of future study are discussed below.

Adapted grids

One of the drawbacks of the Euler2D code developed in this study was the need to ensure a sufficiently refined grid in all areas of the domain to resolve the acoustic field. Given that the acoustic wave speed is high relative to the mean flow it is considered that adapted grids would be of little use. However, if the object of the study was merely to undertake an aerodynamic solution then an adapted grid could prove to offer considerable savings in computational overhead. It is envisaged that the adapted grid could take the form of a modification to the solver wherein the grid is automatically refined based upon gradients of density. However, in the interests of computational efficiency a means may need to be found (such as local time stepping) to enable a change of timestep locally within the domain so as not to violate the local Courant stability criterion. This would make a time dependent solution difficult (hence it's unsuitability for the acoustic solution), although it could be applied to obtain a pseudo steady state solution. In addition, since abrupt changes in density gradients are often found to occur at solid boundaries, some means of redefining the wall boundaries for those cells undergoing adaptation that lie at a solid surface (such as the Cartesian cut cell method) would need to be devised.

Unstructured grids

The use of the structured multiblock grid employed in this study does have its advantages, namely the ease at which it is implemented and the efficiency of memory storage in the flow solver. However multiblock structured grid creation was

found to be a very intensive and time consuming process. Unstructured grids based upon methods such as Delaunay Triangulation to automatically mesh the computational domain with triangles or tetrahedral offer the possibility of automating the grid creation process greatly reducing user intervention. They do however have a number of disadvantages, the most obvious of these being the higher memory storage requirement and the increased risk of solution divergence or inaccuracy resulting from a poorly constructed grid featuring highly skewed cells. In the context of the Euler2D grid and solver codes developed herein the use of an unstructured triangular grid is not considered to be practical since it would only be applicable to the solution of a pseudo steady state mean flow, whereas many of the flow features of interest (such as vortex shedding) are transient in nature. It is added that the use of unstructured grids would also necessitate a complete rewriting of the numerical scheme and computer code, a non trivial task.

Multigrid methods.

A multigrid method could be developed wherein a relatively coarse grid is initially constructed to allow a solution for the mean flow to be obtained with subsequent automatic refinement of those cells exhibiting high gradients of density. In this way the computational domain would be suitably refined only in those areas requiring it thereby minimising the total number of cells and overall solution time. However, whilst multigrid methods would be extremely useful to resolve the mean flow, it is felt that they would be of limited use in problems featuring acoustic propagation since the acoustic wavespeed is more or less constant and high relative to the mean flow.

The use of a 'standard grid'.

It is a common practice within the industrial power generation business to seek to reduce capital costs by adoption of common components wherever possible. In this respect many of the acoustic solutions offered by companies such as AAF Ltd feature standard components such as filter plenums, transitions and passive silencers that are manufactured en masse. It is suggested that this offers an exciting possibility whereby computation grids could be predefined for many if not all of these standard components leaving the user merely needing to choose the appropriate component from the predefined selection. The user would merely be required to provide basic data such as the frequency range of interest if undertaking an acoustic study with connectivity of the individual grids and output of the grid files undertaken using solution logic in the solver and grid programs.

Use of higher order schemes to reduce grid requirements.

Grid requirements for an acoustic solution are severe compared to those required for a solution of the mean flow. Due to the small acoustic wavelength, high acoustic wave speed and stability requirements a grid resolution of 50 computational cells per wavelength has been found to be required. This has imposed an upper frequency limit on the acoustic solution for the case of the emergency compressor bleed system of approximately 1 KHz. Given that much of the acoustic energy in the gas turbine

power spectrum occurs at approximately 8 KHz this poses a serious limitation onto the code.

The finite volume scheme adopted in this study employed second order central differencing for spatial discretisation. However it is reported that higher order schemes enable a satisfactory acoustic solution to be obtained on a much coarser mesh (Wells & Renault [22] report adequate resolution at only 6-8 cells per wavelength using 6^{th} order central differencing). Although higher order methods have not been implemented yet, it is considered that if a satisfactory acoustic solution can indeed by obtained at a resolution of 6-8 cells per wavelength then they would offer a means to dramatically reduce grid requirements, hence improving computational efficiency and reducing solution time.

Use of parallel processing or 64 bit compilation for the source code.

Parallel processing is a method whereby the computational domain is divided into a number of sub domains, each of which is then solved simultaneously on multiple processors. Its advantages are that the solution time can often be reduced in direct proportion to the number of processors. For aeroacoustic problems such as those studied here where the scale effect can often result in computational domains having a large number of cells parallel processing is seen as a way of greatly reducing overall solution time. However manual creation of a parallel version of the Euler2D code is seen as a non trivial task, however the latest release of the Intel Fortran compiler claims to offer a capability to largely automate this, although this has not yet been investigated by the author and further research would be required in this area. In addition the latest release of the Intel visual fortran compiler is now available for use on 64 bit operating systems. These offer greater bandwidth, increased processor speed and access to increased machine RAM compared with the 32 bit compiler used to create the codes used in this study. For these reasons it is suggested that the use of the 64 bit compiler be investigated as a priority.

Extension of the scheme to a Navier Stokes solution.

The Euler scheme could be readily modified to include the additional terms necessary for the solution of the Navier Stokes equations, in this way direct computation of the noise source would be possible and computation of flow noise would become a possibility. It is considered that this would be an extremely useful development as many of the aerodynamic phenomena of interest such as vortex shedding and flow separation are viscosity dependant and require a Navier Stokes solution. Furthermore given the trend toward lower cost and more compact intake and exhaust treatment systems and their consequent higher flow velocities flow noise itself can become a concern, therefore a means to permit computation of flow noise would be deemed extremely useful. Finally extension to Navier Stokes also ought to assist with convergence at the low Mach number regime where the Euler scheme has been found to present some difficulties.

Extension of the scheme to a 3D solution.

The Euler scheme presented in this study has allowed computation of aerodynamic and acoustic behaviour within a two dimensional domain. Whilst a great deal of useful information can be derived from a 2D study, most practical engineering problems require a three dimensional simulation of the flow. It is considered that the code could be extended to 3D quite easily, however the additional effort required to generate flux terms for the six sided hexahedral cells and the creation of the computational grid itself would not be trivial. In addition computational requirements would be considerably increased making a full three dimensional solution of such a large domain as an entire intake or exhaust system at the acoustic scale difficult, though a solution of the mean flow is considered practical due to the less severe grid resolution required. However the advent of 64 bit parallel processing may make a three dimensional solution of an entire intake or exhaust system at the acoustic scale practical, so extension of the code to a 3D solution should not be discounted before it's feasibility with regard to computational overhead has been assessed.

Bibliography

1. Lighthill, M.J. (1952), "On Sound Generated Aerodynamically: Part I: General Theory" Proceeding of the Royal Society A211, 564-587.

2. Lighthill, M.J. (1954), "On Sound Generated Aerodynamically: Part II: Turbulence as a source of sound", Proceedings of the Royal Society A222, 1-32.

3. Ffowcs Williams J.E. and Hawkings D.L. "Sound generation by turbulence and surfaces in arbitrary motion", Trans. Royal Society Vol. A 264, pp. 321-342, 1969.

4. Beranek, L.L., Noise and Vibration Control, McGraw Hill, 1971

5. K. L. Tam and F. J. Fahy "A theoretical and experimental investigation of sound intensity distribution within a splitter silencer", ISVR, University of Southampton, UK.

6. Soderman, P. T. "Design and performance of resonant-cavity parallel baffles for duct silencing" NASA, Ames Research Center.

7. Ver, I.L. "Design optimization of gas turbine silencers"Proceedings of the International Conference on Noise Control Engineering, August 27-29, 1975.

8. Munjal, M.L. "Analysis and design of pod silencers" Journal of Sound and Vibration, Volume 262, Issue 3, p. 497-507.

9. Anderson, J.D., Computational Fluid Dynamics, McGraw Hill, 1995.

10. Laney, C. Computational Gas Dynamics

11. Tannehill, Anderson and Pletcher, Computational Fluid Mechanics and Heat Transfer, Taylor and Francis, 1997

12. Jameson, A., Schmidt, W. and Turkel, E. "Numerical Solutions of the Euler Equations By Finite Volume Methods Using Runge-Kutta Time-Stepping Schemes." AIAA Paper 81-1259, 1981.

13. Giles, M.B. "Nonreflecting Boundary Conditions for Euler Equation Calculations" AIAA JOURNAL VOL. 28, NO. 12

14. Thompson, K.W, "Time Dependent Boundary Conditions for Hyperbolic Systems" , Journal Of Computational Physics 68, 1-24 (1987)

15. Thompson, K.W, "Time Dependent Boundary Conditions for Hyperbolic Systems II" , Journal Of Computational Physics 89, 439-461 (1990)

16. Poinsot, T, Lele, S.K. "Boundary conditions for direct simulation of compressible viscous flows" , Journal of Computational Physics 101,104-129 (1992).

17. Berenger, J.P, "A perfectly matched layer for the absorption of electromagnetic waves, Journal of Computational Physics 114, 185-200 (1994).

18. Hu, F.Q. , "On absorbing boundary conditions of linearized Euler equations by a perfectly matched layer", Journal of Computational Physics 129 201-219 (1996).

19. Hu, F.Q. , "On constructing stable perfectly matched layers as an absorbing boundary condition for Euler equations", AIAA Paper 2002-0227.

20. Richards, S.K., Zhanga, X.X., Chen, B., Nelson,B. , "The evaluation of non-reflecting boundary conditions for duct acoustic computations" ISVR, Southampton, UK

21. National Advisory Committee For Aeronautics, Report 1135, "Equations, tables and charts for compressible flow", NASA Ames Research Centre.

22. Wells, V.L. and Renault, R.A. "Computing Aerodynamically Generated Noise", Annual Review of Fluid Mechanics, 29, 161-199,1997

23 Private communication and internal report authored by Mr. Brian Walker, acoustics manager at AAF Ltd.

24. Storti, M., Nigro, N., Dalc´ın, L., Paz, R. , "Dynamic boundary conditions in fluid mechanics" Centro Internacional de M´etodos Num´ericos en Ingenier´ıa - CIMEC, Argentina.

APPENDIX 1

FLOWCHART FOR PROGRAM 'EULER2D' WITH REFLECTING BOUNDARY CONDITIONS

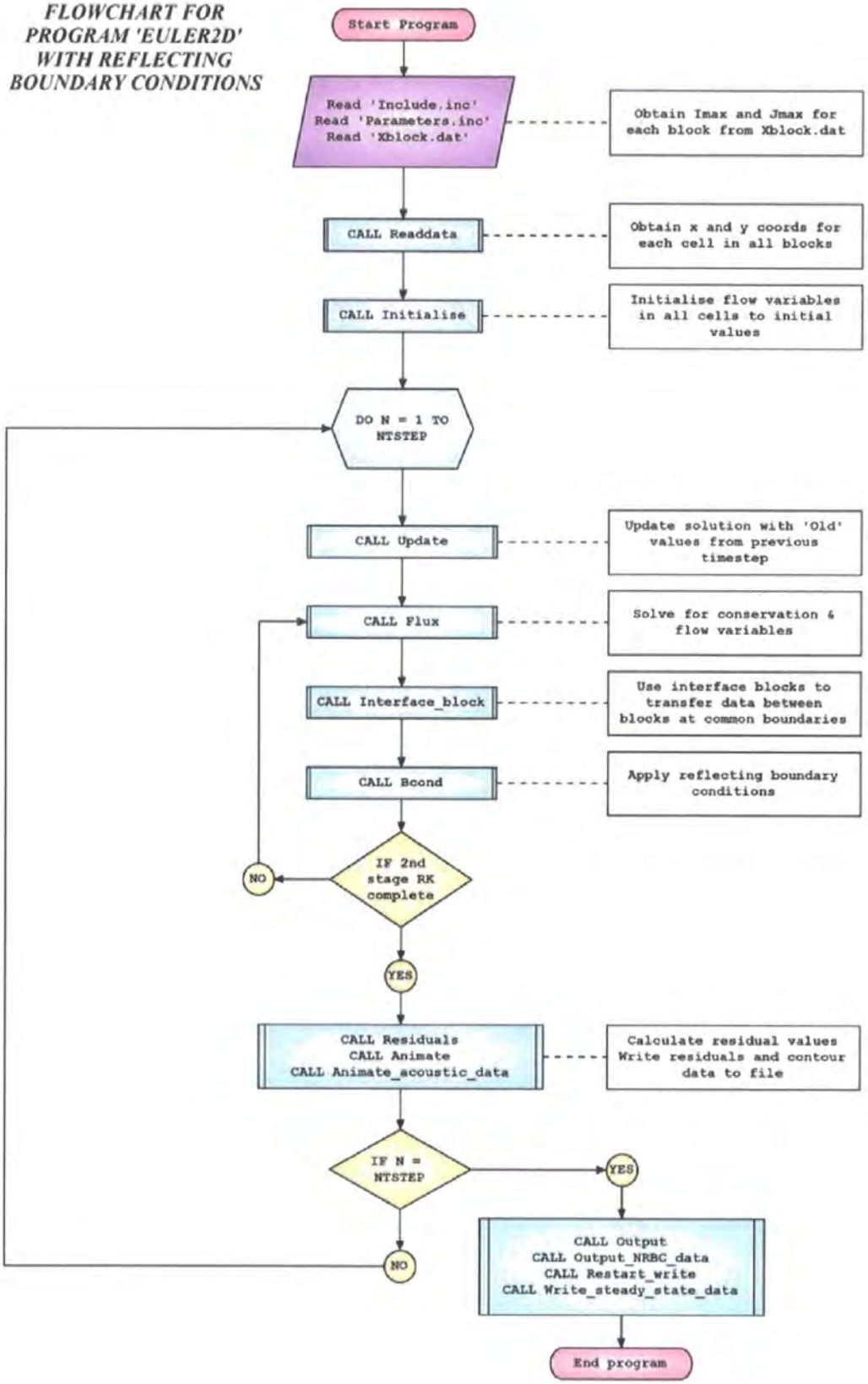

APPENDIX 2

Algebraic Expansion For The 1D Wave Equation Illustrating Effect Of Numerical Dissipation

Considering the 1D wave equation

$$\frac{u_i^{n+1}-u_i^n}{\Delta t}+c.\frac{u_i^n-u_{i-1}^n}{\Delta x}=0$$

Using a Taylor Series expansion for u_i^{n+1}

$$\frac{u_i^n+\Delta t.\frac{\partial u}{\partial t}+\frac{\Delta t^2}{2}.\frac{\partial^2 u}{\partial t^2}+\frac{\Delta t^3}{6}.\frac{\partial^3 u}{\partial t^3}-u_i^n}{\Delta t}+\frac{c}{\Delta x}.u_i^n-\left[u_i^n-\Delta x.\frac{\partial u}{\partial x}+\frac{\Delta x^2}{2}.\frac{\partial^2 u}{\partial x^2}-\frac{\Delta x^3}{6}.\frac{\partial^3 u}{\partial x^3}\right]=0$$

Rearranging and canceling like terms gives

$$\frac{\partial u}{\partial t}+c.\frac{\partial u}{\partial x}=\frac{-\Delta t}{2}.\frac{\partial^2 u}{\partial t^2}+\frac{c.\Delta x}{2}.\frac{\partial^2 u}{\partial x^2}-\frac{\Delta t^2}{6}.\frac{\partial^3 u}{\partial t^3}-\frac{c.\Delta x^2}{6}.\frac{\partial^3 u}{\partial x^3}$$ ---------- **Eqn 1**

Which is seen to be the original wave equation plus an additional truncation term.

To evaluate $\frac{\partial^2 u}{\partial t^2}$ take Equation 1 and differentiate the time derivatives with respect to t.

$$\frac{\partial^2 u}{\partial t^2}+c.\frac{\partial^2 u}{\partial x\partial t}=\frac{-\Delta t}{2}.\frac{\partial^3 u}{\partial t^3}-\frac{\Delta t^2}{6}.\frac{\partial^4 u}{\partial t^4}+\frac{c.\Delta x}{2}.\frac{\partial^3 u}{\partial x^2\partial t}-\frac{c.\Delta x^2}{6}.\frac{\partial^4 u}{\partial x^3\partial t}$$ ---------- **Eqn 2**

Then taking Equation 1 and differentiating with respect to x and multiplying by c

$$c.\frac{\partial^2 u}{\partial x\partial t}+c^2.\frac{\partial^2 u}{\partial x^2}=\frac{-c.\Delta t}{2}.\frac{\partial^3 u}{\partial t^2\partial x}+\frac{c^2.\Delta x}{2}.\frac{\partial^3 u}{\partial x^3}-\frac{c.\Delta t^2}{6}.\frac{\partial^4 u}{\partial t^3\partial x}-\frac{c^2.\Delta x^2}{6}.\frac{\partial^4 u}{\partial x^4}$$ ---------- **Eqn 3**

Rearranging Equation 2

$$\frac{\partial^2 u}{\partial t^2}+c.\frac{\partial^2 u}{\partial x\partial t}+\frac{\Delta t}{2}.\frac{\partial^3 u}{\partial t^3}+\frac{\Delta t^2}{6}.\frac{\partial^4 u}{\partial t^4}-\frac{c.\Delta x}{2}.\frac{\partial^3 u}{\partial x^2\partial t}+\frac{c.\Delta x^2}{6}.\frac{\partial^4 u}{\partial x^3\partial t}=0$$ ---------- **Eqn 4**

Rearranging Equation 3

$$c^2.\frac{\partial^2 u}{\partial x^2}+c.\frac{\partial^2 u}{\partial x\partial t}+\frac{c.\Delta t}{2}.\frac{\partial^3 u}{\partial t^2\partial x}-\frac{c^2.\Delta x}{2}.\frac{\partial^3 u}{\partial x^3}+\frac{c.\Delta t^2}{6}.\frac{\partial^4 u}{\partial t^3\partial x}+\frac{c^2.\Delta x^2}{6}.\frac{\partial^4 u}{\partial x^4}=0$$ ---------- **Eqn 5**

And subtracting Equation 5 from Equation 4

$$\frac{\partial^2 u}{\partial t^2} - c^2\frac{\partial^2 u}{\partial x^2} + \frac{\Delta t}{2}.\frac{\partial^3 u}{\partial t^3} - c.\frac{\Delta t}{2}.\frac{\partial^3 u}{\partial t^2 \partial x} + \frac{\Delta t^2}{6}.\frac{\partial^4 u}{\partial t^4} + c^2.\frac{\Delta x}{2}.\frac{\partial^3 u}{\partial x^3}$$
$$- c.\frac{\Delta x}{2}.\frac{\partial^3 u}{\partial x^2 \partial t} - c.\frac{\Delta t^2}{6}.\frac{\partial^4 u}{\partial t^3 \partial x} + c.\frac{\Delta x^2}{6}.\frac{\partial^4 u}{\partial x^3 \partial t} - c^2.\frac{\Delta x^2}{6}.\frac{\partial^4 u}{\partial x^4} = 0 \qquad \text{---------- Eqn6}$$

Considering only 1st order terms.

$$\frac{\partial^2 u}{\partial t^2} - c^2\frac{\partial^2 u}{\partial x^2} + \frac{\Delta t}{2}.\frac{\partial^3 u}{\partial t^3} - c.\frac{\Delta t}{2}.\frac{\partial^3 u}{\partial t^2 \partial x} + c^2.\frac{\Delta x}{2}.\frac{\partial^3 u}{\partial x^3} - c.\frac{\Delta x}{2}.\frac{\partial^3 u}{\partial x^2 \partial t} = 0 \qquad \text{---------- Eqn 7}$$

Finally, isolating for $\frac{\partial^2 u}{\partial t^2}$

$$\frac{\partial^2 u}{\partial t^2} = c^2\frac{\partial^2 u}{\partial x^2} + \frac{\Delta t}{2}.\left[-\frac{\partial^3 u}{\partial t^3} + c.\frac{\partial^3 u}{\partial t^2 \partial x}\right] + \frac{\Delta x}{2}.\left[-c^2.\frac{\partial^3 u}{\partial x^3} + c.\frac{\partial^3 u}{\partial x^2 \partial t}\right] \qquad \text{---------- Eqn 8}$$

We obtain an expression that can be substituted into Equation 1.

We now need to obtain an expression for $\frac{\partial^3 u}{\partial t^3}$

Differentiating Equation 8 with respect to time t.

$$\frac{\partial^3 u}{\partial t^3} = c^2.\frac{\partial^3 u}{\partial x^2 \partial t} + HigherOrderTerms(\Delta t, \Delta x) \qquad \text{---------- Eqn 9}$$

To evaluate $c^2.\frac{\partial^3 u}{\partial x^2 \partial t}$ we can differentiate Equation 3 with respect to x and multiply by c

i.e. $c^2.\frac{\partial^3 u}{\partial x^2 \partial t} = -c^3.\frac{\partial^3 u}{\partial x^3} + HigherOrderTerms$ --------- Eqn 10

So that finally

$$\frac{\partial^3 u}{\partial t^3} = -c^3.\frac{\partial^3 u}{\partial x^3} + HigherOrderTerms(\Delta t, \Delta x) \qquad \text{---------- Eqn 11}$$

Now, looking again at Equation 1 we see there are two further expressions that need to be evaluated, these being $\frac{\partial^3 u}{\partial t^2 \partial x}$ *and* $\frac{\partial^3 u}{\partial x^2 \partial t}$

To evaluate $\frac{\partial^3 u}{\partial t^2 \partial x}$ we can differentiate Equation 8 with respect to x.

i.e.

$$\frac{\partial^3 u}{\partial t^2 \partial x} = c^2 \frac{\partial^3 u}{\partial x^3} + HigherOrderTerms \qquad \text{---------- Eqn 12}$$

And to evaluate $\frac{\partial^3 u}{\partial x^2 \partial t}$ we can make use of Equation 9 and Equation 11 such that

$$c^2 . \frac{\partial^3 u}{\partial x^2 \partial t} = -c^3 \frac{\partial^3 u}{\partial x^3} + HigherOrderTerms(\Delta t, \Delta x)$$

And hence $\frac{\partial^3 u}{\partial x^2 \partial t} = -c \frac{\partial^3 u}{\partial x^3} + HigherOrderTerms(\Delta t, \Delta x)$ ---------- **Eqn 13**

Equations 11,12 and 13 may now be substituted into Equation 8 and Equation 1 giving

$$\frac{\partial u}{\partial t} + c . \frac{\partial u}{\partial x} = \left[\frac{c.\Delta x}{2} - \frac{c^2 \Delta t}{2} \right] . \frac{\partial^2 u}{\partial x^2} + \left[-\frac{c^3 \Delta t^2}{2} + \frac{c^2 . \Delta x . \Delta t}{2} + \frac{c^3 . \Delta t^2}{6} - \frac{c . \Delta x^2}{6} \right] . \frac{\partial^3 u}{\partial x^3} \qquad \text{--------- Eqn 14}$$

Writing the timestep Δt in terms of the Courant Number $\Delta t = \frac{CFL.\Delta x}{c}$ results in a final expression for the truncation, or damping term, i.e.

$$\frac{\partial u}{\partial t} + c . \frac{\partial u}{\partial x} = \frac{c.\Delta x}{2} [1 - CFL] . \frac{\partial^2 u}{\partial x^2} - \frac{c.\Delta x^2}{6} [2.CFL^2 - 3.CFL + 1] \frac{\partial^3 u}{\partial x^3} \qquad \text{---------- Eqn 15}$$

APPENDIX 3

Multiblock Implementation

Introduction

Due to the complex geometry of the gas turbine intake systems it was obvious that the computational domain would have to be decomposed into a number of simplified domains, each created using transfinite interpolation, but then coupled to one another in the solver to form a complex multiblock domain. Therefore a method to create a multiblock grid and solver would have to be developed.

Geometry And Interface Block Creation.

In order to study the multiblock method, a simple geometry was chosen, in this case a rectangular duct containing a 10 degree wedge. The geometry was defined as three discrete planar areas and the computational grid created using the method of transfinite interpolation. The grid employed for the study is shown below in Figure A3.1

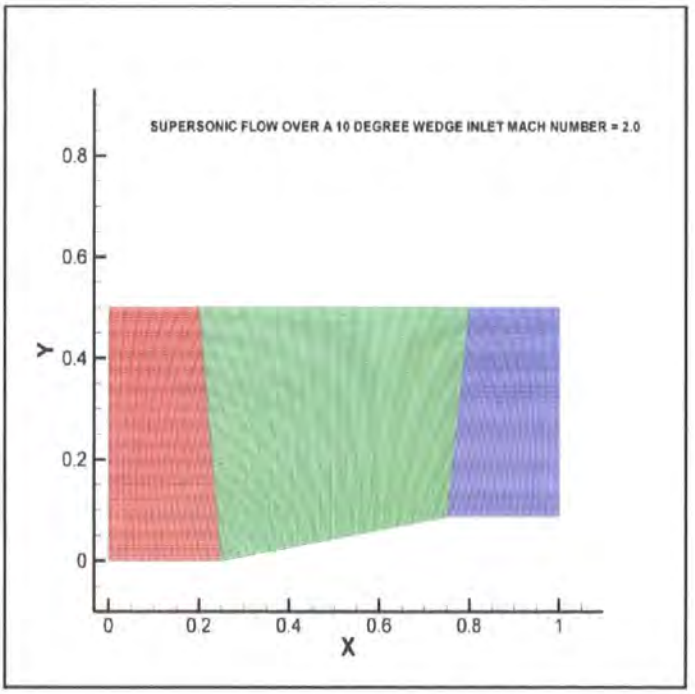

Figure A3.1

Interface Blocks

In order to pass data between adjacent domain blocks, an interface block subroutine was required. A method was proposed as follows.

From Figure A3.1 it was apparent that the outputs from block 1 (shown coloured red) would serve as inputs to block 2 (shown coloured green) , and the outputs from block 2 would serve as inputs to block 3 (shown coloured blue). Therefore, when applying the boundary conditions, the inlet boundary would be applied to the left edge of block 1 and the outlet boundary would be applied to the right edge of block 3. An interface block would be required between the outlets (i.e. the right hand edges) of blocks 1 and 2 and the inlets of blocks 2 and 3.

As an example of how the interface blocks were constructed, consider Figure A3.2 below.

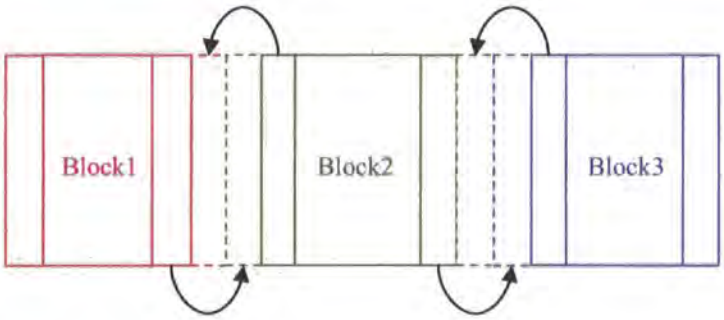

Dotted lines denote dummy cells at i=1
and i=imax+1 for each block
Solid lines denote real cells

Figure A3.2

It can be seen that the values of the flow variables in the ghost cells forming the outlet boundary of block 1 are taken from the values of the first 'real' cells in block 2, i.e. , for pressure we could write
$P(Imax+1)_{block\ 1} = P(I,2)_{block\ 2}$

Similarly, at the inlet of block 2 we can see that the values of the flow variables in the ghost cells forming the inlet boundary of block 2 are taken from the values of the last 'real' cells in block 1, so again for pressure we could write $P(1)_{block\ 2} = P(Imax)_{block1}$

This procedure can be applied to all cells in the vertical (or J) direction at the inlet and outlet of each block using a simple DO loop. Note that for the multiblock method three dimensional arrays have been required to store the data for each block. In this way each block could be allocated a block index which was then used as a calling argument in the solver subroutine.